Measurement of the Product Branching Ratio $f(\mathrm{b} \to \Lambda_\mathrm{b}) \cdot BR(\Lambda_\mathrm{b} \to \Lambda \ell^- \bar{\nu} \mathrm{X})$

by

Johannes Martin Steuerer
B.Sc., Trent University, 1988
Dipl. Phys., Albert-Ludwigs-Universität Freiburg i. Br., 1990

A dissertation Submitted in Partial Fulfilment of the
Requirements for the Degree of

DOCTOR OF PHILOSOPHY

in the Department of Physics and Astronomy

We accept this thesis as conforming
to the required standard.

Dr. A. Astbury, Supervisor (Department of Physics & Astronomy)

Dr. R. K. Keeler, Departmental Member (Department of Physics & Astronomy)

Dr. D. Pitman, Departmental Member (Department of Physics & Astronomy)

Dr. T. W. Dingle, Outside Member (Department of Chemistry)

Dr. D. Hoffman, Outside Member (Department of Computer Science)

Dr. D. Stairs, External Examiner (Department of Physics, McGill University)

Supervisor: Dr. A. Astbury

Abstract

The product branching ratio $f(\mathrm{b} \to \Lambda_\mathrm{b}) \cdot BR(\Lambda_\mathrm{b} \to \Lambda \ell^- \bar{\nu} \mathrm{X})$, where the symbol Λ_b represents all b-flavoured baryons and $f(\mathrm{b} \to \Lambda_\mathrm{b})$ denotes the probability of a b quark to be confined in a baryon, is measured using 3.6 million hadronic Z^0 decays recorded with the OPAL detector between 1990 and 1994. Bottom-flavoured baryons that decay semileptonically to a final state which includes a Λ are identified through the charge correlation of the Λ and the lepton. The product branching ratios are measured to be:

$$f(\mathrm{b} \to \Lambda_\mathrm{b}) \cdot BR(\Lambda_\mathrm{b} \to \Lambda \mathrm{e}^- \bar{\nu}_\mathrm{e} \mathrm{X}) = (2.59 \pm 0.37 \pm 0.23) \cdot 10^{-3}$$

$$f(\mathrm{b} \to \Lambda_\mathrm{b}) \cdot BR(\Lambda_\mathrm{b} \to \Lambda \mu^- \bar{\nu}_\mu \mathrm{X}) = (3.10 \pm 0.30 \pm 0.27) \cdot 10^{-3};$$

leading to a combined result of:

$$f(\mathrm{b} \to \Lambda_\mathrm{b}) \cdot BR(\Lambda_\mathrm{b} \to \Lambda \ell^- \bar{\nu} \mathrm{X}) = (2.91 \pm 0.23 \pm 0.25) \cdot 10^{-3},$$

where the symbol ℓ represents either an electron or a muon.

Examiners:

Dr. A. Astbury, Supervisor (Department of Physics & Astronomy)

Dr. R. K. Keeler, Departmental Member (Department of Physics & Astronomy)

Dr. D. Pitman, Departmental Member (Department of Physics & Astronomy)

Dr. T. W. Dingle, Outside Member (Department of Chemistry)

Dr. D. Hoffman, Outside Member (Department of Computer Science)

Dr. B. Stairs, External Examiner (Department of Physics, McGill University)

Contents

List of Tables

List of Figures

Acknowledgements

Of the many people who helped in the progress of this dissertation and to whom I am sincerely thankful, I would like to mention especially Richard van Kooten and Christian Stegmann. I am grateful for their constructive comments and their practical support throughout all these years.

I also would like to thank the TRIUMF group and the University of Victoria for their financial support and the German people, who provide a free educational system, allowing me to study physics in the first case.

Dedication

To my parents
who patiently and steady supported their kid's 32 year long educational period
which finally ends with this work.

Ich widme diese Arbeit meinen Eltern,
die mich fortwährend in meiner 32 jährigen Ausbildung unterstützten.
Diese Lehrzeit findet nun ein Ende.

Chapter 1

Introduction

The world's largest accelerator is located in a 27 km long tunnel close to Geneva, Switzerland. The accelerator is called *LEP*[1]. LEP was built to study some of the fundamental forces of nature and to measure the properties of objects on which these forces act. The machine collides electrons and positrons at centre-of-mass energies sufficient to create Z^0 particles. The Z^0 particle, along with its charged analogues, the W^+ and W^-, are responsible for the *weak force*. The Z^0 particles created decay into *leptons* and *quarks*. This thesis will concentrate on one particular quark called the b quark, which stands for either "bottom" or "beauty."

The *Standard Model* [1] of particle physics assumes that *leptons* and *quarks* (see table 1.1) are elementary particles. Free quarks have never been observed [2]. Instead one observes a spectrum of particles called *hadron*. The *quark model* [3], a part of the Standard Model, assumes hadrons are composed of elementary quarks. Quarks are bound together by a basic force called the *strong force* which is postulated to couple to *colour charge*, a quantum number which is assigned to the quarks. It can assume three values called *red*, *green* and *blue*[2]. Hadrons are subdivided into two classes, *mesons* and *baryons*. The subdivision occurs naturally in the quark model by requiring all hadrons to

---

[1] Large Electron Positron Collider.

[2] Antiquarks carry anticolour.

Fermions							
	Symbol			Charge in e	Mass in GeV/c^2		
Generation	I	II	III	all	I	II	III
Leptons	ν_e	ν_μ	ν_τ	0	0	0	0
	e^-	μ^-	τ^-	-1	$5.11\ 10^{-4}$	0.106	1.78
Quarks	u	c	t	$+\frac{2}{3}$	$5.6\ 10^{-3}$	1.35	180
	d	s	b	$-\frac{1}{3}$	$9.9\ 10^{-3}$	0.199	4.7

Table 1.1: Fermions and their Masses

Listed are the different fermion species in the Standard Model, their charge and their masses. The quark masses given refer to the current quark masses calculated from the QCD Lagrangian [2] p. 1433.

be of neutral colour. Neutral colour is obtained by either combining a quark with an antiquark with equal parts of colour and anticolour to create a meson, or by combining three quarks (or antiquarks) with different colours to create a baryon. Furthermore, the quark model postulates that the quarks carry an electric charge, Q_f, of either $-1/3\,e$ or $+2/3\,e$, where e is the positron charge. These charge assignments lead to the observed integer charges of the hadrons. Leptons and quarks are *fermions* with *spin*[3] 1/2. Therefore, mesons have integer spin while baryons carry half-integer spin. The nature of the strong force and the quark model is outlined in more detail in section 2.2.

The Z^0 decays to fermion-antifermion pairs. The $Z^0 \rightarrow b\bar{b}$ decays are the subject of this thesis. The b quarks produced undergo a process called *fragmentation* in which hadrons are formed. Fragmentation involves quark-antiquark pairs produced from the vacuum quantum-mechanically which then combine to create mesons and baryons. The quarks can be categorised as heavy or light according to their masses. The *heavy quarks* are t, b and c

---

[3] The spin is a quantum property denoting the statistical behaviour of particles (spin statistics theorem). In general, particles can either have integer spin and obey Bose-Einstein statistics (*bosons*) or half-integer spin obeying Fermi-Dirac statistics (*fermions*). The most obvious difference between the two is that the Pauli Exclusion Principle applies for fermions; that is no two identical fermions can be in the same quantum-mechanical state.

while u, d and s are called the *light quarks*. Light quarks are easily pair-produced in the fragmentation process while heavy quarks have a negligible production probability (see p. 24). Therefore, in a study of b hadrons formed in Z^0 decays one is studying directly the fragmentation process in which a primordial b quark "dressed itself" to become a b hadron. Hadrons containing one heavy quark and one (meson) or two (baryon) light quarks are of special interest since the hadron's behaviour is dominated by the heavy quark while the light quarks play the role of *spectators*. The spectator quarks have only a small influence on particle properties such as decay rates and lifetimes. The properties of heavy hadrons, especially those of b hadrons, can be calculated at the quark level and effects arising from the confinement into hadrons can be treated as perturbations. This approach is commonly referred to as *Heavy Quark Effective Theory* (HQET) [4].

Theoretical studies [5, 6] based on HQET indicate that the properties of b baryons (baryons containing a b quark) can be predicted with a smaller theoretical error than those of b mesons. In this thesis the product branching ratio

$$f(\mathrm{b} \rightarrow \Lambda_\mathrm{b}) \cdot BR(\Lambda_\mathrm{b} \rightarrow \Lambda \ell^- \bar{\nu} \mathrm{X}) \tag{1.1}$$

is measured where the symbol Λ_b represents all b baryons[4]. The branching fraction $f(\mathrm{b} \rightarrow \Lambda_\mathrm{b})$ denotes the probability that a b quark will become confined in a b baryon during the fragmentation process. The branching ratio $BR(\Lambda_\mathrm{b} \rightarrow \Lambda \ell^- \bar{\nu} \mathrm{X})$ is the probability of a b baryon decaying semileptonically into a lepton, ℓ^-, a Λ particle, and any other particles, X. The Λ may be the decay product of intermediate hadrons. Only electrons and muons are considered as lepton candidates in this analysis. The decay chain of the Λ_b studied in this thesis is[5]

$$\begin{array}{lll} \Lambda_\mathrm{b} & \rightarrow \Lambda_\mathrm{c}\, \ell^-\, \bar{\nu} & \\ & \quad\hookrightarrow \Lambda\ \mathrm{X} & \\ & \qquad\hookrightarrow \mathrm{p}\ \pi^- & \end{array} , \tag{1.2}$$

---

[4] Throughout this thesis, the symbols Λ_b and Λ_c are used to represent all b or c baryons. In contrast, the symbols Λ_b^0 and Λ_c^+ refer to the specific particles.

[5] Throughout this thesis the charge conjugate processes are accounted for implicitly without further mention.

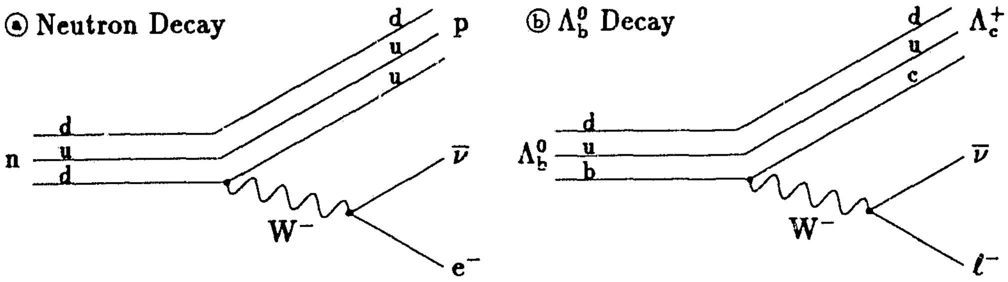

Figure 1.1: Weak Decays

The weak decay of a neutron into a proton, an electron, and a neutrino is shown in figure ⓐ. Analogously, a Λ_b^0 decays into a Λ_c^+, a lepton, and a neutrino, as shown in figure ⓑ. The small letters above the lines denote the quark content of the baryons.

where the Λ particles are identified by their prominent decay channel $\Lambda \rightarrow p\pi^-$. Therefore, baryons containing a b quark are identified by selecting Λ particles and leptons that are kinematically correlated.

The measurement of the product branching ratio is a first step in the process that eventually will lead to a determination of the branching ratio $BR(\Lambda_b^0 \rightarrow \Lambda_c^+ \ell^- \overline{\nu})$. In this reaction the b quark in the Λ_b^0 becomes a c quark in the Λ_c^+ through weak decay. It is an analogous process to the neutron decay where a d quark decays into an u quark, as shown in figure 1.1.

The conversion of an u-type quark (charge $+2/3\,e$) into a d-type quark (charge $-1/3\,e$) and vice versa occurs through the weak transition by emission and absorption of a $W^\pm$ particle. However, there is a complication. The quark eigenstates under the strong interaction are not the same as the quark eigenstates under the weak interaction. A unitary matrix called the Cabibbo-Kobayashi-Maskawa matrix (*CKM matrix*) relates the two bases. The branching ratio $BR(\Lambda_b^0 \rightarrow \Lambda_c^+ \ell^- \overline{\nu})$ depends on one element, V_{cb}, of the CKM matrix. It was recently pointed out [5, 6] that the CKM-matrix element V_{cb}, determined so far from semileptonic b-meson decays, could be obtained with less theoretical uncertainty from semileptonic b-baryon decays.

The Standard Model is presented in more detail in chapter 2. The production of b quarks at LEP is discussed and their subsequent fragmentation into hadrons and decays are described. The relationship between the branching ratio $BR(\Lambda_b^0 \rightarrow \Lambda_c^+ \ell^- \overline{\nu})$ and the CKM-matrix element V_{cb} is developed.

Chapter 3 describes the LEP accelerator and the OPAL detector. The LEP machine has unique advantages for observing b baryons and, in fact, semileptonic b-baryon decays were first observed by LEP experiments [7, 8, 9].

Chapter 4 outlines the selection procedure of the b baryons from the data recorded with OPAL in the years 1990–1994. The data set corresponds to more than 4 million observed Z^0 decays. Details of the efficiency determination, estimation of the backgrounds and the calculation of systematic errors are presented in the chapters 5 and 6. In chapter 7, the product branching ratio $f(b \rightarrow \Lambda_b) \times BR(\Lambda_b \rightarrow \Lambda \ell^- \overline{\nu} X)$ is computed. The resulting value is compared to previous measurements over which the statistical and systematical errors are improved significantly. Furthermore, it is demonstrated in chapter 7 how the product branching ratio measurement and other measurements can used to determine, first, the branching fraction $f(b \rightarrow \Lambda_b)$ and, secondly, the branching ratio $BR(\Lambda_b^0 \rightarrow \Lambda_c^+ \ell^- \overline{\nu})$. The values obtained are compared to the prediction of different theoretical models.

Chapter 2

Theory

Three intrinsically different forces are known in nature: gravity, the electroweak force and the strong force. The Standard Model describes the latter two, the electroweak and the strong force. Nevertheless, the most obvious force is *gravity*. Gravity is actually the weakest of all forces. It appears large because it is always attractive, has infinite range, and cannot be neutralised. The gravitational force between elementary particles, however, is extremely small and can be neglected when studying particle interactions at available accelerator energies.

The second force is the *electroweak force*. At energy scales significantly smaller than the Z^0 mass ((91.1895 ± 0.0043) GeV/c^2) [10] it breaks down into two components. One component is the *electromagnetic force* which is of infinite range and observable macroscopically in electric and magnetic phenomena. The electric and magnetic force can be described with a consistent formalism developed by Maxwell in the middle of the previous century. The other component of the electroweak force at low energies is the weak force. The *weak force* acts only over distances of sub-nuclear scale ($\sim$ 0.002 fm) and is responsible for radioactive β-decay. Glashow, Salam and Weinberg [11] demonstrated in the late 1960's that the electromagnetic and the weak force can be described by a unifying theory. The electroweak force will be discussed in more detail in section 2.1.

The third force is the *strong force*. It is responsible for binding the quarks together into hadrons, and the neutrons and protons together into nuclei. In the Standard Model the strong force is described by *QCD*[1]. The nature of the strong force and some aspects of QCD which are important for this thesis are discussed in section 2.2.

The electroweak and the strong force are responsible for the reactions studied in this thesis. The time evolution of an $e^+e^- \rightarrow \gamma, Z^0 \rightarrow b\overline{b}$ event is characterised by four different stages (see fig. 2.1).

Stage 1 is dominated by the electroweak force. It consists of the e^+e^- annihilation into a γ/Z^0 and the subsequent decay into a $b\overline{b}$-quark pair. As outlined in section 2.1, the cross section for the process can be calculated in the framework of the Standard Model. The production probability of a $b\overline{b}$ pair in comparison to the overall quark pair production rate in e^+e^- annihilation at energies close to the Z^0 pole is estimated in section 2.1.1. This value is important for the derivation of the product branching ratio in chapter 7.

Stage 2 and **stage 3** are in the domain of the strong force. In stage 2, the strong force can be described by perturbation theory as discussed in section 2.2.1. In stage 3, perturbation theory is no longer applicable and a phenomenological model, as introduced in section 2.2.2, is used to describe the formation of hadrons. It is emphasised that no additional b quarks are expected to be produced in either of the two stages. The baryon production mechanism in the phenomenological model and the resulting prediction of the confinement probability of the b quark in a baryon, $f(b \rightarrow \Lambda_b)$, are discussed in section 2.2.2.

Stage 4 consists of secondary particle decays caused by either of the forces. In section 2.3, the weak decays of b-baryons are discussed. The relationship between the branching ratio $BR(\Lambda_b \rightarrow \Lambda_c \ell \overline{\nu})$ and the CKM-matrix element V_{cb} is explained. Several different estimates of the branching ratio are given. The measured value will be compared to these estimates in chapter 7.

---

[1] Quantum Chromodynamics.

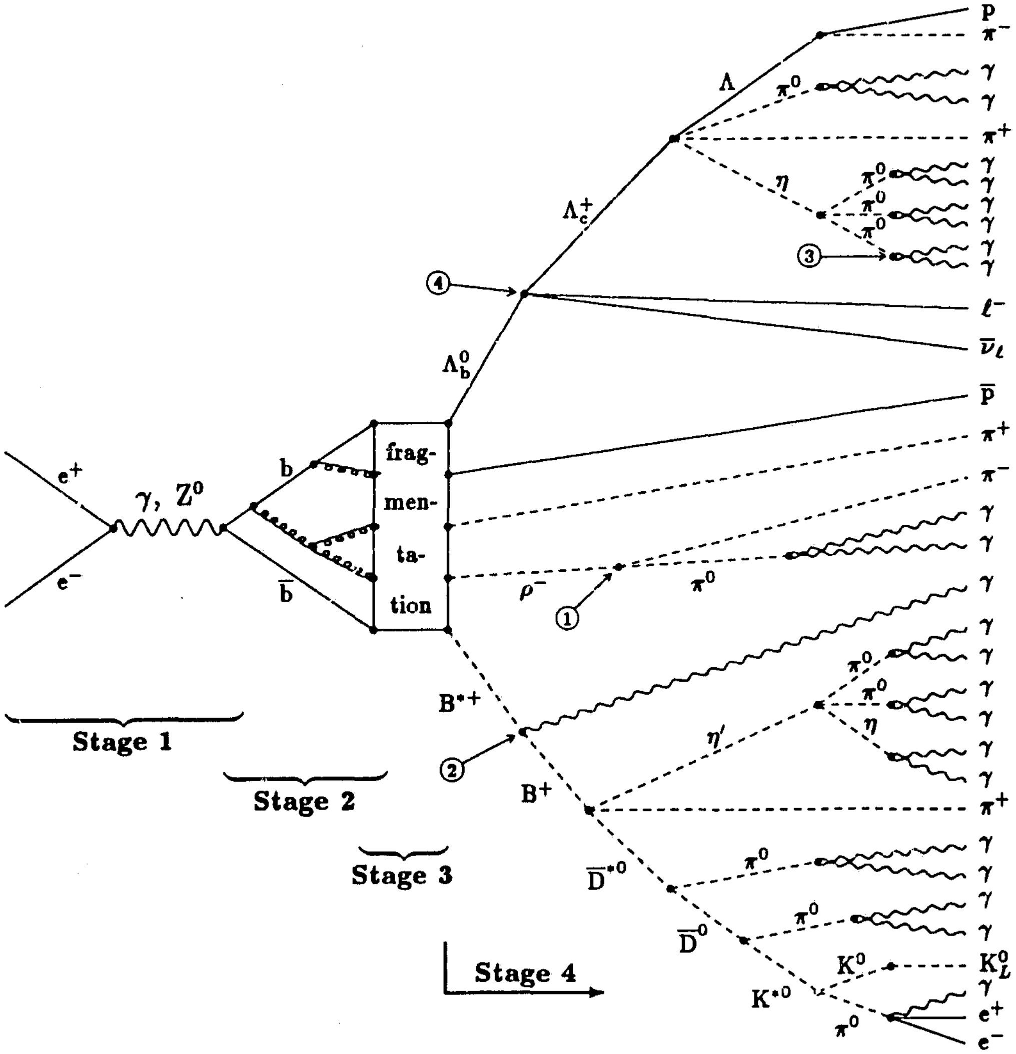

Figure 2.1: Simulated $e^+e^- \rightarrow \gamma, Z^0 \rightarrow b\bar{b} \rightarrow$ Hadrons Event

Based on theoretical models (here JETSET) the event may be separated into four different stages as described in the text. The markers ① to ④ are used to point out specific decays: ① strong decay, ② and ③ electromagnetic decays and, of special interest, the semileptonic weak decay of a Λ_b *④.*

The last section of this chapter, 2.4, is a summary and outlines the importance of the measurement presented here.

2.1 Electroweak Theory

The electroweak theory, based on the SU(2)$_L$ × U(1) gauge group[2], leads to two coupling constants, g and g', and four massless gauge boson fields,

$$\begin{pmatrix} W_\mu^1 \\ W_\mu^2 \\ W_\mu^3 \end{pmatrix} \text{ and } B_\mu,$$

which act on massless fermions. Since the fermions are presumed to be massless, the helicity operator forms true eigenstates of the system. The left-handed fermion fields transform as doublets under SU(2) transformations and are quantised by a *weak isospin* of 1/2, while the right-handed fields behave as singlets corresponding to a weak isospin of 0. The fermions,

$$\begin{array}{cccccc} \begin{pmatrix} \nu_e \\ \mathrm{e} \end{pmatrix}_L, & \begin{pmatrix} \nu_\mu \\ \mu \end{pmatrix}_L, & \begin{pmatrix} \nu_\tau \\ \tau \end{pmatrix}_L, & \mathrm{e}_R, & \mu_R, & \tau_R, \\ \begin{pmatrix} \mathrm{u} \\ \mathrm{d}' \end{pmatrix}_L, & \begin{pmatrix} \mathrm{c} \\ \mathrm{s}' \end{pmatrix}_L, & \begin{pmatrix} \mathrm{t} \\ \mathrm{b}' \end{pmatrix}_L, & \begin{matrix} \mathrm{u}_R, \\ \mathrm{d}_R, \end{matrix} & \begin{matrix} \mathrm{c}_R, \\ \mathrm{s}_R, \end{matrix} & \begin{matrix} \mathrm{t}_R, \\ \mathrm{b}_R, \end{matrix} \end{array}$$

appear massive due to interactions with the scalar "Higgs-field." The mass of the corresponding Higgs-particle and the couplings to it are free parameters in the model. The introduction of the scalar Higgs field leads to a process called *spontaneous symmetry-breaking*. As a consequence of the symmetry-breaking mechanism, the left-handed fermions observed are mixtures of the fermions listed above. In the minimal Standard Model, neutrinos are massless and right-handed neutrinos do not exist. As a consequence, leptons are unmixed.

---

[2] **The term *gauge group* denotes a transformation of a physical system that obeys the symmetry of the mathematical group and leaves the physical state of the system unchanged.**

In the quark case, the mixing is described by the *Cabibbo-Kobayashi-Maskawa matrix* (CKM matrix),

$$\begin{pmatrix} \mathrm{d}' \\ \mathrm{s}' \\ \mathrm{b}' \end{pmatrix} = \begin{pmatrix} V_{\mathrm{ud}} & V_{\mathrm{us}} & V_{\mathrm{ub}} \\ V_{\mathrm{cd}} & V_{\mathrm{cs}} & V_{\mathrm{cb}} \\ V_{\mathrm{td}} & V_{\mathrm{ts}} & V_{\mathrm{tb}} \end{pmatrix} \begin{pmatrix} \mathrm{d} \\ \mathrm{s} \\ \mathrm{b} \end{pmatrix} \tag{2.1}$$

with d, s and b being the physical quarks and d′, s′ and b′ being the weak eigenstates. By convention, the three quarks with charge $+\frac{2}{3}e$ are unmixed and the mixing takes place only between the $-\frac{1}{3}e$ charged quarks. The CKM matrix allows flavour-changing charged currents in the quark sector of the electroweak theory. Since the matrix must be unitary, it can be parametrised by four free parameters [2]. The CKM matrix will be discussed further in section 2.3.

As a further consequence of the symmetry-breaking mechanism, the four fields corresponding to the physical electroweak exchange bosons are mixtures of the gauge boson fields mentioned above,

$$\begin{aligned} W_\mu^\pm &= \frac{1}{\sqrt{2}}\left(W_\mu^1 \mp iW_\mu^2\right), \\ Z_\mu^0 &= \cos(\theta_W)\, W_\mu^3 - \sin(\theta_W)\, B_\mu, \\ A_\mu &= \sin(\theta_W)\, W_\mu^3 + \cos(\theta_W)\, B_\mu. \end{aligned} \tag{2.2}$$

The mixing angle, θ_W, is called the *Weinberg angle* which is measured to be $\sin^2\theta_W = 0.2311 \pm 0.0009$ [10]. The Weinberg angle is related to the coupling constants by

$$\tan\theta_W = \frac{g'}{g} \qquad \text{and} \qquad e = g\sin\theta_W \tag{2.3}$$

where e is the positron's electric charge. The field A_μ corresponds to the massless photon, the carrier of the electromagnetic force. It couples to electrically charged fermions, independent of their helicity. The other three fields are massive and correspond to the Z^0, W^+ and W^- bosons which are the carriers of the weak force. The Z^0 couples preferentially to left-handed fermions but also, due to its B_μ field component, to right-handed fermions. The $W^\pm$ couples to left-handed fermions only. However, now the helicity states are only approximate eigenstates of the fermion fields, due to the non-zero fermion masses.

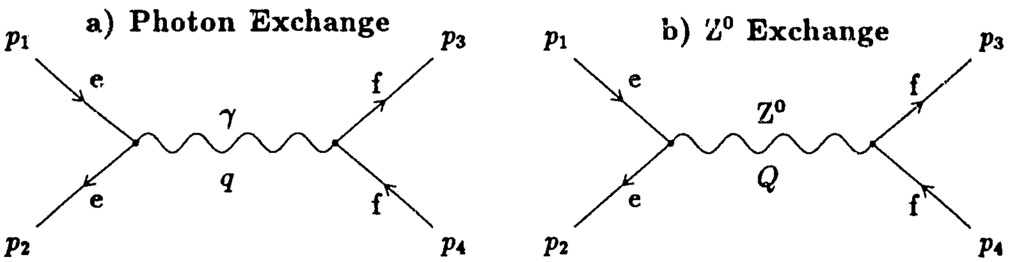

Figure 2.2: Tree Level Diagrams of $e^+e^- \to \gamma, Z^0 \to f\bar{f}$
Shown are the lowest-order diagrams for an e^+e^- *annihilation at centre-of-mass energies close to* $m_Z c^2$*. In the case of* $f\bar{f} = e^+e^-$*, two t-channel exchange diagrams describing the electron scattering need to be considered in addition to the two s-channel annihilation diagrams shown.*

The electroweak theory at energies below the TeV scale can be approximated by perturbation expansion, since the electroweak couplings are small. The terms in the perturbation expansion can be displayed graphically as *Feynman diagrams* [12]. Figure 2.2 shows the Feynman diagrams that correspond to the first terms in the perturbation expansion. Higher order terms can be treated as corrections to the first order calculation.

2.1.1 Cross Section

The *cross section*, σ, is a measure of the likelihood of two incoming particles reacting with each other. It is measured in units of area. The rate of collisions is simply the product of the specific cross section and the luminosity $\mathcal{L}$,

$$\text{rate} = \mathcal{L} \cdot \sigma. \tag{2.4}$$

The *luminosity* denotes the number of incoming particles per unit time and per unit area.

The annihilation of a high energy electron and a positron into an electroweak exchange boson, γ or Z^0, and the subsequent decay of this boson into leptons or quarks can be calculated with the aid of Feynman diagrams. To lowest order, only two diagrams contribute to the production of a fermion-antifermion pair, $\mathrm{f\bar{f}}$, with the exception of an $\mathrm{e^+e^-}$ pair[3]. First, the s-channel exchange of a photon and second, the s-channel exchange of a $\mathrm{Z^0}$ as shown in figure 2.2. The cross section calculation is straightforward using Feynman rules. The total cross section for a $\mathrm{f\bar{f}}$ final state is obtained by ([13] p. 12),

$$\begin{aligned} \sigma_{\mathrm{f\bar{f}}}(s) \;=\; & \frac{4\pi\alpha^2}{3s}\,(\hbar c)^2\, N_c^{\mathrm{f}}\, \beta_{\mathrm{f}} \\ & \times\Big[\; \tfrac{1}{2}\left(3-\beta_{\mathrm{f}}^2\right) Q_{\mathrm{f}}^2\, Q_{\mathrm{e}}^2 \\ & \quad + \left(\beta_{\mathrm{f}}^2 a_{\mathrm{f}}^2 + \tfrac{1}{2}\left(3-\beta_{\mathrm{f}}^2\right) v_{\mathrm{f}}^2\right)\left(a_{\mathrm{e}}^2 + v_{\mathrm{e}}^2\right) |\chi(s)|^2 \\ & \quad + 2\, Q_{\mathrm{f}}\, Q_{\mathrm{e}}\, \tfrac{1}{2}\left(3-\beta_{\mathrm{f}}^2\right) v_{\mathrm{e}}\, v_{\mathrm{f}}\; \mathrm{Re}\left(\chi(s)\right) \;\Big], \end{aligned} \tag{2.5}$$

where $\sqrt{s}$ is the centre-of-mass energy, N_c^{f} is the *colour factor* reflecting the three different colours quarks can carry ($N_c^{\mathrm{q}} = 3$ for quarks, $N_c^{\ell} = 1$ for leptons) and α is the fine structure constant at $\sqrt{s} = m_{\mathrm{Z}}\, c^2$. The fine structure constant increases with increasing energy due to higher order corrections. At energies near the $\mathrm{Z^0}$-resonance, $\alpha(\sqrt{s}=m_{\mathrm{Z}}\, c^2) \simeq \frac{1}{128}$. The velocity of the final state fermion in the centre-of-mass system relative to the speed of light is defined as

$$\beta_{\mathrm{f}} = \sqrt{1 - \frac{4\, m_{\mathrm{f}}^2\, c^4}{s}}. \tag{2.6}$$

The couplings to the left-handed and right-handed fermion fields can, alternatively, be expressed in terms of a vector and an axial-vector coupling. In this notation, the neutral-current vector and axial-vector coupling constants, v_{f} and a_{f}, are given as

$$v_{\mathrm{f}} = \frac{I_3^{\mathrm{f}} - 2\, Q_{\mathrm{f}} \sin^2\theta_W}{2 \sin\theta_W\, \cos\theta_W} \quad \text{and} \quad a_{\mathrm{f}} = \frac{I_3^{\mathrm{f}}}{2 \sin\theta_W\, \cos\theta_W}, \tag{2.7}$$

where I_3^{f} is the third component of the weak isospin. Furthermore, χ is the

---

[3] To lowest order there are two additional t-channel diagrams with $\mathrm{e^+e^-}$ pairs in the final state.

propagator in the lowest-order Breit-Wigner[4] approximation,

$$\chi(s) = \frac{s}{s - m_Z^2 c^4 + i\, m_Z c^2\, \Gamma_Z} \tag{2.8}$$

The total width of the Z^0-resonance, Γ_Z, can be written in terms of partial widths,

$$\Gamma_Z = \sum_f \Gamma_{Z^0 \to f\bar{f}}, \tag{2.9}$$

where $\Gamma_{Z^0 \to f\bar{f}}$ is the partial Z^0 width into the fermion species f,

$$\Gamma_{Z^0 \to f\bar{f}} = \frac{\alpha}{3}\, N_c^f\, m_Z c^2\, \beta_f \left(\beta_f^2 a_f^2 + \tfrac{1}{2}\left(3 - \beta_f^2\right) v_f^2\right). \tag{2.10}$$

The first term in the square bracket of expression (2.5) corresponds to the photon annihilation diagram (fig. 2.2 a). The second term represents Z^0-production (fig. 2.2 b) and may be written in terms of Z^0 partial-widths by using equation (2.10). Thus, it is equivalent to

$$\sigma_Z = 12\,\pi\,(\hbar c)^2\, \frac{s}{m_Z^2 c^4}\, \frac{\Gamma_{e^+e^- \to Z^0}\, \Gamma_{Z^0 \to f\bar{f}}}{\left(s - m_Z^2 c^4\right)^2 + \Gamma_Z^2\, m_Z^2\, c^4}. \tag{2.11}$$

The third term of equation (2.5) is the interference of the γ and Z^0 exchange amplitudes.

Equation (2.5) was evaluated for different fermion species. The results are plotted versus the centre-of-mass energy, $\sqrt{s}$, in figure 2.3. The absolute value of the interference term is shown as a dotted line and is negligible in comparison to the term resulting from Z^0 production. It is exactly zero at the Z^0 pole. All data used in this thesis were taken at centre-of-mass energies between 88.2 GeV and 94.3 GeV with 91.1% of the events having centre-of-mass energies of (91.2 ± 0.2) GeV. At these energies, the contribution to the cross section from the photon exchange diagram is two orders of magnitude

---

[4] In lowest-order perturbation theory, the Z^0 resonance would enter the calculation as a δ function. In the Breit-Wigner approximation, this δ function is replaced by a function obtained from a perturbation expansion in quantum mechanical scattering theory that takes into account the finite lifetime of the state. In the Breit-Wigner function, the pole and the width of the resonance are free parameters.

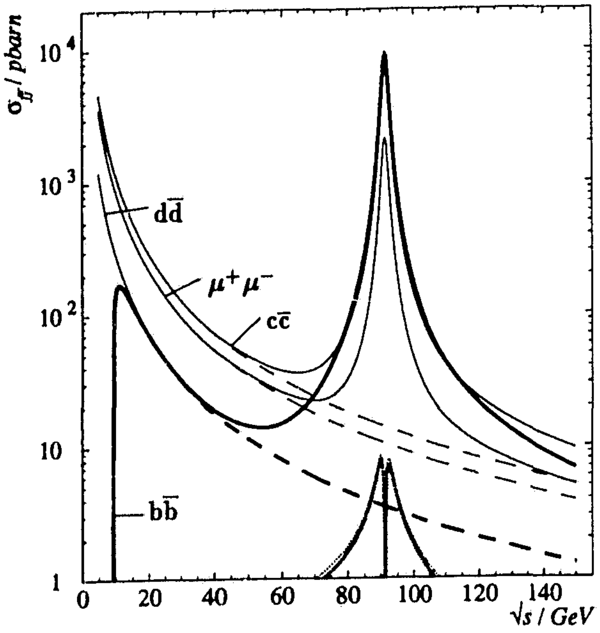

Figure 2.3: Cross Section *The lines are the total cross section for fermion-pair production to lowest-order Breit Wigner approximation. Dashed lines: contribution from photon exchange diagram. Dotted lines: absolute value of contribution from interference term. The unit of* 1 barn *denotes an area of* 10^{-28} m^2.

smaller than the contribution from the Z^0 exchange diagram and can be neglected (see fig. 2.3 dashed lines). Also, the effects due to the fermion masses are negligible since even for the heaviest accessible quark, the b quark, the production velocity, β_b, is close to the speed of light. To be precise, for centre-of-mass energies around $m_Z c^2$, β_b equals 0.994. Therefore, neglecting the term from the photon exchange diagram and the interference term and using the approximation $\beta_b = 1$, the cross section formula reduces to $\sigma_{f\bar{f}} = \sigma_Z$ (see eq. (2.11)). Correspondingly, equation (2.10) reduces to

$$\Gamma_{Z^0 \to f\bar{f}} = \frac{\alpha}{3} N_c^f m_Z c^2 \left(a_f^2 + v_f^2\right). \tag{2.12}$$

In comparison to the neglected terms above, the next-to-leading order diagrams[5] have a much more significant effect on the cross section. Initial state radiation (fig. 2.4) reduces the peak cross section by ≈ 30% and widens the Z^0 resonance peak towards higher energies since the emitted photon reduces the available energy at the e^+e^--Z^0 vertex. While the absolute cross sections

---

[5] Next-to-leading order diagrams are Feynman diagrams with one additional vertex such as the diagram shown in figure 2.4. These diagrams are suppressed by $\sim \sqrt{\alpha}$.

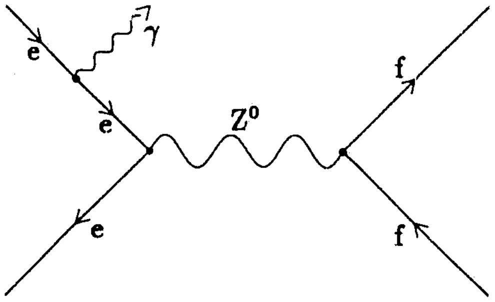

Figure 2.4: Initial State Radiation
The available energy at the e^+e^--Z^0 *vertex is reduced by initial state radiation. This has significant influence on the line shape. A typical Feynman diagram is shown.*

are reduced, the initial state radiation does not change the relative production rates for fermion pairs. Furthermore, these relative production rates are nearly independent of $\sqrt{s}$ at centre-of-mass energies close to the Z^0 resonance since the phase space for all fermion species is nearly identical.

QCD corrections affect only the total cross section and not the relative production rates of a quark species. The effect on the total cross section is on the order of $\alpha_s/\pi = 4\%$, where α_s is the strong coupling constant described in section 2.2.1.

The relative production rates of the quark species, therefore, are not sensitive to the above mentioned corrections and are less sensitive to experimental uncertainties than the total cross section measurement. The absolute number of produced and hadronically decaying Z^0 particles is easy to determine for the LEP experiments and is useful as a normalisation. The selection efficiency for multihadronic events at OPAL is estimated to be $(98.1 \pm 0.5)\%$ [14] and is not dependent upon the flavour of the primary quark pair[6].

The production probability for a particular quark pair $q\bar{q}$ relative to the multihadronic production probability reduces to

$$\frac{\sigma_{q\bar{q}}}{\sigma_{\text{had}}} = \frac{\Gamma_{q\bar{q}}}{\Gamma_{\text{had}}} = \frac{\Gamma_{Z^0 \to q\bar{q}}}{2\,\Gamma_{Z^0 \to q^{+\frac{2}{3}}\bar{q}^{-\frac{2}{3}}} + 3\,\Gamma_{Z^0 \to q^{-\frac{1}{3}}\bar{q}^{+\frac{1}{3}}}}. \tag{2.13}$$

---

[6] The so-called *flavour bias* correction of the multihadronic event selection accounts for variations of the selection efficiency that depend on the flavour of the quark pair produced in the Z^0 decay. It is determined to be smaller than 0.1% [14].

In terms of $\sin^2\theta_W$, the relative production rates are

$$\frac{\Gamma_{\mathrm{q\bar{q}}}}{\Gamma_{\mathrm{had}}} = 36\,\frac{I_3^{\mathrm{q}2} - 2\,I_3^{\mathrm{q}}\,Q_{\mathrm{q}}\sin^2\theta_W + 2\,Q_{\mathrm{q}}^2\sin^4\theta_W}{45 - 84\sin^2\theta_W + 88\sin^4\theta_W}. \tag{2.14}$$

The relative production rate for a $\mathrm{b\bar{b}}$ pair is estimated on the basis of this formula to be

$$\left.\frac{\Gamma_{\mathrm{b\bar{b}}}}{\Gamma_{\mathrm{had}}}\right|_{\mathrm{theo.}} = 0.2197 \qquad \left.\frac{\Gamma_{\mathrm{b\bar{b}}}}{\Gamma_{\mathrm{had}}}\right|_{\mathrm{OPAL}} = 0.2171 \pm 0.0030 \tag{2.15}$$

For comparison, the value measured by OPAL [14] is also given and is the value which will be used in this thesis.

2.1.2 Polarisation

As mentioned above, the Z^0 couples to left-handed and right-handed fermions with different strengths, resulting in a preferentially left-handed longitudinal polarisation of the fermion produced. Furthermore, the cross section is not symmetric in $\cos\theta$, where θ is the polar angle of the outgoing fermion with respect to the incoming electron. The cross section in the Born approximation (neglecting fermion masses) with respect to $\sqrt{s}$, $\cos\theta$ and the longitudinal polarisation states $p = \pm 1$, is calculated to be ([13] p. 237)

$$\begin{aligned} \frac{\mathrm{d}\sigma_{\mathrm{f\bar{f}}}}{\mathrm{d}\cos\theta}(s,\ \cos\theta,\ p) &= \frac{\pi\alpha^2(\hbar c)^2}{4s}\,N_c^{\mathrm{f}} \\ &\quad \Big\{ (1+\cos^2\theta)F_0^{\mathrm{f}}(s) + 2\cos\theta\ F_1^{\mathrm{f}}(s) \\ &\quad + p\left[(1+\cos^2\theta)F_2^{\mathrm{f}}(s) + 2\cos\theta\ F_3^{\mathrm{f}}(s)\right] \Big\} \end{aligned} \tag{2.16}$$

with the electroweak form factors

$$\begin{aligned} F_0^{\mathrm{f}}(s) &= Q_{\mathrm{e}}^2 Q_{\mathrm{f}}^2 + 2\mathrm{Re}(\chi(s))Q_{\mathrm{e}}Q_{\mathrm{f}}v_{\mathrm{e}}v_{\mathrm{f}} + |\chi(s)|^2\left(a_{\mathrm{e}}^2 + v_{\mathrm{e}}^2\right)\left(a_{\mathrm{f}}^2 + v_{\mathrm{f}}^2\right), \\ F_1^{\mathrm{f}}(s) &= 2\mathrm{Re}(\chi(s))Q_{\mathrm{e}}Q_{\mathrm{f}}a_{\mathrm{e}}a_{\mathrm{f}} + 4|\chi(s)|^2 a_{\mathrm{e}}v_{\mathrm{e}}a_{\mathrm{f}}v_{\mathrm{f}}, \\ F_2^{\mathrm{f}}(s) &= 2\mathrm{Re}(\chi(s))Q_{\mathrm{e}}Q_{\mathrm{f}}v_{\mathrm{e}}a_{\mathrm{f}} + 2|\chi(s)|^2\left(a_{\mathrm{e}}^2 + v_{\mathrm{e}}^2\right)a_{\mathrm{f}}v_{\mathrm{f}}, \\ F_3^{\mathrm{f}}(s) &= 2\mathrm{Re}(\chi(s))Q_{\mathrm{e}}Q_{\mathrm{f}}a_{\mathrm{e}}v_{\mathrm{f}} + 2|\chi(s)|^2 a_{\mathrm{e}}v_{\mathrm{e}}\left(a_{\mathrm{f}}^2 + v_{\mathrm{f}}^2\right). \end{aligned} \tag{2.17}$$

The $\cos\theta$ dependence of the cross section is often expressed as the *forward-backward asymmetry*

$$A^{\mathrm{f}}_{\mathrm{FB}}(s) = \frac{\int\limits_{0}^{1} \sigma_{\mathrm{f\bar{f}}}\ \mathrm{d}\cos\boldsymbol{\theta}\ -\ \int\limits_{-1}^{0} \sigma_{\mathrm{f\bar{f}}}\ \mathrm{d}\cos\boldsymbol{\theta}}{\sigma^{\mathrm{tot}}_{\mathrm{f\bar{f}}}} = \frac{3}{4}\frac{F^{\mathrm{f}}_{1}(s)}{F^{\mathrm{f}}_{0}(s)} \tag{2.18}$$

where both polarisation states are summed. For $\mathrm{b\bar{b}}$ production the forward-backward asymmetry varies between 0.03 at $\sqrt{s} = 88.2$ GeV and 0.16 at $\sqrt{s} = 94.3$ GeV.

The degree of longitudinal polarisation depends on θ as well as upon the available energy

$$\begin{aligned} A^{\mathrm{f}}_{\mathrm{pol}}(s,\cos\theta) &= -\frac{\mathrm{d}\sigma_{\mathrm{f\bar{f}}}(s,\cos\theta,p=+1) - \mathrm{d}\sigma_{\mathrm{f\bar{f}}}(s,\cos\theta,p=-1)}{\mathrm{d}\sigma_{\mathrm{f\bar{f}}}(s,\cos\theta,p=+1) + \mathrm{d}\sigma_{\mathrm{f\bar{f}}}(s,\cos\theta,p=-1)} \\ &= -\frac{(1+\cos^2\theta)F^{\mathrm{f}}_{2}(s) + 2\cos\theta\ F^{\mathrm{f}}_{3}(s)}{(1+\cos^2\theta)F^{\mathrm{f}}_{0}(s) + 2\cos\theta\ F^{\mathrm{f}}_{1}(s)}. \end{aligned} \tag{2.19}$$

For d-type quarks the average polarisation

$$< A^{\mathrm{d}}_{\mathrm{pol}}(s = m^2_{\mathrm{Z}}\,c^4) > = \int\limits_{-1}^{+1} A^{\mathrm{d}}_{\mathrm{pol}}(s,\cos\theta)\ \ \mathrm{d}\cos\boldsymbol{\theta} = -0.93. \tag{2.20}$$

The polarisation $A^{\mathrm{d}}_{\mathrm{pol}}(s,\cos\theta)$ is nearly independent of s and $\cos\theta$. In the range 88.2 GeV $< \sqrt{s} <$ 94.3 GeV, it varies less than 0.005 as a fluctuation of energy and less than 0.04 over the full range of $\cos\theta$. The average polarisation of d-type quarks is large due to the relatively small contribution from the electrical charge of $-\frac{1}{3}e$ compared to a relatively large coupling to the weak component of the electroweak force.

2.2 Theory of Strong Interactions

QCD is the Standard Model theory of strong interactions. It is based on a SU(3) nonabelian gauge symmetry describing the interactions between colour charged objects. As mentioned in the introduction, *colour charge* is a quantum number assigned to all fermions participating in strong interactions, and is similar to electrical charge for fermions participating in electromagnetic interactions or weak isospin characterising all fermions participating in weak interactions. In contrast to electrical charge, which appears in one variety (a multiple of the positron charge), colour charge appears in three varieties commonly referred to as red, green and blue. Antiparticles have the opposite electric charge of their corresponding particles. The same is assumed for the colour charge. For example, the antiparticle of a red d quark carries an antired colour charge. QCD requires all hadrons to be colour neutral. The basic colour relations for mesons are

$$c + \bar{c} = 0 \tag{2.21}$$

with c equals either of the three colours *r*ed, *g*reen or *b*lue at any given moment and for baryons

$$r + g + b = 0. \tag{2.22}$$

The only colour-carrying and therefore strongly-interacting fermions are the quarks. Quarks form a colour triplet. This means that each quark species can be subdivided into three colour groups. This is the origin of the *colour factor* $N_c^q = 3$ needed for the cross section calculations (2.5) to explain the relative production rates of leptons and hadrons.

The SU(3) structure of QCD leads to eight massless exchange bosons. These exchange bosons are called *gluons*. The gauge theory requires the gluons to carry colour themselves, allowing self interactions. The colour structure of the gluons is [15]: $g_{r\bar{b}}$, $g_{r\bar{g}}$, $g_{b\bar{g}}$, $g_{b\bar{r}}$, $g_{g\bar{r}}$, $g_{g\bar{b}}$, $g_{(r\bar{r}-b\bar{b})/\sqrt{2}}$ and $g_{(r\bar{r}+b\bar{b}-2g\bar{g})/\sqrt{6}}$. The self interaction of the gluons leads to a strong coupling constant that increases in strength as the energy increases. This leads to two major phenomena which distinguish strong interactions from other interactions:

1. *Confinement*, which means that quarks or gluons cannot exist as free objects. They are always bound into mesons or baryons. Other colour-neutral objects such as a $qq\bar{q}\bar{q}$ state are theoretically allowed but may not be energetically stable and have not yet been observed.

2. *Asymptotic freedom*, which refers to the phenomenon of a decreasing strong coupling constant $\alpha_s(Q^2)$ at high momentum transfer Q^2 in an

> interaction. High momentum transfer is equivalent to probing short distances. The interaction is asymptotic in the sense that $\alpha_s \to 0$ as $Q^2 \to \infty$.

Calculations in the framework of QCD are difficult. Nevertheless, at short distances ($\lesssim 0.2$ fm) α_s is small ($\lesssim 0.4$) due to asymptotic freedom and perturbation theory can be used as discussed in section 2.2.1. At larger distances, α_s grows and perturbation theory can no longer be applied. The interactions at these larger distance scales, commonly referred to as *fragmentation*, involve the formation of hadrons from quarks and gluons. QCD-inspired models are widely used to describe the fragmentation process. Some of these models are introduced in section 2.2.2. The perturbative stage and the fragmentation stage of the event evolution can be studied in combination using Monte Carlo techniques.

Monte Carlo simulation programs are used to build up a complex process from relatively simple single steps. In a Monte Carlo program, adjustable parameters are used to describe the poorly understood parts of a theory. They are chosen to fit the currently available experimental data. Such programs are widely used for event simulations. They provide an easy way of comparing theoretical predictions with experimental results and, therefore, can be used to determine detector efficiencies and to develop data selection criteria as is discussed in section 3.

The *JETSET* 7.3 Monte Carlo program is used extensively for the analysis described in the following chapters. This package belongs to the *Lund-family of Monte Carlo generators* that are characterised by being based on iterative cascade jet models using string dynamics [16]. The physical aspects of the JETSET program are summarised in this chapter. More detailed information can be found in [16, 17, 18, 19]. The technical aspects of the JETSET program are described in [20].

2.2.1 Perturbative QCD

As discussed above, α_s depends upon the energy transfer of the reaction. The energy variation or running of the constants can be pictured as the energy dependence of higher order corrections in the perturbation expansion.

The running strong coupling constant α_s for large Q^2 is approximately equal to [21][7]

$$\alpha_s(Q^2) \approx \frac{12\pi}{(33 - 2n_f)\ln\frac{Q^2}{\Lambda^2}} \tag{2.23}$$

where n_f is the number of kinematically accessible quarks[8]. At LEP energies $n_f = 5$, and Λ is a parameter defining the confinement scale. The value of α_s is determined experimentally and Λ can be computed from it. The best measured values at $Q^2 = m_Z^2 c^4$ are determined to ([2] p. 1299) be

$$\begin{array}{ccc} \alpha_s(Q^2 = m_Z^2 c^4) & = & 0.116 \pm 0.005 \\ \Lambda = \left(195\,^{+65}_{-50}\right)\ \mathrm{MeV} & \Longleftrightarrow & d = \dfrac{\hbar c}{\Lambda} = \left(1.01\,^{+0.34}_{-0.26}\right)\ \mathrm{fm} \end{array} \tag{2.24}$$

with d being the corresponding distance scale.

Reactions of the type $\mathrm{q} \to \mathrm{qg}$, $\mathrm{g} \to \mathrm{q\bar{q}}$ and $\mathrm{g} \to \mathrm{gg}$ can be calculated with perturbation theory as long as the perturbation expansion $\alpha_s(Q^2)/\pi \ll 1$ is still justified. The rates for $\mathrm{b\bar{b}}$ production by gluon splitting are very small due to phase-space suppression. The reaction rates for all of the above processes are needed for the development of Monte Carlo programs. Figure 2.5 shows an example of a typical event evolution in the perturbative QCD stage as simulated by JETSET. With increasing distance, perturbative QCD cannot be reliably applied and the system turns slowly into the fragmentation stage described in the next section.

---

[7] The complete expression can be found in [2] p. 1297 and depends upon the scheme of renormalisation used ([22] p. 157).

[8] An interesting consequence of the equation is that the phenomenon of asymptotic freedom occurs only if the number of different quarks, which are in the energetically accessible region of the experiment, is less than or equal to 16 ([23] p. 242).

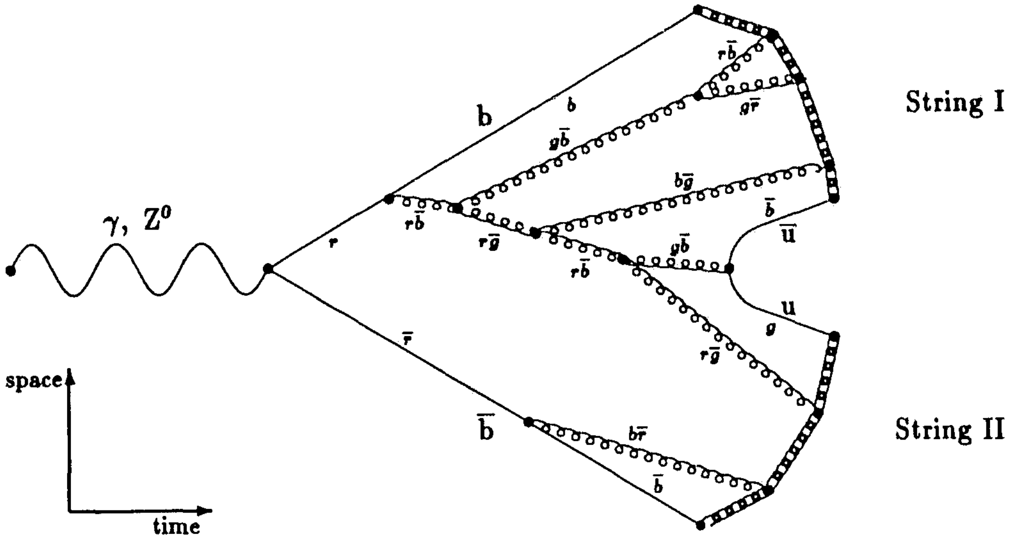

Figure 2.5: Domain of Perturbative QCD

Shown is a Monte Carlo simulated Z^0-decay into a $b\bar{b}$-pair in the domain of perturbative QCD. The colour flow of the system is given. At end of the perturbative QCD domain the system is assumed to form strings stretching between objects of opposite colour.

2.2.2 Fragmentation

For distances larger than ~ 0.2 fm between coloured objects, perturbative QCD becomes unreliable due to the growing coupling constant $\alpha_s(Q^2)$. It is not yet understood how to perform dynamical QCD calculations in this range. Several attempts, for example lattice QCD [24], have been made to deal with the non-perturbative aspects of the theory. In general, Monte Carlo programs use semi-empirical models such as the colour string model.

String Fragmentation

String models such as the Lund model used in the JETSET program assume that partons of opposite colour are connected by a massless string. Strings are assumed to be formed due to the increasing gluon self interaction when

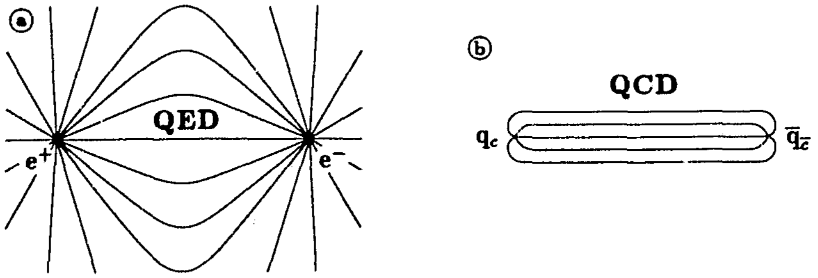

Figure 2.6: Comparison of QED and QCD Field Lines
Figure ⓐ shows typical electric field lines between two charged particles such as e^+ and e^-. In comparison the colour charge field lines of two quarks of opposite colour at large distance are drawn in ⓑ. QED field lines are spread throughout space since photons are uncharged and therefore not self interacting. The colour field lines are compressed due to the self interaction of the colour charged gluons.

objects of opposite colour are separated further than the confinement distance d (2.24). The gluon self interaction compresses the field lines of the colour force field as opposed to electric field lines which spread throughout space (see fig. 2.6). It is assumed in the model that colour strings behave like classical strings in the sense that they correspond to a constant force field which is equivalent to a linear potential.

Since gluons carry colour as well as anticolour charge, they must be connected to two other coloured objects by two strings. This leads to a situation where a chain of strings between a quark and an antiquark become stretched by the connected gluons (see fig. 2.5). If the quarks on the ends of the string chain are moving apart from each other, the single string parts are put under more and more stress until they break. This usually happens if the string exceeds a length of about 2 – 5 fm [17]. The string breaking process is identical to the generation of a new quark-antiquark pair out of the vacuum. Several string breakings may occur before the final hadrons are produced.

The actual string breaking process may be calculated classically as long as the quarks generated out of the vacuum are massless [16]. The situation changes drastically as soon as the new quarks are assumed to be massive. The energy for mass production needs to be taken out of the force field. Thus the

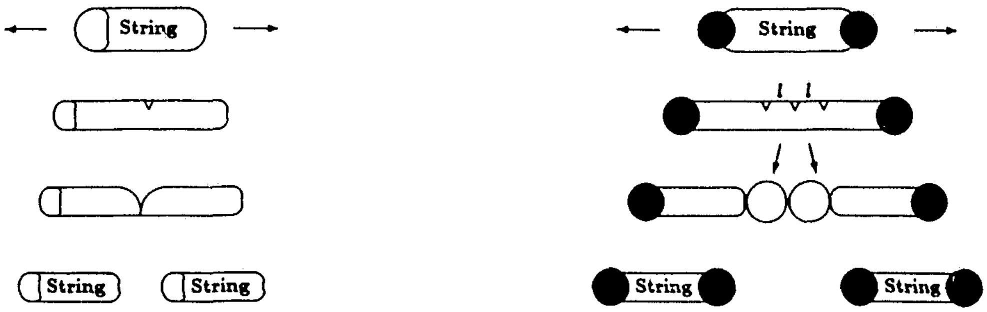

ⓐ Massless Quarks

ⓑ Massive Quarks

Figure 2.7: String Breaking

Massless quarks are being assumed at the end of the strings in figure ⓐ. The • in figure ⓑ indicate massive quarks. In the case of massive quarks, a piece of the string is needed for the creation of mass. Therefore, the breaking cannot happen at the same space-time point as indicated by the three cracks on the second line of figure ⓑ. These cracks are not causally connected and can only be interpreted as a quantum mechanical phenomenon.

quarks are produced at a distance $2l$ apart from each other, where

$$l = \frac{m_q\, c^2}{\kappa} \tag{2.25}$$

with the string tension $\kappa \approx 1$ GeV/ fm [17] and m_q being the constituent[9] quark mass. Therefore, the production process of massive quarks cannot take place at the same space-time point and must be seen as a quantum mechanical effect (see fig. 2.7). The production process is treated as a tunnelling process in a linear potential in the framework of the Lund model [16]. This leads to the following predicted suppression of heavy quark-flavour production in string

---

[9] Constituent quark masses are widely used in non-relativistic quark models. The current quark masses given in table 1.1 are derived from the QCD Lagrangian under chiral symmetry. In contrast, the constituent quark masses are determined from fits to the hadron mass spectrum using phenomenological potentials. The constituent quark masses used in the Lund model are: $m_u = 0.325$ GeV/c^2, $m_d = 0.325$ GeV/c^2, $m_s = 0.5$ GeV/c^2, $m_c = 1.6$ GeV/c^2 and $m_b = 5$ GeV/c^2.

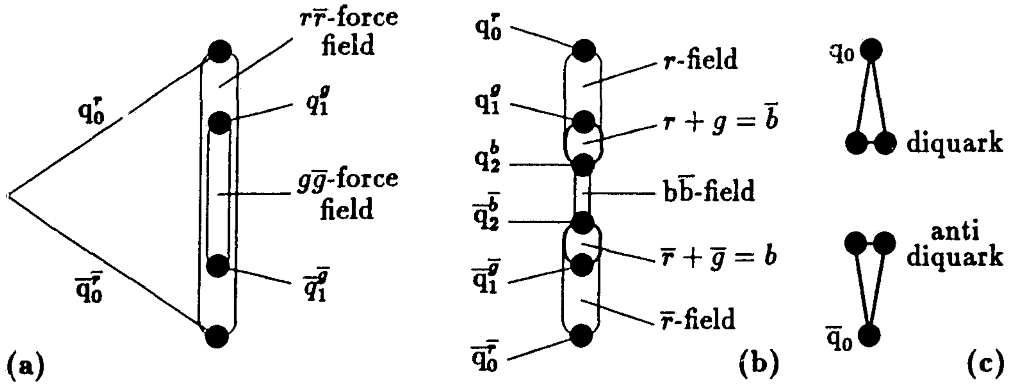

Figure 2.8: Diquark Production During String Fragmentation
Shown is the string breaking process in a popcorn model. (a) A green-antigreen quark pair appears as a fluctuation in a red-antired colour-force field between two quarks. (b) A blue-antiblue quark pair appears as second fluctuation. The net forces of the other two quarks pull on it. (c) The green and blue quarks form a diquark. Two baryons are formed if no further breakings occur.

decays[10]:

$$P(\mathrm{d}) : P(\mathrm{u}) : P(\mathrm{s}) : P(\mathrm{c}) \;\approx\; 1 : 1 : \frac{1}{3} : 10^{-11}. \tag{2.26}$$

The production of b quarks in string decays is even more strongly suppressed than c-quark production due to the high mass of the b quark.

In the Lund model all c and b quarks will either originate from the primary vertex or will be produced in the decay of a highly energetic gluon during the perturbative QCD stage, $\mathrm{g} \rightarrow \mathrm{q}\bar{\mathrm{q}}$. Matrix elements were calculated for $\mathrm{g} \rightarrow \mathrm{q}\bar{\mathrm{q}}$ reactions and are included in the JETSET program. Nevertheless, the probabilities for $\mathrm{b}\bar{\mathrm{b}}$-pair and $\mathrm{c}\bar{\mathrm{c}}$-pair production by gluon decays are low, meaning that essentially all b-flavoured quarks are predicted to originate directly from the annihilation process of the incident electron and positron.

---

[10] The relation $P(\mathrm{s})/P(\mathrm{u})$ in the JETSET may be changed using the PARJ(2) parameter.

Baryon Production

The Lund programs use a so-called *popcorn model* to describe baryon-antibaryon production [17, 25]. Popcorn models are based on the idea that in the colour field of, for example, a red quark q_0^r and a antired antiquark $\overline{q}_0^{\overline{r}}$, a green-antigreen quark pair $q_1^g\overline{q}_1^{\overline{g}}$ may appear as vacuum fluctuation (see fig. 2.8a). Usually this $g\overline{g}$-quark pair would not feel the $r\overline{r}$-colour force and would disappear again. But, if during the lifetime of the $g\overline{g}$ fluctuation another fluctuation of a blue-antiblue quark pair $q_2^b\overline{q}_2^{\overline{b}}$ appears, then the blue quark would feel the net colour force of the green and red quarks, due to the SU(3) relations (2.21 and 2.22):

$$\begin{aligned} b+g+r &= 0 \\ \underbrace{\overline{b}+b}_{=0}+g+r &= \overline{b} \\ \hookrightarrow \quad g+r &= \overline{b}. \end{aligned} \tag{2.27}$$

The same would happen to the antiquarks analogously (see fig. 2.8b). The b and $\overline{b}$ quarks get pulled out of the vacuum by the net colour force along with the g and $\overline{g}$ quarks. The q_2 and q_1 quarks are interpreted as a *diquark* (see fig. 2.8c). The likelihood of pulling a diquark pair out of the vacuum in relation to a single quark pair is suppressed by the higher diquark mass. The probabilities can be computed using the tunnelling mechanism mentioned in the previous section but some arbitrariness is involved in the calculation due to the choice of the diquark masses used. In the JETSET Monte Carlo program, the diquark versus single quark production ratio is set to $P(\mathrm{qq})/P(\mathrm{q}) = 0.1$. This parameter regulates the overall baryon production probability in the simulated events, a quantity that can be compared to the data. The name popcorn model was chosen because the strings connecting the new baryons may break again either between the quark and the diquark or within the diquark itself. An example of the popping mechanism is given in figure 2.9.

The likelihood of popping a quark-antiquark pair between a baryon pair is controlled in the JETSET program by the *popcorn parameter*. Its default value corresponds to a 50% probability of producing a meson between a baryon

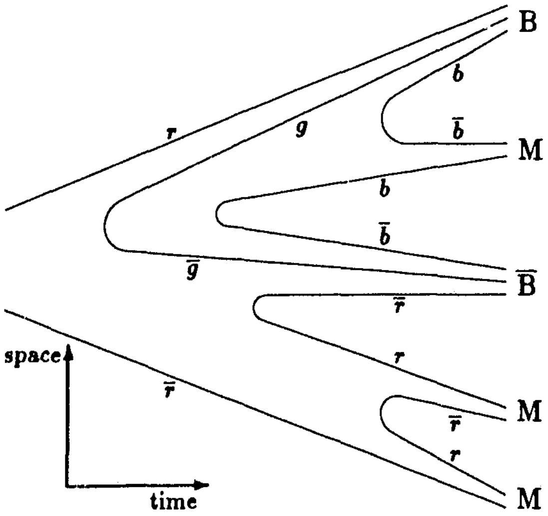

Figure 2.9: Popcorn Model
Baryons, B, *and mesons,* M, *are formed in the colour fields of two separating quarks by popping new quarks out of the vacuum. The letters represent the colours of the involved quarks. In the JETSET Monte Carlo program the probability for baryon production and the likelihood of producing a meson between a baryon pair, as in this example, is controlled by adjustable parameters.*

pair[11] (see fig. 2.9). Since the popcorn parameter regulates the production of additional particles between baryon-antibaryon pairs, it determines the degree of kinematic and geometrical correlation between them. In the background study in chapter 6, the popcorn parameter is varied in order to study systematic variations in the background levels caused by Λ particles that are produced during the fragmentation process and not as a decay product of a b baryon.

A list of the parameters used by the JETSET 7.3 program to regulate baryon production in the framework of the popcorn model, is given in table 2.1. More detailed information can be found in [17, 20].

Using the default JETSET parameter settings, the b-baryon production probability in $Z^0 \rightarrow b\overline{b}$ events is predicted to be $f(b \rightarrow \Lambda_b) = 8.5\%$. It is slightly lower than the diquark popping probability due to the kinematics of the string fragmentation process. The measured production rates of protons [27] and Λ particles [28] in Z^0 decays suggest that the heavy baryon production rates are overestimated by the JETSET simulation. In the studies, it was found that fewer protons and Λ particles with momenta above 4 GeV

---

[11] Meanwhile, the validity of the model has been checked in an OPAL study [26]. The data are found to be best described for a popcorn parameter setting that corresponds to a 80% probability of producing a meson between a baryon pair.

JETSET Baryon Production Parameters			
Relation	Name	Value	Description
$\frac{P(qq)}{P(q)}$	PARJ(1)	0.10	Diquark suppression factor.
$\frac{P(us)/P(ud)}{P(s)/P(d)}$	PARJ(3)	0.30	Extra suppression factor of strange diquark production.
$\frac{P((ud)_1)}{3P((ud)_0)}$	PARJ(4)	0.05	Suppression factor for spin 1 diquarks compared to spin 0 diquarks.
$\frac{P(BM\bar{B})}{2P(B\bar{B})}$	PARJ(5)	0.5	Popcorn parameter, regulating meson production between baryon pairs.

Table 2.1: Adjustable JETSET Parameters
The parameters controlling baryon production and their default values are given. These parameters may be changed by the user.

---

are found in the data than predicted by the JETSET simulation. Protons and Λ particles originating from b-baryon decays are preferably found in this momentum range. Since roughly a third of the protons and Λ particles in the momentum range above 4 GeV are predicted to originate from b-baryon decays, it is expected that $f(b \to \Lambda_b) < 8.5\%$. In chapter 7, $f(b \to \Lambda_b)$ is estimated from the data and will be compared to the JETSET prediction.

Momentum Distribution in String Fragmentation

The fragments of an ideal classical string would not have any transverse momentum in relation to the central axis of the string before breaking. The situation is different if the breaking occurs as a result of a quantum mechanical tunnelling effect, as needed for the generation of massive quarks. The tunnelling may occur asymmetrically, and transverse momentum is generated according to a Gaussian distribution reflecting the Heisenberg uncertainty principle. The combined transverse momentum of the generated quark-antiquark pair adds to zero. In general, the resulting transverse momenta are small in comparison to the large momenta of the quarks created in the Z^0 decays or the momenta of gluons created by hard gluon radiation in the stage of perturbative QCD. Therefore, hadronic events are characterised by a jet structure.

Since the acquired transverse momentum results from the string breaking, it is independent of the quark flavours at the ends of the original string. The situation is different for the longitudinal momentum transfer in a breaking string. In the case of a heavy quark pulling at the end of a string, most of the kinetic energy of the system is carried by the heavy quark and not by the string leading to a much *harder* momentum spectrum of hadrons containing a heavy quarks, meaning a momentum spectrum which peaks at larger values.

The momentum spectrum of hadrons which contain a heavy quark is found to be well described [29] by the quasi-empirical *Peterson fragmentation function* [30]:

$$\frac{\mathrm{d}N}{\mathrm{d}z} \propto \frac{1}{z\left(1 - \frac{1}{z} - \frac{\epsilon_{\mathrm{Q}}}{1-z}\right)^2} \tag{2.28}$$

with

$$z = \frac{E^{\mathrm{had}} + p_L^{\mathrm{had}}}{E^{\mathrm{available}} + p_L^{\mathrm{available}}}.$$

Here, E is the energy and p_L is the longitudinal momentum available in the fragmentation step or of the outgoing heavy hadron respectively. In the Peterson fragmentation function, ϵ_{Q} is the only free parameter and depends upon the constituent quark mass ratio of the heavy quark Q and the light quark q

$$\epsilon_{\mathrm{Q}} = \frac{m_{\mathrm{q}}^2}{m_{\mathrm{Q}}^2}. \tag{2.29}$$

For example, for assumed constituent quark masses of $m_{\mathrm{q}} = 0.350\ \mathrm{GeV}/c^2$ and $m_{\mathrm{b}} = 4.7\ \mathrm{GeV}/c^2$, a value of $\epsilon_{\mathrm{b}} = 0.0055$ is obtained.

2.3 Weak Hadron Decays

Weak decays of particles play an important role in this thesis. Their properties are discussed here briefly. Weak decays are characterised by their violation of parity and charge conjugation symmetry. Quark flavour-changing decays such as[12] $\mathrm{b} \rightarrow \mathrm{cW}^-$ and decays within a family such as $\mathrm{c} \rightarrow \mathrm{sW}^+$ or $\mu \rightarrow \nu_\mu \mathrm{W}^-$

---

[12] The $W^\pm$-particles in these examples are virtual and will decay immediately.

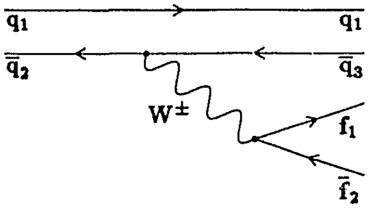

Figure 2.10: Weak Meson Decay
Depicted is the lowest-order Feynman diagram of a weak free quark decay. The quark q_1 is not directly involved in the decay process and is called the spectator quark.

are possible due to the weak charged current. Typical lifetimes are of the order of 10^{-12} s. The relatively long time scales of weak decays result from the large mass of the $W^{\pm}$ ((80.22 ± 0.26) GeV/c^2). The mass term enters inverse quadratically in the propagator and therefore to the fourth power in the lifetime calculation.

Of special interest for this thesis are free quark decays of the form $q_1\overline{q}_2 \rightarrow q_1\overline{q}_3 f_1 \overline{f}_2$ where q_1 does not participate in the decay process (see fig. 2.10). Models in which certain quarks do not participate in the decay process are called *spectator models*. The Feynman graph shown in figure 2.10 represents the amplitude of the lowest-order calculation, neglecting any QCD corrections. This is only a good approximation for heavy quark decays since the heavy quark carries most of the hadron momentum and is therefore less sensitive to QCD corrections. The theory based on this assumption is called *Heavy Quark Effective Theory* (HQET) [4]. The partial decay widths can be approximated in the framework of HQET by evaluating the Feynman diagram for the free quark decay and applying some corrections to account for the phase space and QCD effects afterwards.

As mentioned above, weak decays violate the conservation of quark flavour. This effect results from the quark mixing caused by the mass generation mechanism (see section 2.1). The mixing is parametrised by the CKM matrix:

$$\begin{pmatrix} d' \\ s' \\ b' \end{pmatrix} = \begin{pmatrix} V_{ud} & V_{us} & V_{ub} \\ V_{cd} & V_{cs} & V_{cb} \\ V_{td} & V_{ts} & V_{tb} \end{pmatrix} \begin{pmatrix} d \\ s \\ b \end{pmatrix} \tag{2.30}$$

$$= \begin{pmatrix} 0.9753(6) & 0.221(3) & 0.004(2) \\ 0.221(3) & 0.9745(7) & 0.040(8) \\ 0.010(6) & 0.039(9) & 0.9992(4) \end{pmatrix} \begin{pmatrix} \mathrm{d} \\ \mathrm{s} \\ \mathrm{b} \end{pmatrix}.$$

The values given are determined [2][13] from measurement and by requiring the matrix to be unitarity. The errors given in the parentheses after the numbers reflect the uncertainty of the last digit of the corresponding number at the 90% confidence level. Some of the values represent rather large errors, for example $\Delta V_{\mathrm{cb}} = 20\%$ at the 90% confidence level. Since the CKM-matrix elements are directly related to four of the fundamental parameters of the Standard Model, their precise determination is essential in order to test the model.

In particular, the CKM-matrix element, enters into the calculation of the Feynman diagrams as a factor determining the strength of the coupling between the W and the quarks. The partial width, therefore, depends quadratically on the CKM-matrix element. Using the values from equation (2.30) and neglecting phase space contributions, one estimates the probability of the b-quark decaying into a u-quark, $P(\mathrm{b} \to \mathrm{u})$, in relation to the probability of $P(\mathrm{b} \to \mathrm{c})$ in the spectator model to be[14]

$$\frac{P(\mathrm{b} \to \mathrm{u})}{P(\mathrm{b} \to \mathrm{c})} = \frac{V_{\mathrm{ub}}^2}{V_{\mathrm{cb}}^2} = 1\%. \tag{2.31}$$

The decay b → u is called CKM suppressed. As a consequence of this suppression, essentially all semileptonic b baryon decays are expected to be of the form

$$\Lambda_{\mathrm{b}} \to \Lambda_{\mathrm{c}} \ell^- \overline{\nu}.$$

Since the produced leptons do not interact by the strong force, the baryonic remains of the decay are assumed to be undisturbed and therefore form a c baryon. This provides the possibility to factorise the branching ratio

$$BR(\Lambda_{\mathrm{b}} \to \Lambda \ell \mathrm{X}) = BR(\Lambda_{\mathrm{b}} \to \Lambda_{\mathrm{c}} \ell \overline{\nu}) \times BR(\Lambda_{\mathrm{c}} \to \Lambda \mathrm{X}). \tag{2.32}$$

---

[13] All particle properties and other numbers are taken from this source, unless noted otherwise.

[14] So far the best measured value of $|V_{\mathrm{ub}}/V_{\mathrm{cb}}| = 0.08 \pm 0.02$, achieved by the CLEO and ARGUS collaborations. The error includes both experimental and theoretical uncertainties.

In the JETSET 7.3 Monte Carlo program all semileptonic b-baryon decays are of the above form.

In general, the partial width, $\Gamma_{\mathrm{X}\to\mathrm{y}}$, for the decay mode $\mathrm{X} \to \mathrm{y}$ can be extracted from the lifetime τ_{X} of the particle X and the branching ratio $BR_{\mathrm{X}\to\mathrm{y}}$ through the relations:

$$\tau_{\mathrm{X}} = \frac{\hbar}{\Gamma_{\mathrm{all}}} \quad \text{and} \quad BR_{\mathrm{X}\to\mathrm{y}} = \frac{\Gamma_{\mathrm{X}\to\mathrm{y}}}{\Gamma_{\mathrm{all}}}, \tag{2.33}$$

where Γ_{all} is the total width of X. In the case of semileptonically decaying b hadrons, such as $\Lambda_{\mathrm{b}} \to \Lambda_{\mathrm{c}}\ell^{-}\overline{\nu}$, the partial width can be approximated as a product of the terms arising from the free quark decay, the phase space corrections R, the square of the combined hadronic form factors F^2, and the QCD corrections η:

$$\Gamma_{\Lambda_{\mathrm{b}}\to\Lambda_{\mathrm{c}}\ell\overline{\nu}} = \frac{1}{192\pi^3}\,\frac{G_F^2\, m_{\mathrm{b}}^5\, c^{10}}{(\hbar c)^6}\,|V_{\mathrm{cb}}|^2 \times R(m_{\Lambda_{\mathrm{b}}}; m_{\Lambda_{\mathrm{c}}}, m_{\ell}, 0) \times F^2 \times \eta \tag{2.34}$$

where ℓ is a charged lepton and $G_F/(\hbar c)^3 = 1.166\,39 \cdot 10^{-5}\ \mathrm{GeV}^{-2}$ is the *Fermi coupling constant*. The hadronic form factors and the QCD correction term η are dependent upon the velocity transfer variable

$$\omega = \frac{m_{\Lambda_{\mathrm{b}}}^2 + m_{\Lambda_{\mathrm{c}}}^2 - q^2/c^4}{2\, m_{\Lambda_{\mathrm{b}}}\, m_{\Lambda_{\mathrm{c}}}} = \frac{E_{\Lambda_{\mathrm{c}}}^{*}}{m_{\Lambda_{\mathrm{c}}}\, c^2} \tag{2.35}$$

with q being the momentum transferred in the decay process and $E_{\Lambda_{\mathrm{c}}}^{*}$ being the energy of the Λ_{c}, measured in the rest frame of the Λ_{b}.

The equivalent expression for the decay $\overline{\mathrm{B}} \to \mathrm{D}^{(*)}\ell\overline{\nu}$ has been calculated in [31]. The resulting estimates of the form factors and the QCD correction, together with the ARGUS and CLEO measurements of the semileptonic branching ratio $BR(\overline{\mathrm{B}} \to \mathrm{D}^{*}\ell\overline{\nu}_{\ell})$ and the world average of the B lifetime measurements have been used to determine the best value of $V_{\mathrm{cb}} = 0.040 \pm 0.005$ [2].

Theoretically, the Λ_{b}^{0} system is better understood than b-meson systems. The light quarks in the Λ_{b}^{0} are assumed to be in a spin zero state while the spin of the Λ_{b}^{0} is identical to that of the b quark due to the decoupling of the heavy quark spin in HQET [32]. Furthermore, in the zero recoil limit, $\omega \to 1$, the

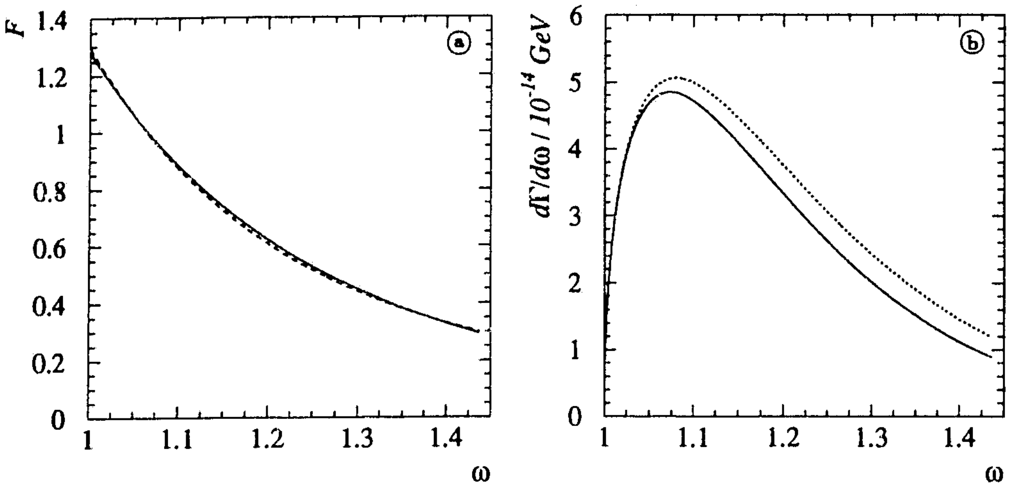

Figure 2.11: $\Lambda_b \rightarrow \Lambda_c \ell \bar{\nu}$ Form Factor and Differential Decay Rate
The solid lines are: ⓐ the form factor and ⓑ the decay rate for the decay $\Lambda_b \rightarrow \Lambda_c \ell \bar{\nu}$. *The curves are plotted with respect to the velocity transfer variable* ω *defined in (2.35). For the calculation of the curves the same parameters as in [6] have been used. The dashed line in ⓐ shows the approximate function described in the text. The dotted line in ⓑ was calculated without QCD corrections.*

---

differential decay rate becomes model independent and QCD corrections of the order $1/m$ disappear [6]. Eventually, semileptonic b-baryon decays will provide an alternative way of measuring V_{cb} with a smaller theoretical error [5, 6]. The effective form factor and the differential decay rate with respect to ω for the decay $\Lambda_b^0 \rightarrow \Lambda_c^+ \ell^- \bar{\nu}$ are calculated in [6] and are plotted versus ω in figure 2.11. In the default JETSET program no form factor corrections are made (this corresponds to a constant form factor) while simulating this decay. Therefore, special Monte Carlo samples have been generated to study the impact of the choice of form factor on the measurement. The details will be discussed in chapter 5. Since the actual expression for the effective form factor [6] is rather complicated, it has been approximated with a function of the form

$$F'(\omega) = \frac{1}{\lambda_1 + \lambda_2 \omega + \lambda_3 \omega^2} \tag{2.36}$$

to generate the special Monte Carlo samples. The parameters λ_i were determined by fitting the function to the theoretical curve. The values obtained are $\lambda_1 = 4.0065$, $\lambda_2 = -9.5466$ and $\lambda_3 = 6.3125$. The resulting function, F', drawn in figure 2.11ⓐ as a dashed line, agrees well with the full calculation.

For semileptonic b-baryon decays, the shape of the differential decay rate is complicated by the possible polarisation of the b baryons. The original polarisation of the b quark (discussed in section 2.1.2) may be carried through the fragmentation process and transferred to the b baryon. The kinematic properties of the polarised decay are discussed in [32]. In the JETSET default the semileptonic b-baryon decays are simulated, neglecting polarisation effects. The possible impact of polarisation effects on the product branching ratio measurement are discussed in chapter 5.3.

The partial width $\Gamma_{\Lambda_b \to \Lambda_c \ell \bar{\nu}} = 1.28 \cdot 10^{-14}$ GeV has been computed by numerically integrating the differential decay rate (2.34) over the allowed kinematic range

$$1 < \omega < \frac{m_{\Lambda_b}^2 + m_{\Lambda_c}^2}{2\, m_{\Lambda_b} m_{\Lambda_c}}, \tag{2.37}$$

where $m_{\Lambda_b} = 5.64$ GeV/c^2 and $m_{\Lambda_c} = 2.285$ GeV/c^2 have been used[15].

The QCD correction terms are not well understood. The differential partial width ignoring these terms is plotted as a dashed line in figure 2.11 for comparison. The integrated partial width changes by 11% if the correction terms are neglected. Using this value as the theoretical uncertainty, $V_{cb} = 0.040 \pm 0.005$ and the measured lifetime $\tau_{\Lambda_b} = (1.26 \pm 0.17)$ ps [33], the semileptonic branching ratio is given by

$$BR_{\Lambda_b \to \Lambda_c \ell \bar{\nu}} = (2.45 \pm 0.75)\%. \tag{2.38}$$

This value is significantly smaller than the value quoted in [32], which is calculated to be between 10% and 13% from semileptonic b meson decay rates. The JETSET 7.3 default value is $BR_{\Lambda_b \to \Lambda_c \ell \bar{\nu}} = 11.4\%$, based on similar arguments. Alternatively, a value of $(5.7 \pm 1.9)\%$ is obtained from [5] using the

---

[15] Reference [6] quotes a value of $\Gamma_{\Lambda_b \to \Lambda_c \ell \bar{\nu}} = 2.57 \cdot 10^{10} \mathrm{s}^{-1} \hbar = 1.69 \cdot 10^{-14}$ GeV using the CKM-matrix element $V_{cb} = 0.045$ and the QCD correction terms. Using the formulae given and the higher CKM-matrix element. I obtain the same value by neglecting the QCD correction terms.

above values of V_{cb} and τ_{Λ_b} and the vector meson dominance model. The large discrepancies between the numbers indicate the need for a measurement. In chapter 7, the different theoretical predictions of $BR_{\Lambda_b \to \Lambda_c \ell \bar{\nu}}$ will be compared to this measurement.

2.4 Outline of the Measurement

In this thesis, b baryons are identified by the charge correlation of an electron or a muon with a Λ particle. In general, the symbol ℓ for leptons will be used to represent the electron or the muon. Taus will only be considered as background in this context. The neutral Λ particles are identified via their prominent decay mode $\Lambda \to p\pi^-$ which has a branching ratio of $(63.9 \pm 0.5)\%$. Throughout this thesis, the charge conjugate modes will be considered, but not mentioned explicitly.

Leptons originating from b-hadron decays are typically of high momentum due to the hard fragmentation of b hadrons. Furthermore, they have a high average transverse momentum in relation to the jet of particles resulting from the b-hadron decay because of the mass differences between the b and c quarks. The lepton momentum and transverse momentum provide good criteria to select leptons originating from semileptonic b decays. This method of identifying b flavour is called *lepton tagging*. Baryons containing b quarks can be identified through the lepton tag in combination with a high momentum Λ in a jet close to the lepton. A typical decay chain of the events in question is

$$\begin{array}{lllll} \Lambda_b & \to & \Lambda_c & \ell^- & \bar{\nu} \\ & & \hookrightarrow & \Lambda & X \\ & & & \hookrightarrow & p\,\pi^- . \end{array} \tag{2.39}$$

Throughout this work the generic symbol Λ_b is used to represent all semileptonically decaying b baryons. This convention was chosen because no baryons with more than one heavy quark are produced in Z^0 decays due to the suppression of heavy quarks in the fragmentation process (see eq. (2.26)). Furthermore, all excited b baryons decay either hadronically or electromagnetically

a.) Spin $\frac{1}{2}$ States

Σ_b^- (bdd) Λ_b^0, Σ_b^0 (bud) Σ_b^+ (buu)
Ξ_b^- (bsd) Ξ_b^0 (bsu)
Ω_b^- (bss)

b.) Spin $\frac{3}{2}$ States

$\Sigma_b'^-$ (bdd) $\Sigma_b'^0$ (bud) $\Sigma_b'^+$ (buu)
$\Xi_b'^-$ (bsd) $\Xi_b'^0$ (bsu)
$\Omega_b'^-$ (bss)

Figure 2.12: b-Baryons and Their Quark Content
As discussed in section 2.2.2, heavy baryons with more than one c *or* b *quark are not expected to be produced in* Z^0 *decays. The spin* $\frac{3}{2}$ *states and all excited states decay hadronically or electromagnetically into the spin* $\frac{1}{2}$ *ground states. The same applies for the* Σ_b*, which decay into* Λ_b^0 *assuming their mass difference is sufficient. In this model, the only weakly decaying* b *baryons are the* Λ_b^0*, the* $\Xi_b^{-/0}$ *and the* Ω_b^-*.*

into one of the following particles: Λ_b^0, Ξ_b^-, Ξ_b^0 or Ω_b^-. These particles are the only weakly decaying b baryons. The quark content of these particles is given in figure 2.12. The production of Ξ_b and especially Ω_b is suppressed by the lower popping probability for diquarks containing an s quark. In Monte Carlo studies performed with JETSET, 88% of all weakly decaying b baryons are found to be Λ_b^0. The value appears to be in good agreement with recent results of the Ξ_b production rates at LEP [34].

The number of events containing a b baryon which decays semileptonically and has a Λ in the decay chain is given by

$$N = N_{\mathrm{had}} \times \frac{\Gamma_{b\bar{b}}}{\Gamma_{\mathrm{had}}} \times 2 \times f(\mathrm{b} \to \Lambda_b) \times BR(\Lambda_b \to \Lambda \ell X), \qquad (2.40)$$

with N_{had} being the total number of identified hadronic events and $\Gamma_{b\bar{b}}/\Gamma_{\mathrm{had}}$ being that given in equation (2.15). The factor of 2 is needed since a b baryon as well as an anti-b baryon could be produced in each $b\bar{b}$ event. It is assumed that no additional b quarks are produced by gluon splitting or in the fragmentation process. The number of semileptonically decaying b baryons which have a Λ in their decay chain, N, is estimated in this thesis leading to the determination of the product branching ratio $f(\mathrm{b} \to \Lambda_b) \times BR(\Lambda_b \to \Lambda \ell X)$. As discussed in chapter 1, $f(\mathrm{b} \to \Lambda_b)$ is the the probability of a b quark to be confined in a baryon and $BR(\Lambda_b \to \Lambda \ell X)$ denotes the branching ratio of b baryons into lepton and hadrons of which one decays subsequently into a Λ particle. In chapter 7, it will be outlined how to extract $f(\mathrm{b} \rightarrow \Lambda_{\mathrm{b}})$ and $BR(\Lambda_{\mathrm{b}} \rightarrow \Lambda_{\mathrm{c}}\ell\bar{\nu})$ from the obtained product branching ratio using other measurements.

The probability of a b quark to be confined in a baryon, $f(\mathrm{b} \rightarrow \Lambda_{\mathrm{b}})$, is an essential parameter of the proposed fragmentation model in the JETSET Monte Carlo program. As mentioned in section 2.2.2, a value of $f(\mathrm{b} \rightarrow \Lambda_{\mathrm{b}}) < 8.5\%$ is expected. The knowledge of the contribution of b baryons to the general b-hadron sample is not only of interest in the context of the fragmentation model but also of increasing interest for other analyses such as the determination of the average b-hadron lifetime [35] or the estimation of the b-baryon background by measuring b-meson oscillations at LEP [36].

As pointed out in section 2.3, the $BR(\Lambda_{\mathrm{b}} \rightarrow \Lambda\ell\mathrm{X})$ can be factorised into (eq. (2.32))

$$BR(\Lambda_{\mathrm{b}} \rightarrow \Lambda\ell\mathrm{X}) = BR(\Lambda_{\mathrm{b}} \rightarrow \Lambda_{\mathrm{c}}\ell\bar{\nu}) \times BR(\Lambda_{\mathrm{c}} \rightarrow \Lambda\mathrm{X})$$

assuming all b-baryon decays with a Λ in their final state have a c baryon as an intermediate state. The second term has been measured by the ARGUS and CLEO experiments [2], $BR(\Lambda_{\mathrm{c}} \rightarrow \Lambda\mathrm{X}) = (35 \pm 11)\%$. This measurement has not yet been entered into the JETSET 7.3 branching ratio tables. The default JETSET 7.3 value is 46.5%. Using the ARGUS and CLEO value [2], the first term can be compared to theoretical predictions and provides a test of HQET. Eventually, a sufficiently precise measurement may be used together with the b baryon lifetime measurement to determine V_{cb}.

Chapter 3

The OPAL Experiment

The LEP accelerator is used to generate the physical conditions of interest and, subsequently, the OPAL detector is used to observe them. The *raw data* collected are interpreted with a reconstruction program called *ROPE*[1], followed by a selection program used to select the events of interest. Figure 3.1 illustrates the data flow.

The analysis reported here uses the OPAL detector to identify electrons and muons as well as protons and pions from Λ decays. It requires a detailed understanding of the response of the detector with respect to particle type, momentum and direction. The accumulated knowledge of the detector response is incorporated in a Monte Carlo simulation program called *GOPAL*[2] [37]. The analysis uses the JETSET program to produce four-vectors to describe instances of the physical process being studied. The GOPAL program reads the four-vectors as input and simulates the appropriate detector response. The output of the GOPAL program has the same format as the raw data and therefore, the simulated events can be processed by the same event reconstruction program, ROPE. Processing the simulated events with the same reconstruction program as the data reduces possible sources of programming errors and makes it easier to compare data and Monte Carlo simulations. The ROPE output is

---

[1] **Reconstruction of OPAL Events.**

[2] **Geometry of OPAL.**

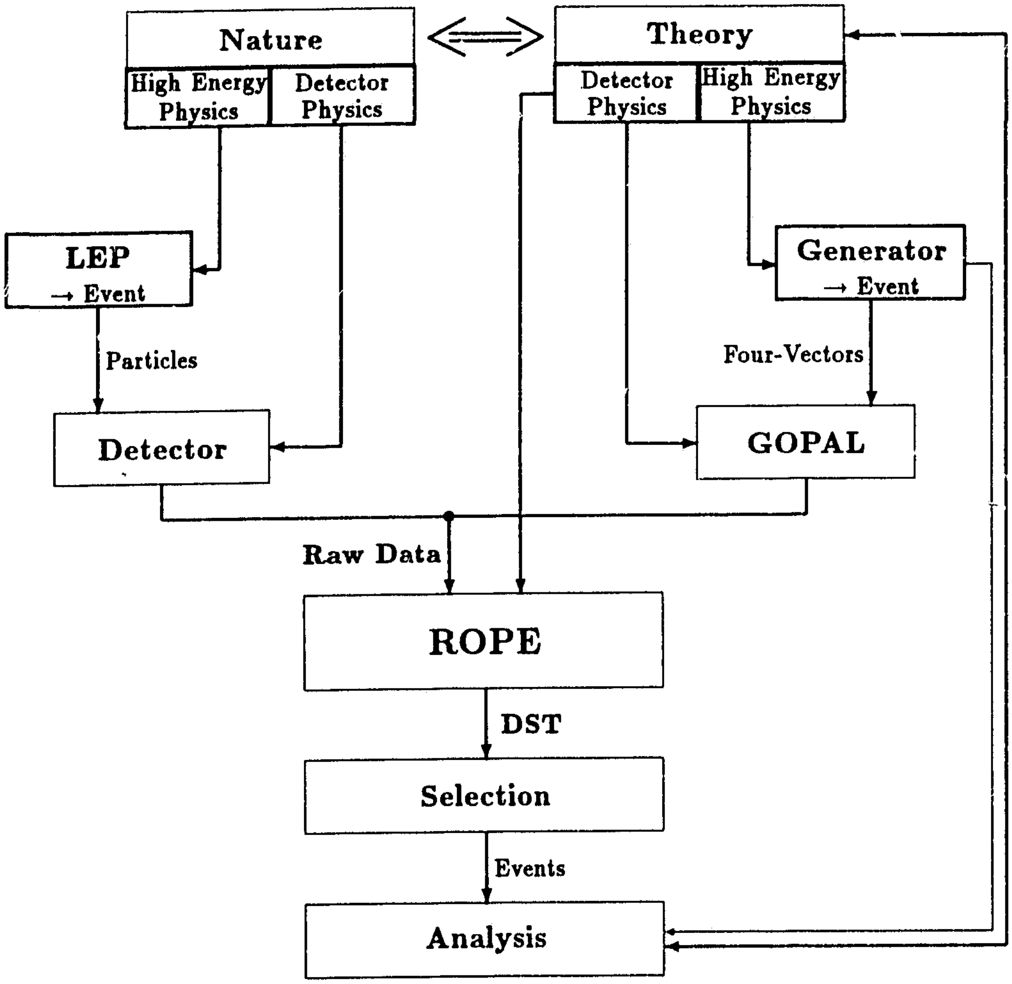

Figure 3.1: Information Flow in Experiment and Monte Carlo Simulation

The physics of interest is generated at LEP and observed with OPAL. The detector provides raw data which are processed through the event reconstruction program ROPE and passed on to an event selection program. In comparison, the theory is simulated by an event generator on a computer, which produces four-vector output. The output is passed to the detector simulation program GOPAL, which produces raw data of the same form as the detector. The simulated detector response is further processed in the same way as the data. Data and theoretical predictions are compared in the analysis and the results can be used to improve theoretical models.

Luminosity at OPAL		
Year	MH $/10^3$	$\int \mathcal{L}\,dt$ in 1/pb
1989	29	1.3
1990	148	6.8
1991	352	14.0
1992	767	25.1
1993	723	35.3
1994	1 715	57.9
1989-94	3 734	140.4

Table 3.1: Integrated Luminosity
In the table, MH denotes the numbers of recorded and identified multihadronic events. The time integrated luminosities recorded with OPAL are given in units of 1/pb *where* $1\,\mathrm{barn} = 10^{-28}\,\mathrm{m}^2$.

called a *DST*[3]. DSTs include only highly compressed relevant information for the different sub-detectors which are described in this chapter. This analysis is based completely on the information contained in the DSTs. The DSTs are processed through an event selection, which is described in detail in the next chapter.

3.1 LEP

The OPAL detector is one of the four general purpose detectors at LEP, the largest accelerator at the *CERN*[4] research laboratory. LEP has a circumference of 26.659 km and is buried between 50 m and 120 m underground in the Pays de Gex in France and in the Geneva canton in Switzerland. The huge circumference is required to reduce the energy loss of the beams due to synchrotron radiation. LEP is designed to be operated in two phases. The LEP1 phase started in 1989. It is designed to reach a centre-of-mass energy of up to 110 GeV, although no data have been recorded yet at centre-of-mass energies above 95 GeV. The machine has been upgraded with new superconducting cavities in preparation for LEP2 operation. For LEP2, it is planned

---

[3] Data Summary Tape.

[4] Centre Européenne pour la Recherche Nucléaire, European Centre for Nuclear Research, Geneva, Switzerland.

to reach centre-of-mass energies beyond the threshold for W^+W^- production. It is hoped this goal will be attained by 1996. So far LEP has been operated in either four bunch or eight bunch mode. In four bunch mode, four equally spaced bunches of electrons are accelerated and collide with the same number of counter-rotating positron bunches. The four multipurpose detectors, ALEPH[5][38], DELPHI[6][39], L3[7][40] and OPAL[8][41], are located at every other of the eight beam intersection points. In eight bunch mode, beam separators are used to avoid additional beam intersection points, which would disturb the bunches. In the future, the number of bunches in the machine will be increased by changing over to a bunch train operation. The time integrated luminosities (see p. 11) recorded by the OPAL experiment since the LEP startup in 1989 are listed in table 3.1. At the interaction points of the beams, the beams have typical dimensions of $\sigma_x = 130 - 200$ μm horizontally, $\sigma_y < 10$ μm vertically and $\sigma_z = 1\,300$ μm longitudinally [42]. The average beam currents of the e^+ and e^- beams respectively are about 3 mA.

3.2 OPAL

A complete description of the OPAL detector can be found in reference [41]. Only a short summary will be given here with emphasis on the descriptions of the detector components which are important for this work. A schematic drawing of the detector is given in figure 3.2. The main parts of the detector are, listed from the inside to the outside: the vacuum pipe, central tracking devices, solenoid, electromagnetic calorimeter, hadron calorimeter, and a muon detection system.

The OPAL coordinate system is defined as a right-handed orthonormal system with its origin at the geometrical centre of the detector. The positive

---

[5] Apparatus for LEP Physics.

[6] Detector with Lepton Photon and Hadron Identification.

[7] LEP 3 experiment.

[8] Omni Purpose Apparatus for LEP.

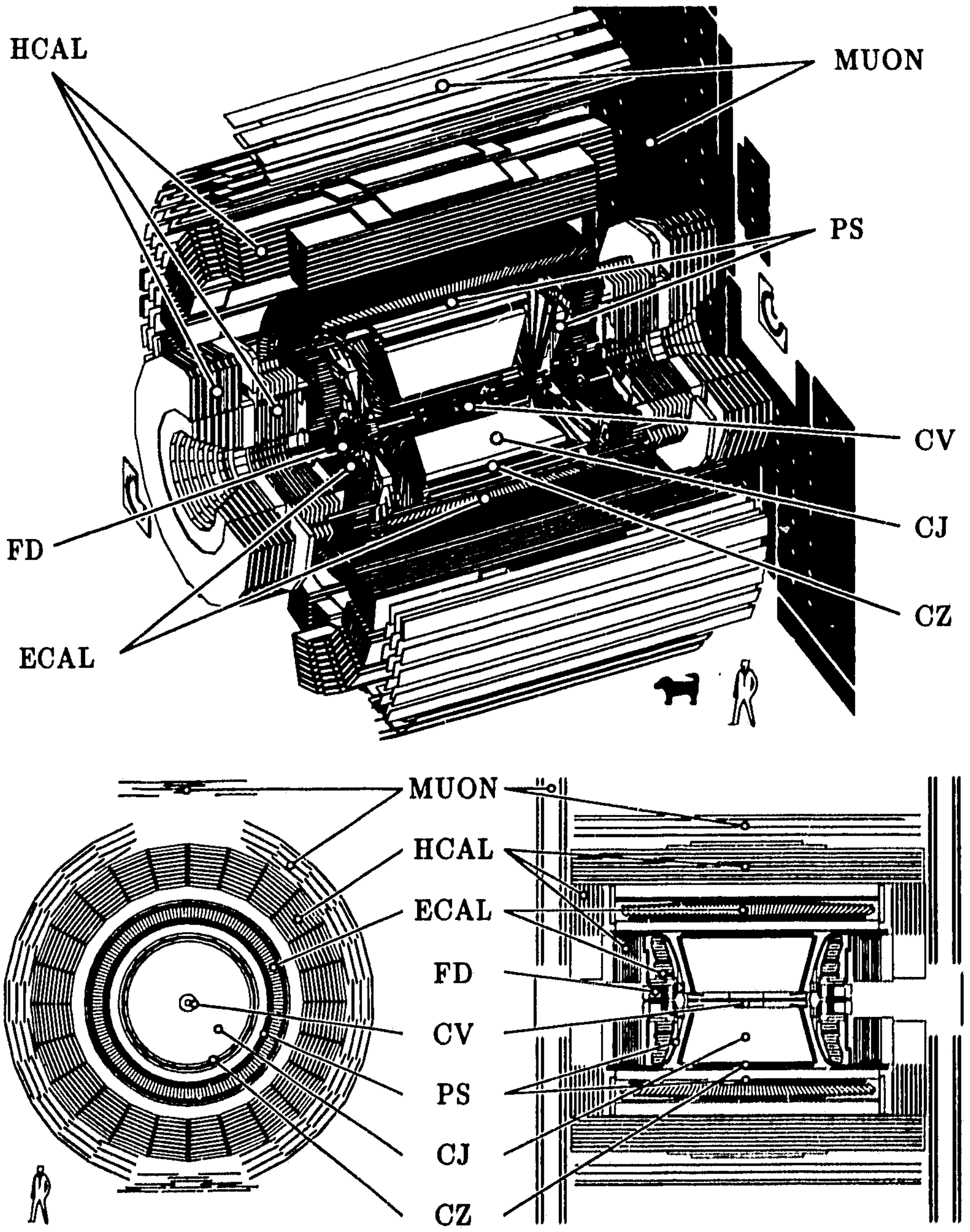

Figure 3.2: OPAL

Detector; cross section see from beam pipe; horizontal section seen from top. MUON: muon chamber, HCAL: hadron calorimeter, ECAL: electromagnetic calorimeter, FD: forward detector, CV: vertex detector, PS: presampler, CJ: jet chamber, CZ: z-chamber.

z axis lies along the electron beam direction, the x axis points toward the centre of the LEP ring, and the y axis points upwards. The symbols θ and ϕ denote the polar and azimuthal angles.

3.2.1 Central Detector

The central tracking detector measures the trajectories, momenta and the ionisation loss of charged particles. It consists of a silicon microvertex detector, a precision vertex detector, a large volume jet chamber, and z-chambers surrounding the jet chamber. The central detector is located inside the solenoid.

The silicon microvertex detector [43] was first installed for the 1991 data collection. It was mounted between the original aluminium-carbon fibre beam pipe at a radius of 7.8 cm and a new beryllium beam pipe at a radius of 5.35 cm. The silicon microvertex detector consisted of two cylinders with tangentially mounted silicon microstrip detectors. The inner cylinder has 11 detector planes called ladders at a radius of 6.1 cm and covers a polar angular range of $|\cos\theta| < 0.83$. The second layer consists of 14 ladders with an angular coverage of $|\cos\theta| < 0.77$. In its first version, the silicon microvertex detector measured the ϕ coordinate of tracks with a resolution of 10 μm. For the 1993 data run, the original silicon microvertex detector was replaced with a new one of the same dimensions and resolution but with additional z position capability. At the end of 1994 the silicon detector was damaged and removed. As a consequence, 20% of the data collected in 1994 were recorded without an operating silicon detector.

The Vertex detector is a cylindrical drift chamber with an inner radius of 8.5 cm and an outer radius of 23.5 cm. Its design is that of a scaled down jet chamber. The vertex detector consists of two layers each with 36 sectors in ϕ. The inner layer contains axial cells with 12 anode wires each. The outer layer consists of stereo cells, offset with an angle of 4° with respect to the z axis, with 6 anode wires each. The axial cells provide 50 μm resolution in the $r-\phi$ plane. The combination of axial cell and stereo cell information provides a position measurement with a z resolution of 700 μm.

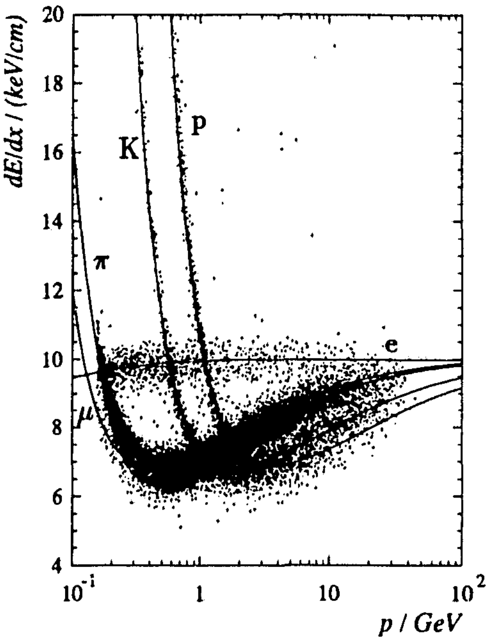

Figure 3.3: Ionisation Loss
A randomly chosen set of tracks of charged particles as they are measured in the OPAL jet chamber is used for the graph. The energy loss due to ionisation per distance travelled in the chamber gas is plotted versus the measured momentum of the particle. The theoretical expectation for each particle species [44] is shown as a line.

The jet chamber is a cylindrical drift chamber with an inner radius of 25 cm, an outer radius of 185 cm, and length 4 m. The endcaps of the cylinder are cone-shaped. The chamber consists of 24 sectors in ϕ each with 159 radially positioned sense wires. The sense wires are arranged parallel to the beam providing a $r - \phi$ measurement with a resolution of 135 μm on average. The z coordinate is determined by charge division with a resolution of 6 cm. An angular range of $|\cos\theta| < 0.731$ is covered by all 159 sense wires. Almost all (98%) of the full solid angle (4π) is covered by at least 8 sense wires. The z coordinate of a track in the endcap region of the jet chamber $0.731 < |\cos\theta| < 0.98$ is obtained from the position of the last sense wire registering the exiting track. Furthermore, the chamber is pressurised to four bars to enhance the measurement of the energy loss $\mathrm{d}E/\mathrm{d}x$ of charged particles in the chamber gas. This measurement can be used together with a momentum measurement to provide particle identification (see fig. 3.3). In cases where the $\mathrm{d}E/\mathrm{d}x$ measurement of a track is obtained from the information of all 159 signal wires, a $\mathrm{d}E/\mathrm{d}x$ resolution of 3.5% results for tracks in multihadronic events.

The z-chamber is used to determine the z coordinate at the exit point of a track from the barrel part of the jet chamber. The z-chamber consists of 24 drift chambers covering an angular range of $|\cos\theta| < 0.719$. The sense wires of the z-chambers are arranged orthogonal to those of the jet chamber. The z-chambers provide up to six spatial measurements per track. The resolution in z varies between $100 - 350$ μm depending on the position of the track. The ϕ coordinate of a track is measured by charge division. A resolution of 15 mm is obtained.

The solenoid is a conventional, water-cooled, aluminium solenoid which provides a uniform magnetic field of 0.435 T.

The momentum of charged particles is measured in the central detector by determining the curvature of the tracks in the plane perpendicular to the magnetic field and from the polar angle of the track. The momentum resolution in the xy-plane is $\sigma(p_{xy})/p_{xy} = \sqrt{(0.02)^2 + (0.0015\,p_{xy})^2}$, where p_{xy} is in units of GeV/c.

3.2.2 Calorimeter

Calorimeters measure the total energy of particles and provide information on particle identification. Because photons and electrons are electromagnetically interacting particles, their energies are best measured in an optimised electromagnetic calorimeter which is characterised by having a short radiation length. Short radiation lengths, which enhance the development of electromagnetic showers, are found in materials with high electron density. In contrast, hadron calorimeters are built from materials with large nuclear cross sections. The hadron calorimeters, which in general surround the electromagnetic calorimeters, measure the energy of hadrons and hadronic showers that penetrate the electromagnetic calorimeter. In the case of OPAL, the iron return yoke of the solenoid is instrumented with streamer tubes and serves as a hadron calorimeter. The electromagnetic calorimeter and the hadron calorimeter are described in more detail below.

The shower shape in the electromagnetic calorimeter is characteristic of the particle species entering the calorimeter and is used for particle identification. Good position resolution is needed to separate the signals of different particles. To improve the positional resolution of the electromagnetic calorimeter in OPAL and to detect showers that are initiated in material upstream of the calorimeters, a presampler is mounted between the solenoid and the electromagnetic calorimeter.

The presampler in the barrel region, $|\cos\theta| < 0.81$, consists of 16 drift chambers which are operated in limited streamer mode. In the endcap region, $0.83 < |\cos\theta| < 0.95$, the presampler is made of 32 multiwire chambers operated in high gain mode. The spatial resolution is approximately 5 mm for electromagnetic showers that are initiated in the pressure vessel of the central detector or in the solenoid.

The electromagnetic calorimeter is divided into a cylindrical barrel, covering the polar angle range of $|\cos\theta| < 0.82$, and annular endcaps, covering the range of $0.81 < |\cos\theta| < 0.98$. The barrel calorimeter consists of 9,440 lead glass blocks arranged in a nearly projective geometry. The projective geometry minimises the probability of a particle traversing more than one block. A non-perfect pointing geometry was deliberately chosen to prevent neutral particles from escaping detection through the gaps between the blocks. The lead glass has a characteristic radiation length[9] $X_0 = 1.5$ cm. The total depth for photons from the origin is $24.6\,X_0$ in the barrel region. The Čerenkov light produced by relativistic charged particles in the lead glass blocks is detected with phototubes. The energy resolution is $\sigma_E/E \simeq 2.3\%$ for beam-momentum electrons and $\sigma_E/E \simeq 10.5\%$ for electrons between 2 and 3 GeV/c.

The endcap electromagnetic calorimeter consists of 1,132 lead glass blocks of different length. The blocks are all mounted coaxial to the beam line. The average depth is $22\,X_0$ for photons which originate at the interaction point. The readout is accomplished with vacuum phototriodes which are capable of operating in the full axial magnetic field of the solenoid. At energies around

---

[9] The radiation length X_0 is defined as the mean distance in a material over which a high-energy electron loses all but $1/e$ of its energy through bremsstrahlung.

6 GeV, an energy resolution of $\sigma_E/E \simeq 5\%/\sqrt{E}$ is obtained where E is in units of GeV.

The hadron calorimeter consists of a barrel part covering a polar angular range of $|\cos\theta| < 0.81$, an endcap part covering $0.81 < |\cos\theta| < 0.91$ and a pole tip covering $0.91 < |\cos\theta| < 0.99$. All three parts are assembled as a sandwich structure, with alternating drift chambers and iron plates. The iron plates also serve as the return yoke of the magnetic field. The barrel part consists of 9 layers of chambers and 8 layers of iron plates. The endcap has 8 layers of chambers and 7 layers of iron plates. In both cases the chambers are operated in limited streamer mode. The iron absorber plates are 10 cm thick. The pole tip has 10 layers of multiwire chambers and 9 layers of iron plates. The multiwire chambers are operated in high gain mode and the iron absorber is 8 cm thick. The energy resolution of the hadron calorimeter is $\sigma_E/E \simeq 120\%$. The main use of the hadron calorimeter for this analysis is its supportive role in the identification of muons as minimally ionising particles.

3.2.3 Muon Detector

Muons of sufficient energy ($> \sim 3$ GeV) are capable of penetrating the entire detector. They are detected by the muon chambers surrounding the hadron calorimeter. Three major hadronic backgrounds were considered in the design of the muon chambers: hadrons that did not produce a hadronic shower in strong interactions with the material before the muon chambers; "punch-through" of hadrons that had interacted but produced secondary particles which escape the calorimeters and fake a muon; and pions or kaons that decayed in flight into muons. The backgrounds can be reduced by comparing signals in the muon chambers with tracks in the central detector. Good position resolution of the muon chambers is required to be able to match the tracks.

The muon detector consists of up to four layers of drift chambers in the barrel part, $|\cos\theta| < 0.72$, and four layers of limited streamer tubes in the endcap region, $0.67 < |\cos\theta| < 0.98$. The muon detectors do not cover the entire ϕ range of the detector due to the detector support structure and cables. However, 93% of the full solid angle is covered by at least one layer of the muon detector. The angular resolution for the muon barrel detector as well as for the muon endcap detector is 5 mrad.

3.2.4 Other Detector Components

A time of flight detector is located between the solenoid and the presampler. It consists of 160 scintillation counters and fast timing electronics and has an angular coverage of $|\cos\theta| < 0.82$. It serves mainly to veto events triggered by cosmic-ray muons.

Forward detectors are mounted close to the beam pipe at distances larger than 2 m upstream and downstream of the intersection region. They cover polar angles between 47 and 120 mrad. Their main purpose is to detect low angle Bhabha scattering events which are used to measure the absolute luminosity.

A silicon tungsten forward calorimeter [45] was installed in addition to the forward detector to improve the luminosity measurements of the 1993 scan of the Z^0 resonance. The silicon tungsten calorimeter covers polar angles between 25 and 60 mrad. The silicon microstrip detectors provide a more accurate measurement of the Bhabha scattering angle.

The trigger system in OPAL is characterised by a high degree of redundancy. This leads to high efficiency for all types of events and provides the possibility of determining the trigger efficiency using data. For hadronic events, the trigger efficiency is close to 100%, not counting dead-time due to data readout. The bunch crossing rate at LEP is 90 kHz for 8×8 bunch operations and the typical event rate is about 5 events per second.

The data acquisition system is capable of handling more than 150,000 analog signals per multihadronic event. This corresponds to several megabytes of data after digitalisation. Preprocessing before recording the data reduces the data size to about 50 kbytes per multihadronic event. The data are primarily stored on magneto-optical disks. A preliminary reconstruction of the events using the ROPE code is done within 2 hours of the data being taken.

Chapter 4

Data Sample and Event Selection

This chapter outlines the event selection procedure. The efficiencies for specific selection criteria are given in this chapter to illustrate the effect of the selection criteria. A complete discussion of the selection efficiency for the analysis is discussed in the next chapter.

4.1 Data Sample

This work is based on the data recorded at OPAL in the years 1990–1994. Only data which have been recorded while the central tracking chamber, the z-chamber, the electromagnetic calorimeters, the presamplers and muon detectors were operating properly are considered. When available, information from the silicon microvertex detector is used; otherwise the vertex information is taken from the vertex detector. About 80% of the data were taken with an operating silicon microvertex detector.

4.2 Hadronic Event Selection

The data are preselected with the standard hadronic event selection of the OPAL collaboration [46]. The criteria used for this selection are as follows:

✂ At least 5 tracks originating from the interaction region are required to be reconstructed in the jet chamber. *Tracks* are required to be determined using at least 20 *hits*[1]. A track is assumed to originate from the interaction region if it has a point of closest approach of $d_0 < 2$ cm and $|z_0| < 40$ cm. The *point of closest approach* is defined as the point on an extrapolated track that is closest to the nominal vertex. In cylindrical coordinates, d_0 and z_0 are the radial and z coordinates of that point.

✂ At least 7 energy *clusters* must be found in the electromagnetic calorimeter. A cluster in the barrel part of the electromagnetic calorimeter is defined as one or more neighbouring lead-glass blocks which contain a total energy deposit of at least 100 MeV. In the endcaps, a cluster is defined by a detected energy deposit of at least 200 MeV, spread over at least two neighbouring lead-glass blocks.

✂ The total energy deposit in the electromagnetic calorimeter has to be greater than 10% of the available centre-of-mass energy.

✂ The vacuum in the beam pipe is not perfect and the beams are not perfectly shaped. In order to reject interactions between the beams and residual gas atoms in the beam pipe, and reactions of off-momentum beam particles with the beam pipe, only events with an energy imbalance projected along the beam direction of

$$\frac{|\sum_i E_i \cdot \cos\theta_i|}{\sum_i E_i} < 0.65$$

are considered for the analysis. Here, E_i is the energy of an electromagnetic calorimeter cluster i and θ_i is its polar angle.

---

[1] The term hit denotes a registered signal on a sense wire.

- For b physics analysis, at least seven good charged tracks are required. A *good track* is defined as having the following properties:

  - a measured momentum, $p < 65$ GeV/c, to reject tracks that have momenta higher than the initial particles in the beam,
  - a measured momentum in the xy-plane $p_{xy} > 0.15$ GeV/c,
  - a $\chi^2_{xy}/DoF < 100$ in the xy-plane with respect to the points used for the track fitting,
  - and a point of closest approach to the nominal vertex, with $d_0 < 5$ cm and $|z_0| < 50$ cm.

After all these detector performance and data quality cuts, a total sample of $3,610,323$ multihadronic events remains. The efficiency of the hadronic event selection is $(98.1 \pm 0.5)\%$, and the background in the sample is less than 0.1% while the flavour bias (see footnote p. 15) for b-quark events is less than 0.1% [14].

4.3 Particle Identification

The criteria used to identify events containing b baryons via Λ-lepton correlation are outlined in detail below. The selection follows, in general, the method used in reference [9]. Improvements are made by using the lepton identification methods of references [47, 48] and by incorporating elements of the Λ identification method introduced in reference [28].

Only good tracks are considered when identifying lepton candidates. The electron and muon track candidates are required to have a measured momentum p_ℓ and transverse momentum p^t_ℓ that fulfil

- $p_\ell > 3$ GeV/c and
- $p^t_\ell > 0.8$ GeV/c.

The transverse momentum is measured with respect to the axis of the nearest jet. Jets are determined by the standard OPAL jet finder [49], which is based on the JADE algorithm [50]. The lepton candidates are included in the calculation of the jet direction. The requirements on the lepton momenta provide a b-enriched sample, since leptons coming from sources other than b decays have, on average, smaller total and transverse momenta. The efficiency of the two momenta criteria for leptons from b-baryon decays is approximately 50% and varies by about 2% depending on the polarisation of the b baryon. The total-momentum criterion alone has an efficiency of about $(70 \pm 5)\%$ depending on the degree of polarisation.

4.3.1 Electron Selection

Electron candidates are selected with the standard electron identification algorithm of the OPAL collaboration [47]. The criteria used in the algorithm are as follows.

- The momentum range of candidate tracks is further restricted by requiring $p_e < 40$ GeV/c. This reduces the background from badly measured tracks.

- The angular range is restricted to $|\cos\theta| < 0.715$ in order to limit the selection to well inside the coverage of the z-chambers.

- At least 3 z-chamber measurements are required for the candidate track in order to guarantee good momentum resolution and good matching between the candidate track and the electromagnetic calorimeter.

- The ionisation loss, $\mathrm{d}E/\mathrm{d}x$, of electrons in the jet chamber reaches the relativistic plateau at momenta below 3 GeV/c (see fig. 3.3). For electron momenta in the plateau region a constant value of $(\mathrm{d}E/\mathrm{d}x)_{\mathrm{exp}} = 10\,\mathrm{keV/cm}$ is expected. Electron candidates are retained if

$$\frac{\mathrm{d}E}{\mathrm{d}x_n} \geq -1.25$$

where $\mathrm{d}E/\mathrm{d}x_n$ is the normalised deviation to the expected value of the ionisation loss measurement of the candidate track,

$$\frac{\mathrm{d}E}{\mathrm{d}x_n} = \Delta\frac{\mathrm{d}E}{\mathrm{d}x}\bigg|_{\mathrm{norm}} = \frac{\mathrm{d}E/\mathrm{d}x - (\mathrm{d}E/\mathrm{d}x)_{\mathrm{exp}}}{\sigma(\mathrm{d}E/\mathrm{d}x)_{\mathrm{exp}}}. \tag{4.1}$$

The error on the expected value is calculated for each candidate as

$$\sigma(\mathrm{d}E/\mathrm{d}x)_{\mathrm{exp}} = \sigma(\mathrm{d}E/\mathrm{d}x)\,\frac{(\mathrm{d}E/\mathrm{d}x)_{\mathrm{exp}}}{\mathrm{d}E/\mathrm{d}x} \tag{4.2}$$

with $\sigma(\mathrm{d}E/\mathrm{d}x)$ being the measurement error of the candidate track. The criterion is chosen in order to optimise efficiency and purity of the selection (see ref. [47]). The value of -1.25 allows all candidates with measured $\mathrm{d}E/\mathrm{d}x$ values greater 10 keV/cm and also those with $\mathrm{d}E/\mathrm{d}x$ values close to 10 keV/cm, depending on the measurement uncertainty, to be retained in the sample.

✂ At least 40 measurements of the deposited charge must have been used for the calculation of the $\mathrm{d}E/\mathrm{d}x$ value of the candidate track.

✂ Electrons deposit most of their energy in the electromagnetic calorimeter. Electromagnetic showers are narrower in shape than hadronic showers. Most of the energy of a shower originating from an electron is located within a 30 mrad half angle cone around the electron's trajectory. The variable E_{cone} represents the measured energy inside such a cone around an extrapolated candidate track. The E_{cone} energy can be compared to the measured momentum, p, of the electron candidate track. The candidate is accepted if

$$\frac{E_{\mathrm{cone}}/p - (E_{\mathrm{cone}}/p)_{\mathrm{exp}}}{\sigma(E_{\mathrm{cone}}/p)} \geq -2$$

where $(E_{\mathrm{cone}}/p)_{\mathrm{exp}}$ is the expected value and $\sigma(E_{\mathrm{cone}}/p)$ is the measurement error of E_{cone} and p.

✂ Finally, candidates are rejected if they are likely to have originated from a photon conversion. The conversion-finding algorithm is described in [48]. A conversion is assumed if a second track of opposite charge forms a vertex with the candidate track inside the detector volume. The second track is required to have a $\mathrm{d}E/\mathrm{d}x$ value consistent with that expected for an electron. It has been found [48] that $(78 \pm 5)\%$ of the electrons originating from conversions are rejected by this algorithm.

The efficiency of the electron selection is about 41% for electrons from semileptonic Λ_b decays with momenta $p_e > 3$ GeV/c. Most of the efficiency loss results from the restricted θ range of the selection.

4.3.2 Muon Selection

Muon candidates are selected with the standard OPAL muon identification algorithm [48] which relies on the penetrating nature of muons. The most important selection criterion is the position matching of the extrapolated central detector tracks with track segments found in the muon chambers. The extrapolation of the tracks through the detector material is performed assuming the track is a muon and taking into account the magnetic field and multiple scattering effects. The position matching is described by the position separation variable χ_{pos} which is constructed from the azimuthal and polar distances, $\Delta\phi_{\mathrm{pos}}$ and $\Delta\theta_{\mathrm{pos}}$, between the extrapolated track and the found muon segment

$$\chi_{\mathrm{pos}} = \sqrt{\frac{(\Delta\phi_{\mathrm{pos}})^2}{\sigma^2(\Delta\phi_{\mathrm{pos}})} + \frac{(\Delta\theta_{\mathrm{pos}})^2}{\sigma^2(\Delta\theta_{\mathrm{pos}})}}. \tag{4.3}$$

The errors $\sigma(\Delta\phi_{\mathrm{pos}})$ and $\sigma(\Delta\theta_{\mathrm{pos}})$ are dominated by the extrapolation uncertainties.

For the selection, each track is associated with the muon segment for which it has the smallest χ_{pos} value. The selection criteria for muon identification are as follows:

✂ In the case of several tracks being associated with the same muon segment, the track with the closest extrapolation point is chosen as the muon candidate.

✂ $\chi_{\mathrm{pos}} < 3$ is required.

✂ To protect against certain rare cases such as punch-through of hadronic showers or coincident cosmic showers, less than 20 reconstructed muon segments within a 300 mrad strip in ϕ of the best-matched segment are required. This cut removes less than 1% of the candidates [48].

✂ The likelihood that a track is considered a muon according to the $\mathrm{d}E/\mathrm{d}x$ measurement, $\mathcal{P}_\mu(\mathrm{d}E/\mathrm{d}x)$, is required to be greater 5% if the $\mathrm{d}E/\mathrm{d}x$ value has been calculated using more than 20 ionisation loss measurements, and the obtained $\mathrm{d}E/\mathrm{d}x$ value is lower than the theoretical expectation for a muon candidate. This $\mathrm{d}E/\mathrm{d}x$ selection criterion reduces the number of kaons and protons that are misidentified as muons.

Furthermore, the central detector track of the muon candidate must have a point of closest approach of

✂ $d_0^\mu < 0.5$ cm.

The average efficiency of the muon selection is about 73% for muons with momenta $p_\mu > 3$ GeV/c.

4.3.3 Λ Selection

The Λ candidates are identified via the decay $\Lambda \to \mathrm{p}\pi^-$, which accounts for $(63.9\pm0.5)\%$ of all Λ decays [2]. The long mean lifetime of the Λ, 263 ps, means that most of the Λ particles decay inside the sensitive part of the detector. Furthermore, Λ particles, being electrically neutral, leave no tracks in the central detector. The proton and the pion created in the Λ decay are charged and result in the characteristic "Vee" structure of Λ decays inside the detector. An example of a low momentum Λ decay is given in figure 4.1. The selection used to extract Λ candidates combines elements of the selection described in reference [9] with those described in reference [28].

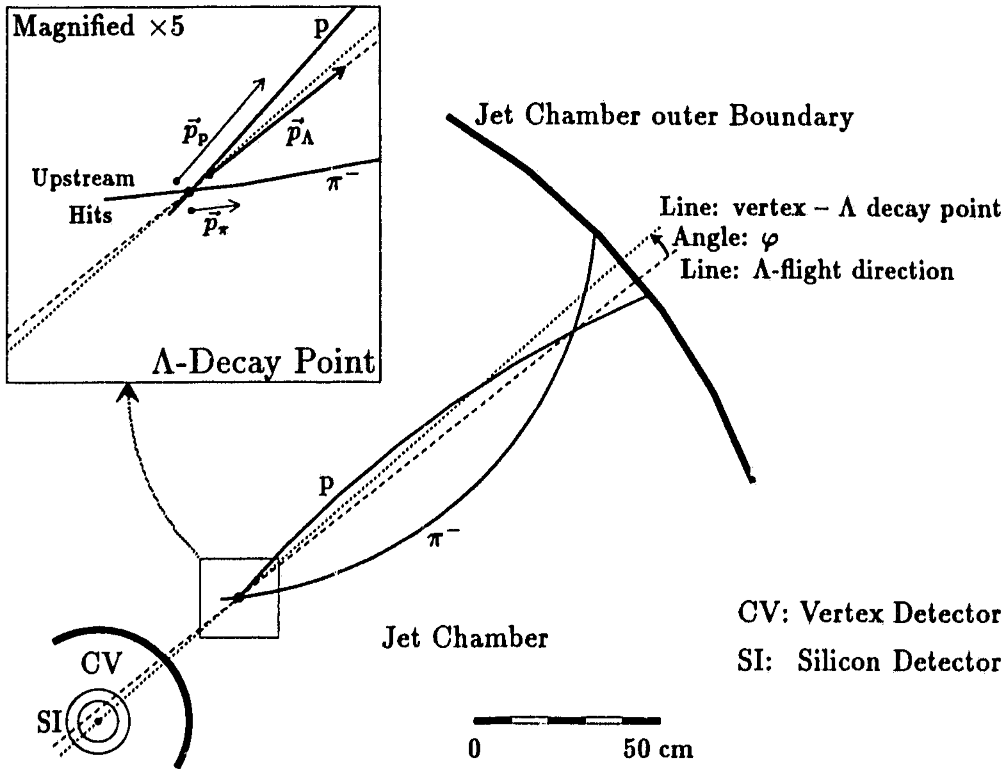

Figure 4.1: Geometry of a Λ Decay in the xy-Projection Plane

A neutral Λ particle decays inside the jet chamber into a proton and a charged pion. The decay point is found by intersecting the detected tracks. In the example, the track fitting algorithm associates hits with the pion track which are about 4 cm upstream from the intersection point with the pion track. The information on upstream hits is used as a veto in the Λ selection. The momentum of the Λ candidate is obtained by adding the momenta of the proton and the pion track candidates at the decay point. The Λ momentum direction is given by the dashed line and forms the angle φ with the line connecting the vertex with the Λ decay point (dotted line). The angle φ is small for a real Λ.

Λ Preselection

For Λ identification, all tracks found by the track-fitting algorithm that fulfil

- $|\cos\theta| < 0.96$ and
- $p_{xy} > 0.1$ GeV/c

are used as potential proton or pion candidates. All combinations of two such tracks with

- opposite charge

are considered as potential Λ candidates.

✂ Candidates are rejected if their trajectories do not have at least one possible intersection point in the xy-plane. If more than one intersection point is found, a decision is made based on the hit pattern in the jet chamber meaning that a potential intersection point is rejected if there are no hits close to it while there are hits close to the other candidate point. If a conclusive decision, according to the hit pattern, cannot be made, the Λ-decay point is chosen to minimise the angle φ, where φ is defined as the angle in the xy-plane between the estimated Λ flight direction and the line connecting the interaction point with the Λ-decay point (see fig. 4.1).

✂ Candidates are rejected if either the proton or the pion track has hits more than 5 cm upstream of the estimated Λ-decay point (see fig. 4.1).

After the Λ decay point is found, the z-momenta of the proton and pion candidates are recalculated under the constraint[2] that the tracks originate from the decay point. This leads to a significant improvement in the mass and momentum resolution of the Λ particles.

---

[2] In the OPAL standard Λ identification routine ID110, the tracks are only constrained to the new vertex in order to obtain the variable MLAMRV. In contrast, all quantities containing z-momentum information are calculated by using the constrained tracks in this analysis.

Of the two candidate tracks, the track with the higher momentum is assumed to be the proton candidate while the lower momentum track is assumed to be a pion. Due to the kinematics of the system, this assumption is correct for 99.9% of the Λ produced in b-baryon decays with momentum $p_\Lambda > 2.5$ GeV/c.

✂ In order to reduce random combinatorial background caused by pions from the primary vertex, the pion candidate is required to have a point of closest approach of $d_0^\pi > 0.1$ cm. This selection criterion is found from Monte Carlo studies to have a efficiency of 94% for Λ particles coming from Λ_b decays.

✂ The random combinatorial background is further reduced by selecting only those Λ particles with a 2-dimensional decay length of $l_\Lambda^{xy} > 5$ cm. The efficiency of this decay length criterion for Λ particles originating from semileptonic b-baryon decays is estimated to be 85%.

✂ For Λ candidates which decay before reaching the jet chamber, $l_\Lambda^{xy} <$ 25 cm, the beam interaction point is required to lie between the extrapolated trajectories of the proton and the pion track candidates. This is the case for 96% of all Λ particles in question.

✂ From kinematical considerations, it is expected that a Λ, produced in the decay chain of a b baryon, will keep the flight direction of the primary b baryon. This corresponds to small values of the above mentioned (p. 56) angle φ. The random combinatorial background is reduced further by requiring $\varphi < 14$ mrad. The efficiency of this selection criterion has been determined by Monte Carlo simulations to be 91%.

✂ The Λ is required to be well contained in the sensitive part of the detector. This is achieved by imposing $|\cos\theta_\Lambda| < 0.9$.

✂ The sample is further reduced by an initial momentum requirement of $p_\Lambda > 2.5$ GeV/c and a preliminary invariant mass restriction of $m_{p\pi} <$ 1.25 GeV/c^2, with p_Λ being the estimated momentum of the Λ candidate and $m_{p\pi}$ being the invariant mass of the proton-pion system under the proton and pion assumption.

The remaining sample of 1,865,564 Λ candidates will be referred to as the *preselected* Λ *sample* throughout the rest of the analysis. The selection criteria used so far are mainly dependent upon quantities measured in the xy-plane and are assumed to be well described by Monte Carlo simulations as will be discussed in the next chapter. To enhance the purity of the Λ sample, the following additional selection criteria are used.

Λ Main Selection

✂ To improve the mass and momentum resolution in the preselected sample, the proton and pion candidates both are required to have well measured z-momenta. This can be accomplished if the z-position of the exit point from the jet chamber is measured well. Each candidate track must be associated with at least 3 out of the 4 possible measurements from the z-chamber, if the track exited through the barrel part of the central detector. If the track exited through the endcap of the jet chamber, then the last sense wire which registered a hit belonging to the track must be clearly identified.

✂ The $\mathrm{d}E/\mathrm{d}x$ value of the proton track candidate is used to reject background from other physical processes such as $\mathrm{K}_s \to \pi^+\pi^-$ decays and γ conversion into $\mathrm{e}^+\mathrm{e}^-$ pairs. The following $\mathrm{d}E/\mathrm{d}x$ selection criterion is only applied if the $\mathrm{d}E/\mathrm{d}x$ value of the proton track candidate has been calculated from more than 20 ionisation loss measurements. Depending on the momentum, the criteria are:

✂ for $p_\mathrm{p} < 1.5$ GeV/c,

$$\mathrm{d}E/\mathrm{d}x > 8\,\mathrm{keV/cm} \quad \text{and} \quad \mathcal{P}_\mathrm{p}(\mathrm{d}E/\mathrm{d}x) > 0.5\%,$$

where $\mathcal{P}_\mathrm{p}(\mathrm{d}E/\mathrm{d}x)$ is the probability that a track is a proton based on its $\mathrm{d}E/\mathrm{d}x$ measurement,

✂ for $1.5\ \mathrm{GeV}/c < p_\mathrm{p} < 2.0\ \mathrm{GeV}/c$,

$$\mathrm{d}E/\mathrm{d}x < 8.5\,\mathrm{keV/cm},$$

✂ or for $p_\mathrm{p} > 2.0\ \mathrm{GeV}/c$,

$$\mathcal{P}_\mathrm{p}(\mathrm{d}E/\mathrm{d}x) > 5\% \quad \text{or} \quad \mathcal{P}_\mathrm{p}(\mathrm{d}E/\mathrm{d}x) > \mathcal{P}_\mathrm{K}(\mathrm{d}E/\mathrm{d}x),$$

where $\mathcal{P}_\mathrm{K}(\mathrm{d}E/\mathrm{d}x)$ is the probability that a track is a Kaon based on its $\mathrm{d}E/\mathrm{d}x$ measurement.

✂ The contamination of the sample from $\mathrm{K}^0_s \rightarrow \pi^+\pi^-$ decays, where one pion is misidentified as a proton, is decreased further by demanding

$$|m_{\pi\pi} - m_{\mathrm{K}^0}| > 6\ \mathrm{MeV}/c^2,$$

where $m_{\pi\pi}$ is the invariant mass of the system, assuming both tracks are pions, and m_K is the nominal K^0 mass of 497 MeV/c^2. This mass range corresponds to one sigma of the K^0-mass resolution.

✂ Of the remaining Λ candidates, only those with momenta $p_\Lambda > 4\ \mathrm{GeV}/c$ are retained. This selection criterion reduces the background caused by Λ particles that are produced directly in the fragmentation process and not within jets that resulted from secondary particle decays. Such Λ particles are commonly denoted as *fragmentation* Λ.

✂ Finally, a signal window as in reference [33] of

$$|m_{\mathrm{p}\pi} - m_\Lambda| < 7.8\ \mathrm{MeV}/c^2$$

is set. Henceforth, $m_{\mathrm{p}\pi}$ is the invariant mass of the proton-pion system and m_Λ is the nominal Λ mass of 1.1156 GeV/c^2.

The efficiency of the Λ selection depends upon momentum. It ranges from 22% for $p_\Lambda = 5.5$ GeV to 10% for high momentum Λ particles. The invariant mass distribution of the Λ candidates before selecting the mass range is shown in figure 4.2.

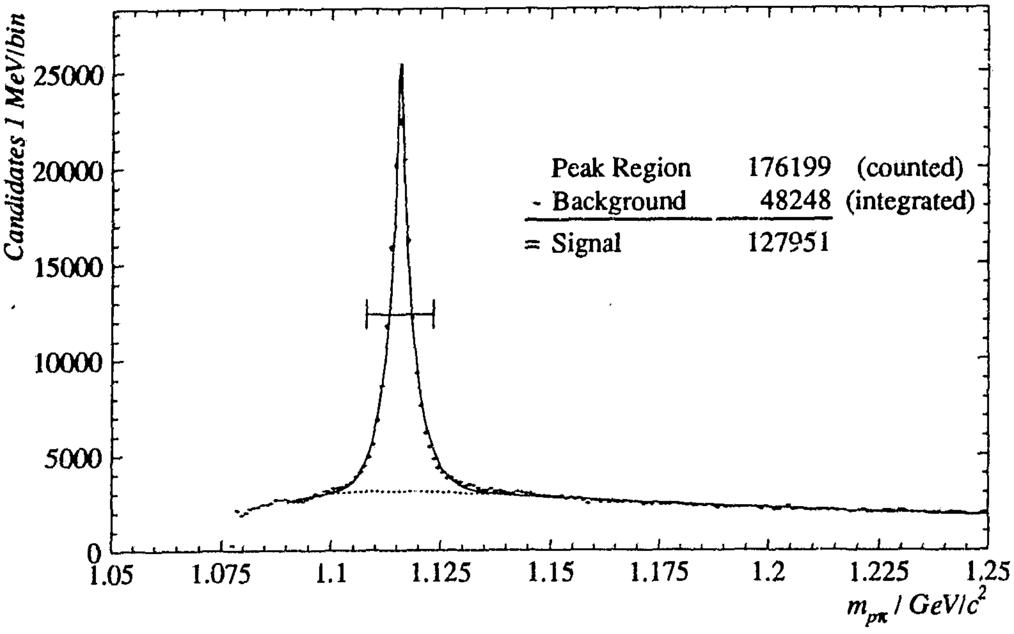

Figure 4.2: $p\pi^-$-Invariant Mass Distribution after Λ Selection

The signal window is ±7.8 MeV/c^2 *around the nominal* Λ *mass of* 1.1156 GeV/c^2. *The numbers given in the plot correspond to the number of events inside the window. The signal is obtained by subtracting the integrated background function from the number of candidates in the mass window. The function used to separate signal from background is described in the text.*

Determination of Λ Signal

To separate the signal from the background, a function is fitted to the data in the region of 1.09 GeV/c^2 $< m_{p\pi} <$ 1.25 GeV/c^2. The function used to model the background is described later. To describe the signal, the following ansatz is chosen. It is assumed that one of the Cartesian momentum components of the proton track is badly measured. The other two momentum components are assumed to be measured precisely. This ansatz is motivated by the significantly worse z-momentum resolution of the detector in comparison to the good x- and y-momentum resolutions, as discussed in chapter 3.2.1. In the selection, the track with the higher momentum is always assumed to be the proton candidate. The pion candidate therefore has less influence on the determination of the

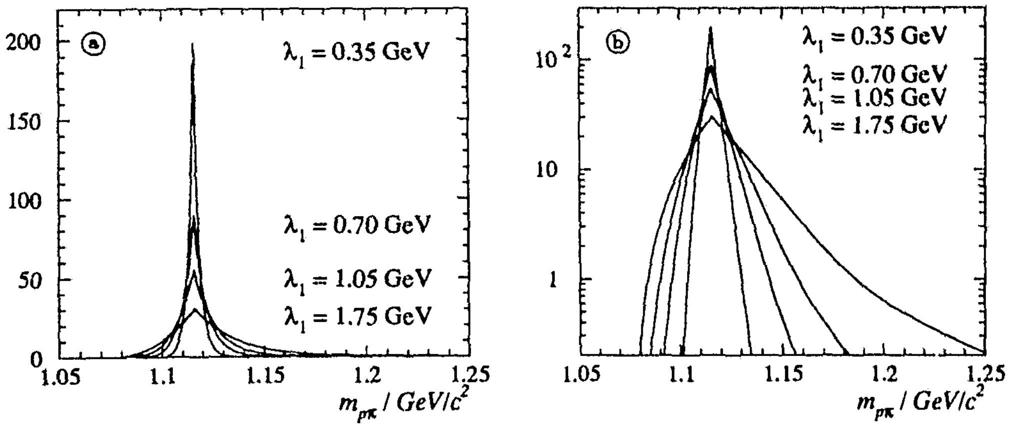

Figure 4.3: Examples of the Fitting Function Used to Describe the Λ Signal
In figure ⓐ a linear scale is chosen while in ⓑ the same functions are displayed using a logarithmic scale. The parameter λ_1 used to calculate an example is written beside the peak of the example function. It can be seen that the function respects the kinematical limits given by $m = m_p + m_\pi$. In case of the fit shown in figure 4.2, $\lambda_1 = 0.42$ GeV/c is found.

Λ momentum. For this reason the ansatz is made that the pion momentum is measured precisely. The one badly measured momentum component of the proton is assumed to be described by a Gaussian distribution. The width of the Gaussian, λ_1, is kept as a free parameter to be determined in the fit. The Gaussian has been analytically convoluted into the calculation of the invariant mass probability density function. The resulting signal function has the kinematically correct shape in the sense that the phase space cutoff of $m_p + m_\pi$ is respected. The asymmetry and the long tails of the Λ peak as observed in the data and as predicted by Monte Carlo simulations can be described by this ansatz. The shape of the fitted curve is controlled by only one free parameter, λ_1. A second free parameter, λ_2, is used to describe the absolute normalisation of the signal peak.

Quantities entering the calculation of the fit function such as the proton mass, m_p, the pion mass, m_π, and the nominal Λ mass, m_Λ, are chosen according to [2]. Furthermore, knowledge of the Λ energy, E_Λ, is required to perform the convolution. Nevertheless, the dependence of the functional shape upon E_Λ was found to be very small for values of E_Λ above 4 GeV. Significant changes of the function shape occur only if E_Λ is close to $m_\Lambda c^2$. Since only Λ particles with momenta $p_\Lambda > 4$ GeV are selected, it has been found sufficient to use the average energy of $E_\Lambda = 7$ GeV for Λ particles from b-baryon decays for the fit. Knowing all the masses of the particles involved in the decay process and E_Λ, the possible range of pion energies is calculated. If the Λ particles are assumed to be unpolarised then the pion energy probability density function is expected to be flat from two-body decay kinematics. The convolution requires an integration over all possible pion energies. This is done numerically in the fitting procedure. The shapes of the signal function obtained for different values of the parameter λ_1 are shown in figure 4.3. It can be seen that the overall kinematic behaviour of the signal function is correct in the sense that the phase space cutoff of $m_p + m_\pi$ is respected and the long tail in the invariant mass range above the nominal Λ mass as seen in Monte Carlo simulations is modelled by the function.

Alternatively, if one pion momentum component is assumed to be badly measured, only very minor differences in the shape of the function are found.

Monte Carlo simulations have been used to find an empirical function with a rather small set of free parameters that models the background shape independent of its composition. A function of the form

$$\mathcal{B} = \lambda_6 + \lambda_5 \left(\frac{\sqrt{x}}{x + |\lambda_3|} \right)^{\lambda_4} \qquad \text{with: } x = m_{p\pi} - (m_p + m_\pi) \tag{4.4}$$

was chosen, with λ_3 ... λ_6 being four more free parameters of the fit. Since the background function is rather flat compared to the signal function and therefore subject to less uncertainty, the signal contribution is estimated by counting the events in the signal window and subtracting the integrated background function from this number. The results of the procedure are given in figure 4.2. The χ^2/DoF of the fit equals 7.4 mainly due to the non-Gaussian tails in the momentum resolution. The non-Gaussian tails are caused by track fitting errors such as association of signals to the wrong track. The momentum resolution of tracks is found to be better described if two Gaussian distributions are assumed; the first Gaussian models the well measured tracks while the second Gaussian is wider and takes care of badly measured tracks. This ansatz translates into two signal functions. If accordingly a second signal function is added to the fit, a χ^2/DoF of 1.1 is obtained. Unfortunately, the fit becomes unstable for low statistics samples if two signal functions are used because the parameters of the two signal functions are highly correlated. Therefore, a six-parameter fit is used based on a single signal function.

4.4 Λ-Lepton Correlations

As a final step, correlated Λ and lepton candidates are selected through the following criteria:

✂ The angle between the Λ and the lepton has to be less than 50°. The efficiency of this selection criterion is nearly 100% for $p_\ell > 3$ GeV/c and $p_\Lambda > 4$ GeV/c.

✂ The invariant mass of the Λ-lepton system is restricted to

$$m_{\Lambda\ell} > 2.2 \text{ GeV}/c^2.$$

This requirement eliminates the potential background from $\Lambda_c^+ \to \Lambda\ell^+\nu X$ events. The efficiency of this selection criterion, after all previously discussed selection criteria have been applied, is about 85%, calculated from Monte Carlo studies. It varies by about 2%, depending on the degree of Λ_b polarisation and the form factor used to model the energy transfer from the b baryon to the c baryon.

✂ Finally, the combined momentum of the Λ-lepton system is restricted by

$$p_{\Lambda\ell} > 9 \text{ GeV}/c$$

in order to reduce random combinatorial background. The efficiency of this final selection criterion is about 97% after all previous selection criteria have been applied.

After the selection, the remaining candidates are split into a *right-sign sample* ($\Lambda\ell^-$, $\overline{\Lambda}\ell^+$) and a *wrong-sign sample* ($\Lambda\ell^+$, $\overline{\Lambda}\ell^-$) according to their charge correlation. The events in the right-sign sample are potential b-baryon candidates (see eq. 2.39) while the wrong-sign sample can only arise from background. The proton-pion invariant mass distributions for the right-sign and the wrong-sign Λ-lepton sample are shown in figure 4.4. The peak in the wrong-sign sample is due to events in which a Λ is erroneously associated with a lepton candidate. The background reactions responsible for the effect, will be discussed in detail in chapter 6. A total of 734 right-sign and 327 wrong-sign combinations are found inside the mass window as indicated in table 4.1.

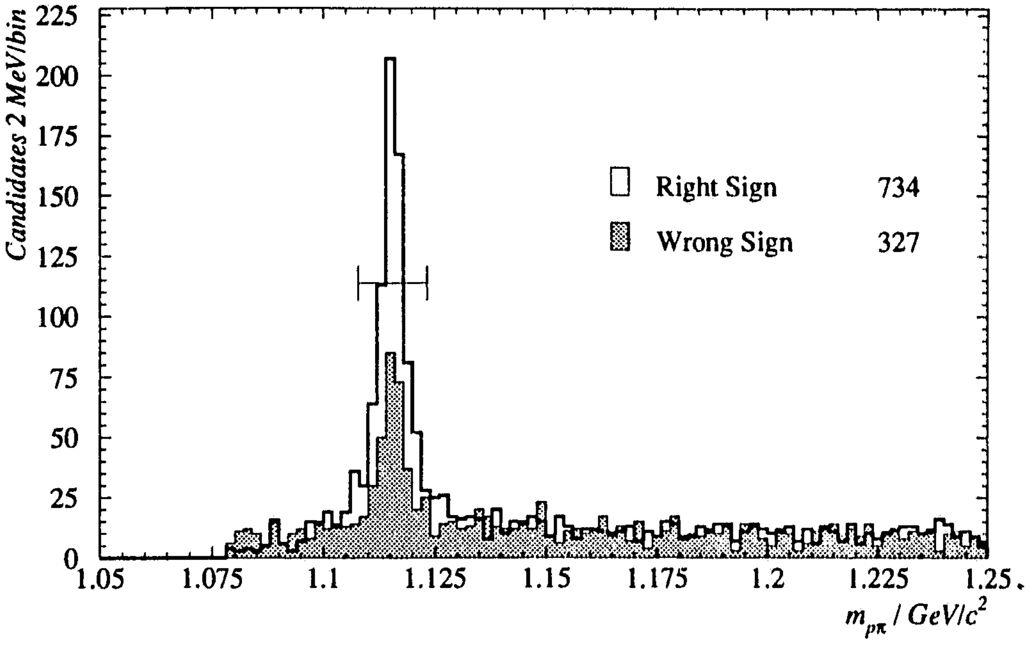

Figure 4.4: pπ-Invariant Mass Distribution for Λ-Lepton Correlations
Shown is the proton-pion invariant mass distribution of the right-sign and wrong-sign sample with no Λ mass window being set. Monte Carlo studies indicate that the peak in the wrong-sign sample is due to events in which a Λ is erroneously associated with a lepton candidate.

Selected Events					
	#e$^-$	#e$^+$	#μ^-	#μ^+	Combined
Right-Sign	144	124	223	243	734
Wrong-Sign	62	66	93	106	327

Table 4.1: Selected Λ-Lepton Correlation
Given are the numbers of Λ-lepton correlations found within the mass window for the different charges of the leptons after applying all selection criteria.

Chapter 5

Determination of the Efficiency

The selection efficiency is determined from Monte Carlo simulations. This approach is chosen because most of the selection criteria are correlated. Furthermore, the efficiency depends on the kinematic variables describing the event. These correlations and kinematic dependencies are taken into account by simulating b-baryon events, processing them with the detector simulation program and applying the same selection criteria to the simulated events as to the data. The efficiency can then be calculated using

$$\varepsilon_{\Lambda\ell} = \frac{n_{\text{out}}}{N_{\text{in}}} \tag{5.1}$$

where N_{in} is the number of simulated semileptonic b-baryon decays with a Λ in their decay chain and n_{out} is the number of those reactions that remain after all the selection criteria are applied. The limitations of this approach result from model uncertainties in the Monte Carlo generator and from imperfect knowledge of the detector response.

The different sources of uncertainty in the efficiency calculation are outlined in this chapter, and their effects on the efficiency are determined. The resulting efficiencies are

$$\begin{aligned} \varepsilon_{\Lambda e} &= 0.0378 \pm 0.0031, \\ \varepsilon_{\Lambda \mu} &= 0.0602 \pm 0.0047 \end{aligned} \tag{5.2}$$

for the Λ-e and Λ-μ samples respectively. The error includes both Monte Carlo statistics and the systematic uncertainties of the method. The efficiency for the Λ-e correlations is lower than for the Λ-μ correlations due to the restricted angular acceptance of the electron identification algorithm. The overall efficiency is rather low due to three effects. One is the undetected $\Lambda \rightarrow n\pi^0$ decay mode (35.8%), another is the long lifetime of the Λ, which means that many decays lie outside the sensitive detector volume, and finally the stringent kinematic selection criteria.

5.1 Monte Carlo Samples

The selection efficiency and sources of uncertainty in its determination are investigated by the use of several samples of Monte Carlo simulated events. All of these Monte Carlo samples have been generated with the JETSET Monte Carlo program using the Peterson fragmentation function for $Z^0 \rightarrow b\bar{b}$ and $Z^0 \rightarrow c\bar{c}$ events (see chapter 2.2.2). Three of these Monte Carlo samples have been processed with the full detector simulation and are described below. In contrast, several other special purpose Monte Carlo samples have been processed with the smear-mode of GOPAL. In the *smear-mode*, GOPAL does not simulate the full detector response but rather smears the input four-vectors according to empirical detector response functions [37]. The smear-mode consumes significantly less computing time and therefore larger samples may be generated. The samples produced with the smear-mode of GOPAL are described later.

Of the three samples that have been generated with the full detector simulation, sample 1 is denoted as the "*general multihadronic sample*" and consists of $2,341,732$ simulated multihadronic events. The flavour of the primary produced quark pairs has been chosen according to the Standard Model predictions.

Samples 2 and 3 are special Monte Carlo samples consisting of $56,310$ and $41,905$ simulated events respectively. In these samples, each event includes at least one semileptonically decaying b baryon with a Λ in its decay chain. The lifetime of the Λ_b^0 was set to 1.4 ps. The decay of the Λ_c^+ particle was simulated with the *EURODEC* package [51] with the decay tables modified to the more recent values given by the Particle Data Group (1992) [52]. The modifications result in the following ratio for Λ_c decays into Λ particles,

$$\frac{BR(\Lambda_c^+ \to \Lambda X)_{\mathrm{direct}}}{BR(\Lambda_c^+ \to \Sigma^{*0} X) \cdot BR(\Sigma^{*0} \to \Lambda X)} = \frac{47.5\%}{52.5\%}.$$

To save computing time, the branching ratio $BR(\Lambda \to p\pi^-)$ was set to 100%, neglecting decays of $\Lambda \to n\pi^0$. To compensate for the neglected decay mode, a correction factor of 0.639 is applied in the efficiency determination later on.

In sample 2, the semileptonic decays of the b baryon are modelled using the JETSET default matrix-element approach. This approach neglects polarisation and form-factor effects. The sample is referred to as the "*unpolarised sample*."

For the generation of sample 3, the JETSET program has been altered in order to incorporate polarisation and form-factor effects. The predicted polarisation of the b quarks has been assumed to be transferred through the process of fragmentation into the b baryon [32, 53]. In addition, the form factor described in chapter 2.3 was used for the generation of this "*polarised sample*."

All three samples have been processed with the full detector[1] simulation program GOPAL, as mentioned above, and the event reconstruction program ROPE.

Many of the selection criteria used are based on quantities measured in the xy-plane of the central detector. These quantities are calculated from the measured track curvature, κ, the azimuthal angle of the track tangent at the point of closest approach, ϕ_0, and the impact parameter, d_0. The accuracy of the detector simulation for these quantities has been studied elsewhere [54].

---

[1] The detector configuration of 1992 has been used for the simulation of sample 2 and 3. The first half of sample 1 has been simulated using the configuration of 1992. The rest has been processed with the 1993 detector configuration. The 1993 setting differs from the 1992 setting by the inclusion of the new silicon microvertex detector (and the silicon tungsten detector). These differences are not important for this analysis since no vertex-finding is done inside the sensitive range of the silicon microvertex detector.

It has been found that the resolution of κ is well reproduced by GOPAL while the resolutions for ϕ_0 and d_0 are not. The simulations are improved by additionally smearing the resolutions of the track parameters d_0 and ϕ_0 by factors of $f_{d_0} = 1.4$ and $f_{\phi_0} = 1.3$ [54], before passing the simulated events into the selection program. This is done by multiplying the difference between the reconstructed track parameters and the original values obtained from the four-vector at the generator level with the correction factors f_{d_0} and f_{ϕ_0}.

5.2 Uncertainties in the Detector Simulation

5.2.1 Uncertainties in the Lepton Efficiencies

The standard lepton-finding algorithms [47, 48] of the OPAL collaboration, introduced in the previous chapter, are used for the lepton selection. The algorithms include routines to correct the resolutions obtained from the Monte Carlo simulations [47, 48]. The resulting efficiency of the standard lepton selection can be determined from the Monte Carlo with systematic uncertainties at the 2%–3% level [14].

The electron identification efficiency is modelled by the corrected Monte Carlo simulation to within a systematic uncertainty of $\Delta\varepsilon_e/\varepsilon_e = \pm 2.5\%$ [14]. The value has been obtained by using several subsamples of tracks in different angular, momentum and transverse momentum ranges as outlined in the reference. The Monte Carlo samples used in this thesis were generated with the 1992 detector setup. Some additional corrections to the electron efficiency determination from this Monte Carlo sample need to be applied for the 1993 and 1994 data in order to account for defective z-chamber panels and jet chamber wire readouts to which the electron selection is sensitive [55]. The correction factors are known within a systematic uncertainty of ±2% [55] and are given in table 5.1 for the different years of data-taking. By averaging the correction factors with respect to the number of selected multihadronic events an overall

Year	1990	1991	1992	1993	1994	1990–1994
Multihadrons $\times 10^3$	133	340	754	704	1678	3610
Shift	–	–	–	−1.8%	−4.4%	−2.4%
Uncertainty	2.5%	2.5%	2.5%	3.2%	3.2%	3.0%

Table 5.1: Time Dependent Correction to Electron Efficiency
Listed are the number of selected multihadronic events, the shifts applied to the electron efficiency as determined by the Monte Carlo and the systematic uncertainty of the electron identification for the different years of data-taking. The last column lists the averaged values used for the analysis.

---

correction of $\delta\varepsilon_e/\varepsilon_e = (\varepsilon_e^{\mathrm{Data}} - \varepsilon_e^{\mathrm{MC}})/\varepsilon_e^{\mathrm{MC}} = -2.4\%$ and a total systematic uncertainty of the electron efficiency determination of $\Delta\varepsilon_e/\varepsilon_e = \pm 3.0\%$ are obtained.

As a cross-check, figure 5.1 shows the rate of selected electron candidates in multihadronic events, r_e, versus different years of data-taking after applying the correction. The electron candidates are selected using the standard electron identification and the electron momentum selection criteria described in the previous chapter. The error bars in the figure represent the statistical error only. The χ^2/DoF value, determined from the spread of the data points, is an estimate of the statistical and systematic fluctuations between the data points. The statistical fluctuations are assumed to result in $\chi^2_{\mathrm{stat}}/DoF = 1$. Using this assumption, the systematic fluctuations between the different years can be determined by

$$\Delta r_e/r_e = \sqrt{\chi^2/DoF - 1} \cdot \Delta a/a = 0.49\%, \tag{5.3}$$

where a is the weighted average. They are small compared to the assigned systematic uncertainty. The slightly higher rate in the 1994 data is caused by a higher background level [55]. The actual size of the background level is not crucial for the analysis (see chapter 6).

The muon identification efficiency is modelled by the corrected Monte Carlo simulation to within a systematic uncertainty of $\Delta\varepsilon_\mu/\varepsilon_\mu = \pm 1.7\%$ [14, 48]. The value has been obtained by comparing the effects of each selection criterion on different event samples such as $Z^0 \to \mu^+\mu^-$, $e^+e^- \to e^+e^-\mu^+\mu^-$ and

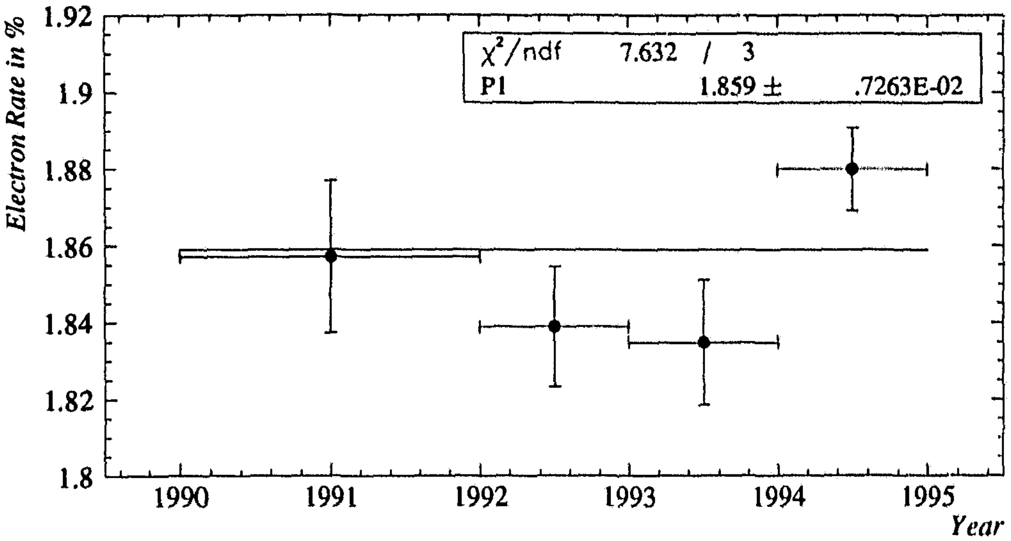

Figure 5.1: Electron Rate

The number of selected electrons normalised to the number of multihadronic events is plotted versus different years of data-taking after applying the efficiency correction. The errors drawn are statistical only and do not include the systematic uncertainty of the method and the correction factor. The last point is slightly above average due to higher background rates in the 1994 data.

$Z^0 \rightarrow$ hadrons, with the effect on the corresponding Monte Carlo simulations. Small corrections, at the 1% level, to the efficiency in different geometrical regions of the detector are not important for this analysis, and thus have been neglected. In addition, tracking errors affecting the d_0 selection criterion and the matching efficiency have been found to be described in the Monte Carlo simulation within a systematic uncertainty of 1.6% which leads to an overall relative systematic uncertainty of $\Delta\varepsilon_\mu/\varepsilon_\mu = \pm 2.3\%$ for the muon efficiency obtained from Monte Carlo simulations. The muon identification is less sensitive to the previously mentioned problems with the z-chamber panels and the jet-chamber wire readouts and, therefore, no additional corrections need to be applied for the 1993 and 1994 data [56]. As a cross-check, the muon rate, r_μ, versus different years of data-taking is plotted in figure 5.2. The systematic

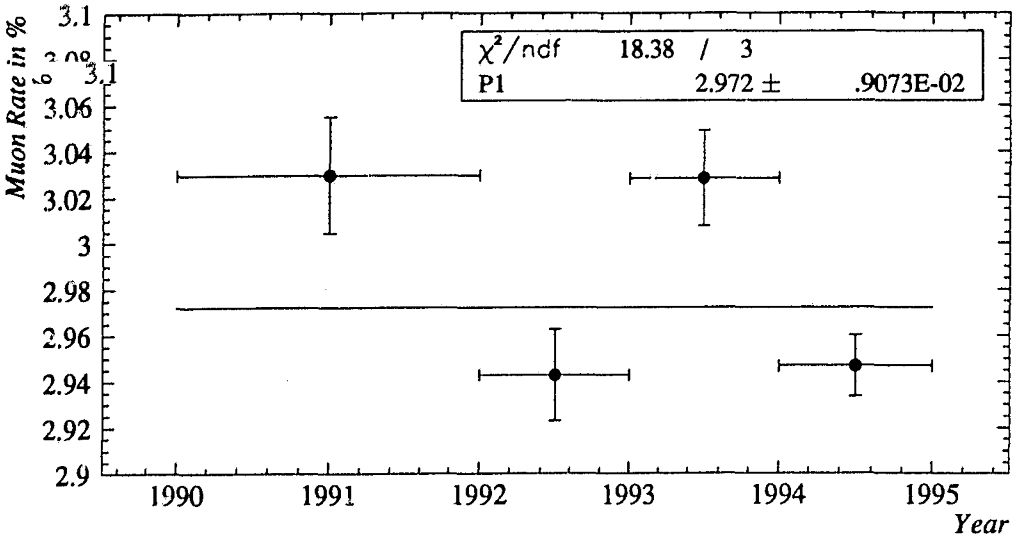

Figure 5.2: Muon Rate

The number of selected muon candidates per multihadronic events is plotted versus different years of data-taking. The errors drawn are statistical only. No efficiency corrections have been applied. The spread in the data points is used to check the systematic error calculation.

---

fluctuations between the different years are determined to be

$$\Delta r_\mu / r_\mu = \sqrt{\chi^2/DoF - 1} \cdot \Delta a/a = 0.69\%, \tag{5.4}$$

where a is the weighted average. They are found to be well contained in the assigned systematic uncertainty.

5.2.2 Uncertainty in the Λ Efficiency

The efficiency of the Λ selection depends strongly upon the Λ momentum and is therefore studied for different momentum intervals. The efficiency of the Λ preselection obtained from the general, the polarised and the unpolarised Monte Carlo samples is given in figure 5.3. For the general multihadronic sample all Λ particles are used for the calculation of the efficiency while for the unpolarised and the polarised samples only Λ particles from the decay chain

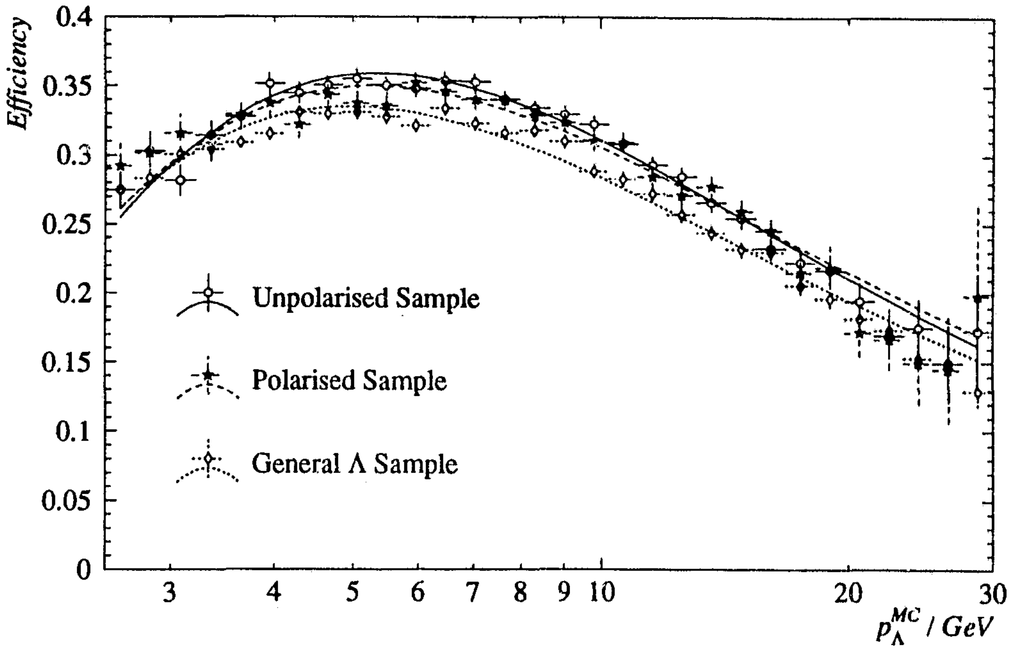

Figure 5.3: Preselection Λ-Finding Efficiency for the Three Different Samples *The values are fitted with an empirical function of the form:* $f(x) = \xi_1 x^{\xi_2} e^{-\xi_3 x}$ *with* $x = \ln p_\Lambda^{\mathrm{MC}}$ *and* $\xi_1, \ldots, \xi_3$ *are the free parameters of the fit.*

---

of a semileptonically decaying b baryon are used. For the calculation of the efficiencies of the polarised and unpolarised Monte Carlo samples, a correction factor of 0.639 has been applied in order to account for the neglected $\Lambda \to n\pi^0$ decays. The variation of the Λ efficiency between samples is due to differences in the isolation of the Λ and differences in the numbers of Λ particles that are produced through the decay of other long-lived baryons, for example $\Xi^0 \to \Lambda X$ with $c\tau_{\Xi^0} = 8.71$ cm, compared to $c\tau_\Lambda = 7.89$ cm for the Λ, where τ is the mean lifetime of the particle.

All selection criteria used in the Λ preselection, except the restriction on the primary momentum and the primary invariant mass selection criterion, are based on quantities measured in the xy-plane of the central detector. The sensitivity of the preselection to uncertainties in the ϕ_0 and d_0 resolution is studied by varying the smearing factors, f_{d_0} and f_{ϕ_0} described in section 5.1, between $1.0 \leq f_{d_0} \leq 1.8$ and $1.0 \leq f_{\phi_0} \leq 1.6$. Varying the smearing factors in this manner yields changes in the efficiency on the order of $\Delta\varepsilon_\Lambda/\varepsilon_\Lambda = \pm 3.0\%$, independent of the Λ momentum. This value is taken as the systematic uncertainty of the efficiency determined by Monte Carlo simulations due to tracking uncertainties.

The main Λ selection requires good z-information for the tracks, demands consistency of the measured $\mathrm{d}E/\mathrm{d}x$ of the proton candidate with the proton hypothesis, and includes the K^0-rejection criterion and the Λ mass window. The systematic uncertainty introduced by determining the efficiency of these selection criteria from the Monte Carlo simulation is studied by comparing the effects of the main Λ selection on the data with the effects on the general Monte Carlo sample. The Λ candidates of the general multihadronic sample and the Λ candidates found in the data are compared, after applying the preselection, in 31 momentum subsamples. The momentum intervals are chosen as shown in figure 5.3. The last momentum interval contains all Λ candidates with momenta above 30 GeV/c. For each momentum interval, the Λ candidates are split again into two subsamples labelled "*survivors*" or "*rejects*", depending on whether or not they fulfil the z-information and the $\mathrm{d}E/\mathrm{d}x$ requirement and have not been vetoed by the K^0-rejection criterion.

The numbers of Λ particles in the survivor samples and the reject samples, for the data as well as for the Monte Carlo simulation, are estimated by fitting the function described in the previous chapter to the proton-pion invariant mass distribution. The Λ-finding efficiency for the main Λ selection for each momentum interval, p_i, is in the ideal case given by

$$\varepsilon_i^{\mathrm{main}\,\Lambda}(p_i) = \frac{S_i}{S_i + s_i + R_i + r_i}, \tag{5.5}$$

where the letters stand for the estimated number of Λ particles in a given momentum interval with

$S_i \equiv$ # inside the signal window of the survivor sample,
$R_i \equiv$ # inside the signal window of the reject sample,
$s_i \equiv$ # outside the signal window of the survivor sample,
$r_i \equiv$ # outside the signal window of the reject sample,

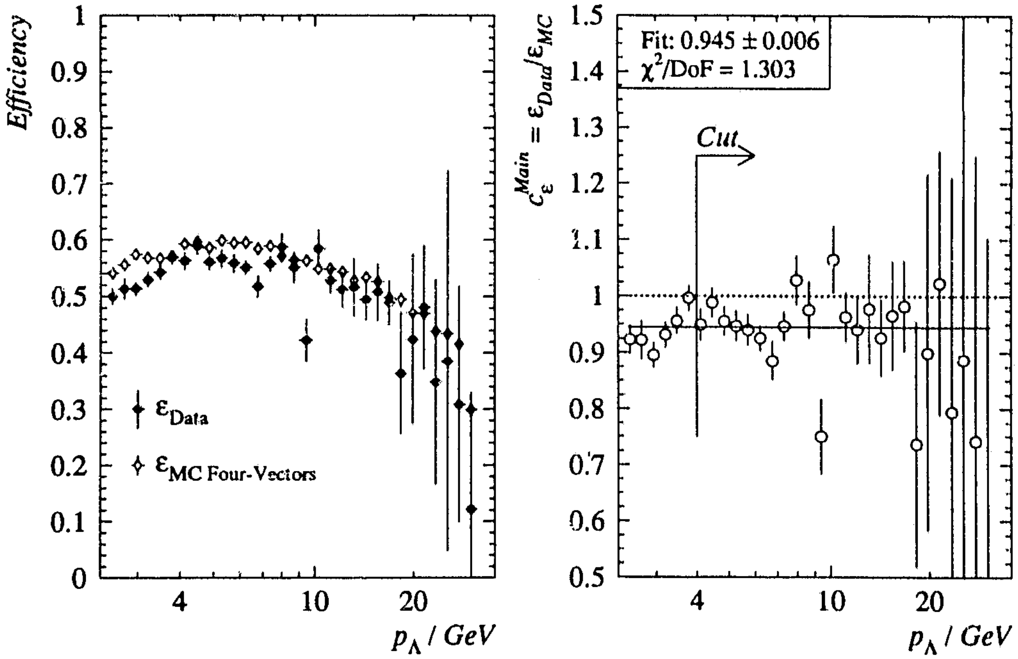

Figure 5.4: Efficiency of the Main Λ Selection

The efficiency calculated from the data after corrections is shown in the first figure by the black dots. The diamonds indicate the efficiency obtained from the Monte Carlo information. The second figure shows the relation between the data and the Monte Carlo. The efficiency in the data is observed to be lower than that in the Monte Carlo simulation.

---

with i denoting the interval in either data or Monte Carlo simulation. The numbers S_i and R_i are obtained by subtracting the integrated background from the counted number of events in the signal window. The numbers s_i and r_i are obtained from integrating the signal function numerically outside the mass window.

Since the functions used in the fit do not describe the signal and the background perfectly, correction factors need to be applied. The correction factors $c_1^i, \dots, c_3^i$ are chosen so that equation 5.5 takes the form

$$\varepsilon_i^{\mathrm{main}\,\Lambda}(p_i) = \frac{c_1^i S_i}{c_2^i(S_i + s_i) + c_3^i(R_i + r_i)}. \tag{5.6}$$

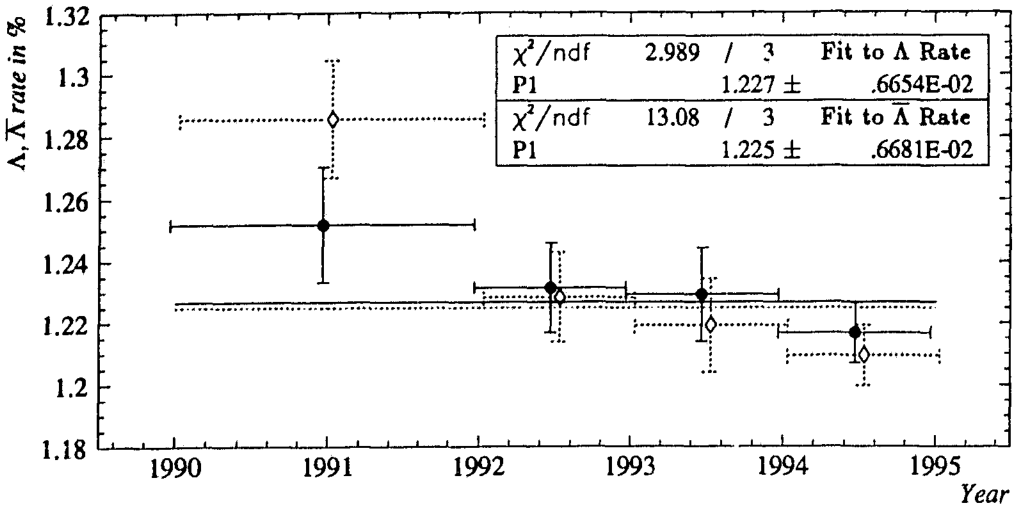

Figure 5.5: Λ and $\bar{\Lambda}$ Rates

Depicted are the rates of selected Λ candidates (solid lines) and $\bar{\Lambda}$ candidates (dotted lines) per multihadronic events, versus different years of data-taking. The errors drawn are statistical only. No efficiency corrections have been applied. Small systematic variations at the 1% level are seen for the $\bar{\Lambda}$ rates while the Λ rates fluctuate within their statistical errors. The slightly lower 1994 rate is due to the loss of z-chamber panels as described in the text.

The values of the correction factors are determined from the Monte Carlo sample for each momentum interval separately. Figure 5.4 shows the efficiencies for the main Λ selection obtained from the data using equation (5.6) and the correction factors obtained from the Monte Carlo sample. For comparison, the efficiency calculated from the true number of Λ in the Monte Carlo sample is also given. The efficiency is found to be $(5.5 \pm 0.6)\%$ lower in the data and consequently a correction of $\delta\varepsilon_\Lambda/\varepsilon_\Lambda = (-5.5 \pm 0.6)\%$ is applied to the efficiency as determined by the Monte Carlo simulation. Most of the difference can be attributed to the setting of the mass window. The proton-pion invariant mass peak is found to be wider in the data than in the Monte Carlo sample. By comparing the track parameters found in the data with those of the Monte Carlo simulation it has been found that the differences seen in the width are caused by an overly optimistic p_z resolution in the Monte Carlo simulation and to the defective z-chamber panels for during the 1993 and 1994 data-taking as mentioned in section 5.2.1.

The Λ and $\overline{\Lambda}$ signals per number of multihadronic events have been estimated for different years of data taken in order to cross check their time stability. The resulting rates are plotted in figure 5.5. Combining the Λ and $\overline{\Lambda}$ signals, the systematic variations are found to be less than 1%. In hadronic interactions of highly energetic particles with the detector materials, a low energy Λ is more likely to be produced than a $\overline{\Lambda}$. This causes the slightly higher average Λ rate in the data. In the time period from 1990 to 1991 more $\overline{\Lambda}$ particles are found which most likely represents a statistical fluctuation. The slightly lower 1994 rate is caused by the above mentioned loss of z-chamber panels to which the selection is sensitive. The effect is accounted for by the correction to the main Λ selection discussed above. Overall, the effects of time variations in the data quality are found to be negligible.

5.2.3 Summary

As mentioned in section 5.2.1, other studies have found that the Monte Carlo package simulates the efficiency of the standard electron finding algorithm to within a systematic uncertainty of $\Delta\varepsilon_e/\varepsilon_e = \pm 3.0\%$ after an additional shift of $\delta\varepsilon_e/\varepsilon_e = -2.4\%$ has been applied. The efficiency of the standard muon finding algorithm is found to be simulated correctly by the Monte Carlo simulations to within a systematic uncertainty of $\Delta\varepsilon_\mu/\varepsilon_\mu = \pm 2.3\%$. For the Λ selection, a relative systematic uncertainty of $\Delta\varepsilon_\Lambda/\varepsilon_\Lambda = \pm 3.0\%$ is assigned in order to account for tracking uncertainties affecting the Λ preselection. In addition, a correction of $\delta\varepsilon_\Lambda/\varepsilon_\Lambda = (-5.5 \pm 0.6)\%$ is applied to the Λ efficiency in order to account for the differences in the modelling of the effects of the main Λ selection in the Monte Carlo simulation.

The uncertainties are assumed to be uncorrelated since they correspond to intrinsically different selections and will be added in quadrature. The combined Λ-lepton selection criteria are purely kinematic in nature and are well-simulated by the Monte Carlo.

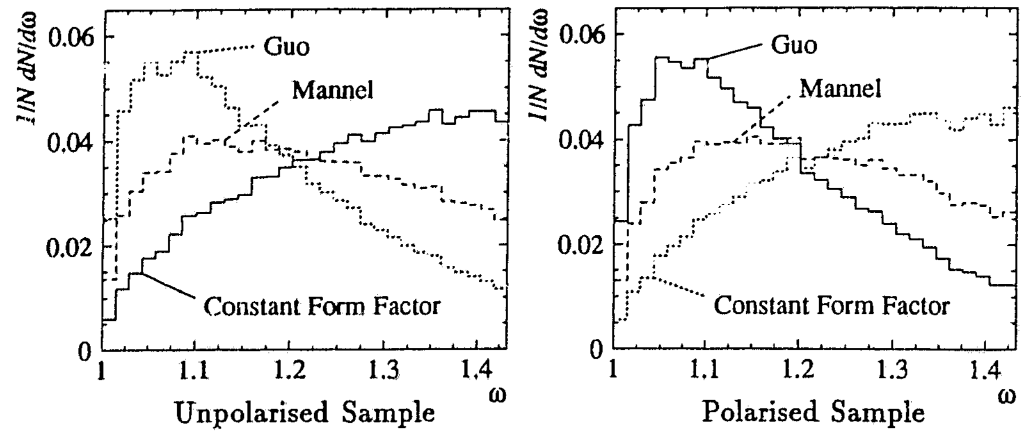

Figure 5.6: Differential Decay Rates for Various Form Factors
The differential decay rates obtained with form factors used for the generation of the unpolarised and the polarised Monte Carlo samples are indicated by the solid lines. For the systematic analysis, the form factor effects are studied by re-weighting the Monte Carlo samples. The resulting distributions are given as dashed and dotted lines. The distribution obtained from the unpolarised sample, which is denoted as "Guo", resembles the function shown in figure 2.11 Ⓑ.

5.3 Model Uncertainties

The efficiency of the entire selection is studied by using the unpolarised and the polarised Monte Carlo samples. Uncertainties in Λ_b^0 decay modelling (form factor, see section 2.3) and the unknown fragmentation process are taken into account by re-weighting the samples. Special Monte Carlo samples which have been processed through GOPAL in smear-mode are used to determine other systematic uncertainties and corrections to the efficiencies such as the unknown b-baryon masses, variations in the centre-of-mass energy, uncertainties in the Λ_c branching ratios and alternative Λ_b^0 decays modes into Σ_c and Σ_c^*.

The dependence of the efficiency on the choice of the form factor used to simulate the Λ_b^0 decays is studied by re-weighting the Monte Carlo samples. The form factor depends upon the velocity transfer variable ω which is defined in (2.35). In the JETSET default, a constant form factor is assumed. The JETSET default was used for the generation of the unpolarised Monte Carlo

Efficiency				
	Form Factor			stat.
Sample	Constant	Mannel	Guo	Error
Unpolarised	**.0551**	.0539	.0527	.0008 ↔ .0010
Polarised	.0540	.0540	**.0536**	.0012 ↔ .0009

Table 5.2: Efficiency Dependence on the Form Factor Used
The values (bold faced) for unpolarised, constant form factor and polarised, F^{Guo} *are obtained directly from the Monte Carlo samples, while all other values are determined from the re-weighted samples. The statistical error varies in the range given depending upon the degree of re-weighting.*

sample. Alternatively, an empirical form factor derived from b-meson decays by Mannel and Schuler [32] is considered. The form factor is parameterised by

$$F^{\mathrm{Mannel}}(\omega) = \frac{\omega_0^2}{\omega_0^2 - 2 + 2\,\omega} \tag{5.7}$$

with $\omega_0 = 0.89$. In addition, the form factor introduced in chapter 2.3 is considered. This form factor is based on calculations by Guo and Kroll [6] using HQET. The resulting rather complex set of six form factors is approximated with the parametrisation given in (2.36) and has been used for the generation of the polarised Monte Carlo sample.

Figure 5.6 shows the resulting decay rates in terms of ω for the unpolarised Monte Carlo sample and the distributions resulting from re-weighting the sample to F^{Mannel} and F^{Guo}. The efficiencies obtained are given in table 5.2. The efficiency found using the empirical form factor (Mannel) lies well between the other two. For the determination of the central value of the efficiency the HQET form factor, F^{Guo}, has been used. The maximum difference in efficiency between it and the JETSET default (constant form factor) is assigned as the systematic uncertainty $\Delta\varepsilon_{\Lambda\ell}/\varepsilon_{\Lambda\ell} = \pm 4.5\%$ due to the unknown Λ_b decay modelling.

Little effect on the efficiency was seen by varying the polarisation of the Λ_b between the two extreme cases of 0% polarisation, corresponding to a situation where all the b-quark polarisation predicted by the Standard Model is lost in

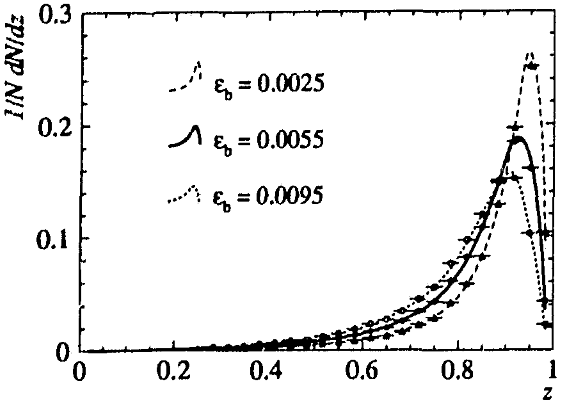

Figure 5.7: Fragmentation *Shown are the fragmentation functions corresponding to three alternative values of ϵ_b. The dashed and dotted curves are obtained by re-weighting the Monte Carlo sample.*

the fragmentation process, and −93% polarisation which assumes the b-quark polarisation is fully transferred through the process of fragmentation to the Λ_b. The efficiency obtained with −47% polarisation (half of the polarisation of the b quarks) is used for the central value of the efficiency and the maximal deviation of $\Delta\varepsilon_{\Lambda\ell}/\varepsilon_{\Lambda\ell} = \pm 0.9\%$ between the corresponding 0% and −93% polarised samples is assigned as the systematic uncertainty due to unknown b-baryon polarisation[2].

The Monte Carlo samples have been generated with the use of the Peterson fragmentation function given in (2.28). The effect of uncertainties in the fragmentation process on the efficiency determination is studied by re-weighting the Monte Carlo samples to different ϵ_b parameters of the fragmentation function. The selection efficiency obtained with the value of $\epsilon_b = 0.0055$, namely the value used for the generation of the Monte Carlo samples, is used. This value has been chosen according to a study of b-quark fragmentation in Z^0 decays [58]. The values, $\epsilon_b = 0.0025$ and $\epsilon_b = 0.0095$, have been chosen as conservative limits for the study of the systematic errors. The z-distributions for the weighted and the unweighted samples are shown in figure 5.7. The maximal difference in efficiency of $\Delta\varepsilon_{\Lambda\ell}/\varepsilon_{\Lambda\ell} = \pm 3.0\%$ due to uncertainties in the fragmentation process is assigned as the systematic uncertainty.

---

[2] The ALEPH collaboration has presented a preliminary measurement of the Λ_b polarisation, $\mathcal{P}_{\Lambda_b} = -0.30^{+32}_{-27} \pm 0.04$ [57]. The value has not been used for this analysis, since the measurement is preliminary and the result is not conclusive.

Of the data collected, 91.1% of the events were taken at centre-of-mass energies of (91.2 ± 0.2) GeV. Another 3.6% of the events were produced at lower energies centred around 89.4 GeV. The remaining 5.3% were taken at an average energy of 93.0 GeV. The influence of the variation of the centre-of-mass energy on the efficiency is studied using Monte Carlo samples which were processed with GOPAL in smear-mode. The systematic uncertainty in the efficiency due to changes in the centre-of-mass energy has been found to be $\Delta\varepsilon_{\Lambda\ell}/\varepsilon_{\Lambda\ell} = \pm 0.1\%$.

The masses of the b baryons have not yet been measured. In the case of the Λ_b^0, theoretical predictions range from $m_{\Lambda_b^0} = 5547$ to 5660 MeV/c^2 [59]. In the generation of the Monte Carlo samples, the JETSET default of $m_{\Lambda_b^0} = 5620$ MeV/c^2 was used. The effect of different choices of the b-baryon masses on the selection efficiency is studied using special Monte Carlo samples that have been processed with GOPAL in smear-mode. The default masses of all b baryons have been varied by ± 100 MeV/c^2 resulting in changes in the selection efficiency of $(1.8 \pm 1.1)\%$, where the error comes from Monte Carlo statistics. A systematic uncertainty of $\Delta\varepsilon_{\Lambda\ell}/\varepsilon_{\Lambda\ell} = \pm 1.8\%$ is assigned to the selection efficiency due to the unknown b-baryon masses.

Another source of error is the improper simulation of the Λ_b and Λ_c decays in the Monte Carlo simulations. The JETSET default semileptonic Λ_b^0 decays are always of the form $\Lambda_b^0 \rightarrow \Lambda_c^+ \ell^- \bar{\nu}$. In principle, decays of the form $\Lambda_b \rightarrow Y_c \ell \bar{\nu}$, where Y_c is an excited c-baryon state, are also possible. Furthermore, decays involving additional pions could occur but they are expected to have a low probability [60]. The most likely alternative decay of the Λ_b^0 is into a Σ_c^+ or Σ_c^{*+}. From simple spin arguments one expects a production ratio of $\Sigma_c^+ : \Sigma_c^{*+} = 2 : 4$. The Σ_c^{*+} decays electromagnetically into the Σ_c^+. The Σ_c^+ itself decays into $\Lambda_c^+ \pi^0$ with a branching ratio of 100%. The decays $\Lambda_b^0 \rightarrow \Lambda_c^+ X$ and $\Lambda_b^0 \rightarrow \Sigma_c^+/\Sigma_c^{*+} X$ are assumed to occur equally often, which is motivated by the nearly equal decay rates of $\Lambda_c^+ \rightarrow \Lambda \pi^+$ and $\Lambda_c^+ \rightarrow \Sigma^0 \pi^+$.

Three sets of Monte Carlo simulated events have been processed with GOPAL in the smear-mode to study the effects of alternative decay modes on the efficiency determination. Each set contains 50,000 JETSET events, where the three studied decay modes, $\Lambda_b^0 \to \Lambda_c^+ \ell^- \overline{\nu}$, $\Lambda_b^0 \to \Sigma_c^+ \ell^- \overline{\nu}$ and $\Lambda_b^0 \to \Sigma_c^{*+} \ell^- \overline{\nu}$, have been simulated using the EURODEC program with appropriately modified decay tables. A decrease in the overall $\Lambda_b \to \Lambda \ell^- \overline{\nu} X$ efficiency of $(2.6 \pm 0.8)\%$, where the error is due to Monte Carlo statistics, is found using the above ratios. The selection efficiency is corrected by $\delta\varepsilon_{\Lambda\ell}/\varepsilon_{\Lambda\ell} = (-1.3 \pm 1.3)\%$ to encompass the full range of possible decay rates.

In the Monte Carlo samples, 12% of all semileptonic b-baryon decays are Ξ_b decays. The first measurements of the Ξ_b^- production rate [34] are in agreement with this number. The selection efficiency for Λ-lepton pairs produced in the decay chain of a Ξ_b is expected to be smaller than the selection efficiency of those pairs produced in the decay chain of a Λ_b^0 since roughly 50% of the Ξ_b will decay via the chain $\Xi_b \to \Xi_c \to \Xi \to \Lambda$. The lifetime of Ξ baryons is comparable to that of the Λ. Thus, many of them decay into a Λ inside the detector, leading to an overall smaller selection efficiency for the Λ. The effect of the unknown Ξ_b content on the selection efficiency is studied by allowing the Ξ_b rate in the Monte Carlo to vary between 0% and 24%. This changes the efficiency by $\Delta\varepsilon_{\Lambda\ell}/\varepsilon_{\Lambda\ell} = \pm 2.4\%$ compared to the value obtained with the default 12% Ξ_b content. The ±2.4% variation is assigned as the systematic error due to the unknown Ξ_b content. A Ξ_b content of 12% is used for the central value of the efficiency.

The branching ratios of the decay modes $\Lambda_c^+ \to \Lambda X$ are not well known. Different decay chains could lead to different momentum distributions for the resulting Λ and therefore to different selection efficiencies. In order to check the effects of different decay models, Λ_c^+ decays simulated with EURODEC using the updated decay tables mentioned in 5.1 are compared to those simulated with the JETSET default. The resulting observed difference in efficiency of $(1.1 \pm 1.9)\%$, where the error reflects the Monte Carlo statistics, is found to be small. Conservatively, a systematic uncertainty of $\Delta\varepsilon_{\Lambda\ell}/\varepsilon_{\Lambda\ell} = \pm 1.9\%$ is assigned due to uncertainties in the Λ_c^+ decay model.

Source	Systematic Shift $(\varepsilon^{\mathrm{Data}}_{\Lambda\ell} - \varepsilon^{\mathrm{MC}}_{\Lambda\ell})/\varepsilon^{\mathrm{MC}}_{\Lambda\ell}$		Systematic Error $\Delta\varepsilon_{\Lambda\ell}/\varepsilon_{\Lambda\ell}$	
	Λe	$\Lambda\mu$	Λe	$\Lambda\mu$
Monte Carlo Statistics	–	–	2.0%	1.6%
Lepton Identification	−2.4%	–	3.0%	2.3%
Total	−2.4%	–	3.6%	2.8%

Table 5.3: Uncorrelated Uncertainties in the Efficiency Determination
Given are the corrections to the Monte Carlo prediction and systematic errors of the efficiency determination which are assumed to be uncorrelated for the electron and muon samples. All numbers are relative to the efficiency obtained from the Monte Carlo simulation.

Source	Systematic Shift $(\varepsilon^{\mathrm{Data}}_{\Lambda\ell} - \varepsilon^{\mathrm{MC}}_{\Lambda\ell})/\varepsilon^{\mathrm{MC}}_{\Lambda\ell}$	Systematic Error $\Delta\varepsilon_{\Lambda\ell}/\varepsilon_{\Lambda\ell}$
Λ Selection:		
Track Modelling, xy-Plane	–	3.0%
Λ Mass Resolution	−5.5%	0.6%
Combined Selection:		
Λ_b Decay Form Factor	–	4.5%
Λ_b Polarisation	–	0.9%
b Fragmentation	–	3.0%
Centre-of-Mass Energy	–	0.1%
Λ_b Mass	–	1.8%
Λ_b Decay Modelling	−1.3%	1.3%
Ξ_b Uncertainty	–	2.4%
Λ_c Decay Modelling	–	1.9%
Total	−6.8%	7.4%

Table 5.4: Correlated Uncertainties in the Efficiency Determination
Given are the corrections to the Monte Carlo prediction and systematic errors which are identical for the electron and muon efficiency determinations. All numbers are relative to the efficiency obtained from the Monte Carlo simulation.

5.4 Summary

The efficiency of the selection process is determined from the polarised and the unpolarised Monte Carlo samples. The uncertainties of the method have been studied and the results are listed in table 5.3 and 5.4. An overall shift between the efficiency obtained from the Monte Carlo samples and the data of $\delta\varepsilon_{\Lambda e} = -9.2\%$ for the Λe sample and $\delta\varepsilon_{\Lambda\mu} = -6.8\%$ for the $\Lambda\mu$ sample has been determined and is applied in the efficiency computation,

$$\varepsilon^{\mathrm{Data}} = \varepsilon^{\mathrm{MC}}(1 + \delta\varepsilon). \tag{5.8}$$

In summary, the efficiencies obtained for the Λ-electron and Λ-muon samples are:

$$\begin{aligned} \varepsilon_{\Lambda e} &= 0.0378 \pm 0.0014 \pm 0.0028, \\ \varepsilon_{\Lambda\mu} &= 0.0602 \pm 0.0017 \pm 0.0044, \end{aligned} \tag{5.9}$$

where the first error represents the uncertainty due to limited Monte Carlo statistics and the lepton identification specific uncertainty. The second error represents all the other systematic uncertainties in the efficiency determination. The first errors are assumed to be uncorrelated to each other while the second errors are fully correlated.

Chapter 6

Background Study

Several processes are known to have signatures similar to those of the signal and consequently need to be considered as backgrounds. Some of these backgrounds contribute equally to the right-sign and wrong-sign samples and are easily accounted for by subtracting the number of events in the wrong-sign sample from the number of events in the right-sign sample (see fig. 4.4). Other backgrounds that contribute differently to the right-sign and the wrong-sign samples are studied in more detail in this chapter. A correction to the background subtraction method is found and will be applied to the calculation of the result in the next chapter.

6.1 Fragmentation Background

Fragmentation Λ particles combined with leptons from semileptonic c- or b-hadron decays are found to be one of the biggest sources of background. This fragmentation background can be subdivided into four categories dependent on the origin of the selected lepton:

- A fragmentation Λ combined with a lepton from a b-baryon decay.
- A fragmentation Λ combined with a lepton from a b-meson decay.
- A fragmentation Λ combined with a lepton from a c-baryon decay.
- A fragmentation Λ combined with a lepton from a c-meson decay.

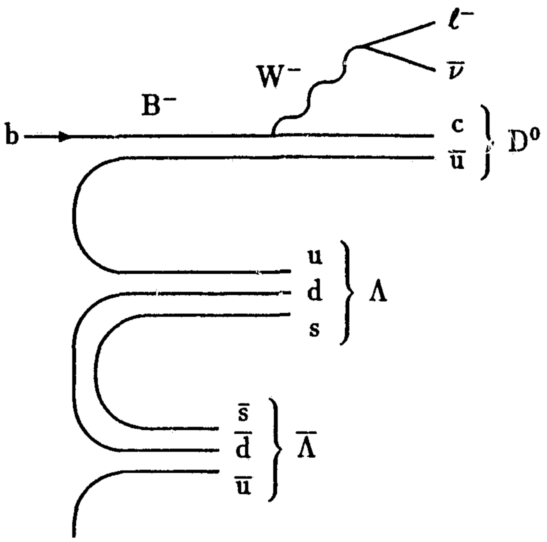

Figure 6.1: B Background
A B$^-$ is created in the fragmentation process and decays semileptonically into a negatively charged lepton. In the example, the B$^-$ is accompanied by a Λ-$\bar{\Lambda}$ pair. In a string-like fragmentation model, the baryon is always closer to the b *meson than the antibaryon and, therefore, more likely to be of higher momentum. This leads to a slightly higher selection probability of $\Lambda\ell^-$ combinations. Consequently, the background contributes more to the right-sign sample.*

In the framework of the fragmentation model introduced in section 2.2.2, it is expected that these backgrounds contribute differently to the right-sign and to the wrong-sign samples. The effect is most apparent in the case where a fragmentation Λ and a lepton from a semileptonic b-baryon decay form a candidate. Most likely the fragmentation Λ is the baryonic partner of the b baryon that decayed semileptonically since in general it is produced closest to the b baryon in the fragmentation process. In a string-like fragmentation model[1], the fragmentation Λ is strongly kinematically and geometrically correlated to the b baryon leading to a statistically significant selection probability of this process. Since the baryonic partner of the semileptonically decaying b baryon is an antibaryon, or vice versa, this process would contribute only to the wrong-sign sample.

Another, less obvious example which contributes differently to the right-sign and wrong-sign backgrounds is shown in figure 6.1. In the example the b meson, in this case a B$^-$, decays semileptonically into a ℓ^-, a $\bar{\nu}$ and a D^0. Furthermore, a baryon pair is formed during the fragmentation process (a Λ-$\bar{\Lambda}$ pair

---

[1] This is a side effect of the so-called *string effect* which is found to be well simulated by JETSET [26, 61].

JETSET Baryon Production Parameters					
Regulation of	Relation	Name	Popcorn Probability		
			0%	50%	95%
Strange Diquarks	$\frac{P(\mathrm{us})/P(\mathrm{ud})}{P(\mathrm{s})/P(\mathrm{d})}$	PARJ(3)	0.26	0.30	0.32
Diquark Spin	$\frac{P((\mathrm{ud})_1)}{3P((\mathrm{ud})_0)}$	PARJ(4)	0.04	0.05	0.0025
Popcorn	$\frac{P(\mathrm{BM\bar{B}})}{2P(\mathrm{B\bar{B}})}$	PARJ(5)	0.	0.5	9.5

Table 6.1: JETSET Parameters Used for the Background Study
The parameters controlling the baryon production have been altered according to [26] in order to study the effect of the unknown popcorn parameter on the imbalance created by the backgrounds from fragmentation Λ particles that were associated with leptons from heavy quark decays. The JETSET default values correspond to 50% popcorn.

in fig. 6.1). In the string-like fragmentation model the baryon is closer to the b meson than the antibaryon. The b meson pulls along the baryon giving it, on average, a slightly higher momentum. Consequently, a fragmentation Λ produced alongside a b meson is more likely to pass the Λ momentum selection criterion than a fragmentation $\overline{\Lambda}$. This results in a slightly higher selection probability of the $\Lambda\ell^- / \overline{\Lambda}\ell^+$ combinations in comparison to $\overline{\Lambda}\ell^- / \Lambda\ell^+$ combinations and contributes therefore more to the right-sign sample.

In all of the above cases, the selection probability depends upon the degree of correlation between the baryon-antibaryon pair. In the popcorn model introduced in section 2.2.2, the strength of the correlation between the b baryon and its antibaryonic partner[2] depends on the number of mesons being produced between them in the fragmentation process. Inside the JETSET program the popcorn parameter regulates the likelihood of mesons being produced between baryon pairs and therefore the strength of correlations.

The dependence of the JETSET Monte Carlo prediction on the popcorn parameter is studied using three special Monte Carlo samples, each consist-

---

[2] **As stated in the introduction, charge conjugate processes are implied implicitly.**

ing of roughly 5 million $b\bar{b}$ and $c\bar{c}$ JETSET events. It was found in previous studies [26] of the baryon production rates that the popcorn parameter is correlated with other baryon production parameters inside JETSET. For the three Monte Carlo samples, the baryon production parameters, listed in table 2.1, have been chosen according to [26] with the correlations being taken into account. The first Monte Carlo sample has been generated with a parameter set corresponding to 0% popcorn probability, the second with the default value of 50% and the third with a value of 95%. The events generated have been processed with GOPAL in the smear-mode and are passed through the event selection.

The particle identification efficiencies in the smeared Monte Carlo samples differ from the efficiencies in samples that have been processed with the full GOPAL. However, the kinematic properties are well described by the smear Monte Carlo. In order to be able to use the background estimates obtained from the smear Monte Carlo, the estimates must be expressed in a form that is independent of the particle identification efficiency. This is achieved by normalising the estimates to the number of selected b baryons in the specific sample. The use of smear Monte Carlo for the study of the fragmentation background is justified because the differences in the event signatures are of a purely kinematic nature. Furthermore, the absolute background is not of interest, but only the rather small difference in the contributions to the wrong-sign and right-sign samples. The results of the study are summarised in table 6.2.

As described above, the background from fragmentation Λ particles combined with leptons from b-baryon decays, contributes mainly to the wrong-sign sample. Studying the smear Monte Carlo samples, a contribution to the right-sign sample of $(0.79\pm0.14)\%$ with respect to the number of identified b baryons is found. The number is obtained from the sample that has been generated with the default values in JETSET. In contrast, the contribution to the wrong-sign sample is found to be $(12.74 \pm 0.59)\%$. This background is the largest source of unequal contributions to the right-sign and the wrong-sign samples. As a cross-check of the accuracy of the Monte Carlo estimate, the data sample has been searched for double events. A *double events* is a pair of candidates

Background from Fragmentation Λ Particles in %				
ℓ Origin	Contributing to	0% Popcorn	50% Popcorn	95% Popcorn
b baryon	right-sign	0.9± 0.2	0.8± 0.1	0.6± 0.1
	wrong-sign	−14.3± 0.6	−12.7± 0.6	−10.5± 0.5
b meson	right-sign	18.2± 0.7	17.9± 0.7	18.8± 0.7
	wrong-sign	−17.0± 0.7	−15.4± 0.7	−15.2± 0.7
c baryon	right-sign	1.6± 0.2	1.3± 0.2	1.6± 0.2
	wrong-sign	−0.1± 0.1	−0.2± 0.1	−0.1± 0.0
c meson	right-sign	8.2± 0.5	7.0± 0.4	6.7± 0.4
	wrong-sign	−9.5± 0.5	−10.4± 0.5	−11.2± 0.6
Σ		−11.9± 1.4	−11.8± 1.3	−9.2± 1.3

Table 6.2: Fragmentation-Dependent Background

Listed are the estimates for the percentage of background events from a fragmentation Λ which is accompanied by a lepton from a heavy hadron decay. The values given correspond to the three settings of the baryon production parameters given in table 6.1. The values are each normalised to the number of identified b *baryons. The JETSET default corresponds to a 50% popcorn probability. Contributions to the right-sign sample are given as positive values, while the negative numbers are contributions to the wrong-sign sample. Background subtraction is therefore performed by adding the numbers. The negative numbers in the bottom line indicate that these backgrounds contribute in total more to the wrong-sign than to the right-sign sample.*

(in the data or in a Monte Carlo sample) with at least one common track candidate and therefore at least one candidate due to a background process. The data sample has been searched for pairs of candidates which have the same lepton but different Λ candidates. Five such events are found and as expected they all have one Λ and one $\overline{\Lambda}$ candidate. Monte Carlo simulations predict 6.4 ± 0.7 double events of this kind. About half of these events are expected to originate from a b baryon accompanied by a fragmentation Λ, while the rest result from other backgrounds. In the general multihadronic Monte Carlo sample, seven such double events are found, where 5.3 ± 0.6 were expected. Therefore, it is concluded that the Monte Carlo description agrees with the data within the statistics.

The background from fragmentation Λ particles combined with leptons from b-meson decays has been found to be the single most significant background with a contribution to the right-sign sample of $(17.85 \pm 0.71)\%$ with respect to the number of identified b baryons. The contribution to the wrong-sign sample, $(15.39 \pm 0.65)\%$, is slightly lower as expected. The magnitude is due to the large b-meson production rate in Z^0 decays. Furthermore, leptons from b-hadron decays are likely to be selected since they have the same hard momentum spectrum as leptons from b-baryon decays. The expected difference in the contributions to the right-sign and wrong-sign samples is found to be small. Varying the popcorn probability between 0% and 95% leads only to small changes.

The background from fragmentation Λ particles combined with leptons from c-baryon decays is highly suppressed by the Λ-lepton invariant mass selection criterion. Nevertheless, small contributions of $(1.34 \pm 0.18)\%$ to the right-sign and $(0.19 \pm 0.07)\%$ to the wrong-sign samples are found. The asymmetry is expected because the c quark in the c baryon will decay into a positively charged lepton and the fragmentation Λ is most likely the antibaryonic partner of the c baryon. The case where the Λ originates from the c baryon is discussed in the next section. The dependence of the contributions on the popcorn parameter is given in table 6.2.

The background from fragmentation Λ particles combined with leptons from c-meson decays, is more likely to contribute to the wrong-sign sample. The reason is similar to the above case where a fragmentation Λ is combined with the lepton from a semileptonic b-meson decay which has been found to contribute more to the right-sign sample. The difference is that the c quark decays into a positively charged lepton and therefore the wrong-sign sample is favoured. In the above mentioned Monte Carlo sample, a contribution of $(6.97 \pm 0.42)\%$ to the right-sign sample is found. The contribution to the wrong-sign sample is $(10.38 \pm 0.52)\%$, confirming the expectation that this background contributes more to the wrong-sign sample.

The results of the study of the backgrounds from fragmentation Λ particles combined with leptons from heavy hadron decays are given in table 6.2. In summary, a normalised imbalance of

$$\frac{n_r - n_w}{n_{\Lambda_b}} = (-11.8 \pm 1.3 \pm 2.6)\% \tag{6.1}$$

towards the wrong-sign sample is found, where n_r and n_w are the number of background events in the right-sign and wrong-sign samples, and n_{Λ_b} is the number of identified b baryons in the same sample. The first error accounts for the limited Monte Carlo statistics and the second error is the systematic uncertainty reflecting the 2.6% differences seen between the default 50% and the 95% popcorn probability.

6.2 Exclusive Decay Modes

In addition to the fragmentation Λ background, several exclusive decay channels, which contribute unequally to the right-sign and wrong-sign samples, must be considered. The contributions from these exclusive decay channels, which are described below, are small compared to the previously described fragmentation backgrounds.

The contributions to the wrong-sign sample caused by semileptonically decaying c baryons, $\Lambda_c \rightarrow \Lambda \ell^+ \nu$, is estimated using the Monte Carlo sample generated with default parameters. Most of the $\Lambda_c \rightarrow \Lambda \ell^+ \nu$ events are rejected by the Λ-lepton invariant mass selection criterion. A contribution of $(2.53 \pm 0.25)\%$ with respect to the number of selected b baryons is obtained. The systematic error on this number is rather small since most b baryons decay via a c baryon into a Λ and therefore decay modelling effects cancel out in the calculation of the ratio.

Semileptonic decays of b baryons into τ leptons which then decay leptonically are not considered as signal. The τ background populates only the right-sign sample. However, it is suppressed by the lepton momentum requirement. The contribution of $(1.84 \pm 0.21)\%$ with respect to the number of selected b baryons has been estimated with the smear-mode Monte Carlo sample. Semileptonic decays of b baryons into a final state including a τ differ from decays into a light lepton only by the available phase space. By normalising to the number of identified semileptonic b baryons in the Monte Carlo sample, systematic uncertainties due to the unknown QCD form factors cancel. The branching ratios of semileptonic τ decays are well measured and assumed to be simulated correctly in the Monte Carlo. Therefore, no systematic error is assigned to this number.

The same Monte Carlo sample has been used to find the contributions from $\Lambda_b \to \Lambda_c D_s^-$ and $\Lambda_b \to \Lambda_c D_s^{*-}$ decays, where the $D_s^{(*)-}$ subsequently decays semileptonically. This background contributes to the right-sign sample only. A contribution of (1.19 ± 0.17 ± 0.60)% is found. Since the branching ratio for the decay $\Lambda_b \to \Lambda_c D_s^-$ is unmeasured, a systematic uncertainty of 50% is assumed for the branching ratio used in the Monte Carlo calculation.

The process $\overline{B} \to Y_c \overline{N} \ell^- \overline{\nu}$, where Y_c is a c baryon and $\overline{N}$ is an antibaryon, is a potential background source that is not simulated by JETSET using the default parameters. Decays of this form have not yet been observed [62], but an upper limit has been set by the ARGUS collaboration [63] on the branching ratios of semileptonic b-meson decays into final states including a proton, $BR(\overline{B} \to pe^-\overline{\nu}X) < 0.16\%$ (90% *C.L.*). This branching ratio and the ansatz

$$\frac{BR(\overline{B} \to \Lambda \ell^- \overline{\nu} X)}{BR(\overline{B} \to pe^- \overline{\nu} X)} = \frac{BR(\overline{B} \to \Lambda X)}{BR(\overline{B} \to pX)} \tag{6.2}$$

is used to determine an upper limit on the contribution of the background to the right-sign sample. In the above equation ℓ represents either an electron or a muon from a semileptonic B decay, X is any set of hadrons and the proton may originate from any intermediate baryon, including Λ particles. The ansatz is based on the assumption that the QCD corrections involved in the terms in the denominator of each side of the equation are approximately equal to those in the numerator and therefore cancel out. The branching ratios $BR(\overline{B} \to \Lambda X) = (4.0 \pm 0.5)\%$ and $BR(\overline{B} \to pX) = (8.0 \pm 0.5)\%$ have been taken from [2] resulting in an upper limit of

$$BR^{\max}(\overline{B} \to \Lambda \ell^- \overline{\nu} X) \leq (0.08 \pm 0.01)\%. \tag{6.3}$$

The selection efficiency for this background is estimated with the JETSET

Monte Carlo program using altered EURODEC decay tables to generate the $\overline{\mathrm{B}} \rightarrow \Lambda \ell^- \overline{\nu} \mathrm{X}$ decays. In terms of the normalisation used above, an upper limit of 2.8% on the contribution of this background to the right-sign sample is found. A correction of $(1.40 \pm 1.40)\%$ is applied to encompass the entire possible range.

Another potential background arises from $\overline{\mathrm{B}} \rightarrow \Lambda \overline{\mathrm{p}} \mathrm{X}$ decays with the $\overline{\mathrm{p}}$ being misidentified as a lepton. The electron selection is largely based upon the $\mathrm{d}E/\mathrm{d}x$ measurements of the candidate track as described in section 4.3.1. The probability of misidentifying a proton as an electron is negligible since the $\mathrm{d}E/\mathrm{d}x$ measurement method easily discriminates electrons and protons in the momentum range above 3 GeV/c (see fig. 3.3). Furthermore, good agreement has been found by comparing the $\mathrm{d}E/\mathrm{d}x$ values of the electrons found in the data with those of the Monte Carlo samples. The chance of misidentifying a proton as a muon is higher because protons may cause "punch-through" in the hadronic calorimeter which would appear to be a muon signal in the muon chambers. Also, the relative ionisation loss of protons and muons is closer in magnitude. To avoid backgrounds from kaons and protons in the muon sample, the $\mathrm{d}E/\mathrm{d}x$ rejection criterion described in section 4.3.2 has been applied in the selection. Nevertheless, a small misidentification probability of $\varepsilon^{\mathrm{miss}}_{\mathrm{p}\pi} = (2.2 \pm 0.5) \cdot 10^{-4}$ has been determined by studying protons in the general Monte Carlo sample. The protons considered for the study were required to have a momentum of $p_{\mathrm{p}} > 3$ GeV/c, a transverse momentum of $p^t_{\mathrm{p}} > 0.8$ GeV/c and a point of closest approach to the primary vertex of $d^{\mathrm{p}}_0 < 0.5$ cm.

In the standard JETSET Monte Carlo program the branching ratio of $\overline{\mathrm{B}}^0/\mathrm{B}^- \rightarrow \Lambda \overline{\mathrm{p}} \mathrm{X}$ is less than 0.1%. However, recent measurements give a branching ratio of $(2.5 \pm 0.4)\%$ [2]. In order to study the contribution of the background to the muon signal, 5265 background events have been generated using JETSET with modified EURODEC decay tables to simulate the B decays. Again, all Λ have been forced to decay into protons and pions in this sample. The resulting events have been processed with the full detector simulation and have been passed through the event selection. Since the misidentification probability, $\epsilon^{\mathrm{miss}}_{\mathrm{p}\mu}$, is already known, the sample is used to determine the efficiency dependence on the kinematic and geometrical properties

<table>
<tr><th colspan="3">Exclusive Backgrounds in %</th></tr>
<tr><th>Background</th><th>Right-Sign</th><th>Wrong-Sign</th></tr>
<tr><td>$\Lambda_c \rightarrow \Lambda\ell^+\nu$</td><td>–</td><td>2.53±0.25</td></tr>
<tr><td>$\Lambda_b \rightarrow \Lambda_c\tau^-\overline{\nu}$</td><td>1.84±0.21</td><td>–</td></tr>
<tr><td>$\Lambda_b \rightarrow \Lambda_c D_s^-,\ D_s^- \rightarrow \ell^- X$</td><td>1.19±0.62</td><td>–</td></tr>
<tr><td>$\overline{B}^0 \rightarrow \Lambda_c\overline{n}\ell^-\overline{\nu}_\ell$</td><td>1.40±1.40</td><td>–</td></tr>
<tr><td>$\overline{B}^0 \rightarrow \Lambda_c\,\overline{p}\,\pi^0,\ \Lambda_c \rightarrow \Lambda X$</td><td>Neglected</td><td>Neglected</td></tr>
<tr><td rowspan="2">Total</td><td>4.43±1.55</td><td>2.53±0.25</td></tr>
<tr><td colspan="2">+1.9 ± 1.6</td></tr>
</table>

Table 6.3: Backgrounds from Exclusive Decay Channels

Contributions to the right-sign and the wrong-sign samples of certain exclusive decay channels as obtained from Monte Carlo simulations are summarised. All values are given relative to the number of identified b *baryons in the corresponding samples.*

---

of the decay. All protons in the sample are assumed to fake a muon in order to obtain a statistically significant sample. With this ansatz a selection efficiency of

$$\epsilon_{\Lambda\overline{p}} = (0.0199 \pm 0.0012) \cdot \epsilon_{p\mu}^{\mathrm{miss}} \tag{6.4}$$

is obtained. The contribution to the muon signal is on the order of 0.2 event. This potential background source is therefore negligible.

The contributions to the right-sign and the wrong-sign samples of the studied exclusive decay channels are summarised in table 6.3. An imbalance of

$$\frac{n_r - n_w}{n_{\Lambda_b}} = (+1.9 \pm 1.6)\% \tag{6.5}$$

is obtained from the listed exclusive decay channels.

6.3 Other Backgrounds

Random combinations of tracks, and leptons or Λ particles that have been misidentified are another source of background. The total contribution from this source is of similar magnitude as the contributions from the fragmentation

Λ particles but, in contrast, this background is assumed to contribute to the right-sign and wrong-sign samples evenly. The hypothesis has been tested with the general Monte Carlo sample and is found to be correct to within the statistical uncertainty. In the case of Λ particles that have been misidentified, the hypothesis is cross-checked by analysing the sidebands of the $p\pi$ invariant mass distribution (see fig. 4.4). Random combinations of tracks or $K^0 \rightarrow \pi^+\pi^-$ decays that fake a Λ are distributed over a wide range of invariant masses. An imbalance between the size of the right-sign and the wrong-sign samples caused by these backgrounds would be observable also in the sidebands of the $p\pi$ invariant mass distribution of the Λ candidates. In the sideband regions, namely $m_p + m_\pi < m_{p\pi} < 1.10$ MeV/c^2 and 1.14 MeV/$c^2 < m_{p\pi} < 1.25$ MeV/c^2, 696/678 events are found in the right/wrong-sign samples respectively. The two numbers agree within the statistical uncertainty with a probability of 63% ($\chi^2/DoF = 0.24$). Therefore, it can be concluded that no evidence for an imbalance is found.

Potential complications arise if the lepton from a semileptonic $\Lambda_b \rightarrow \Lambda \ell X$ decay and one of the tracks resulting from the $\Lambda \rightarrow p\pi$ decay have been identified but the second candidate track of the Λ is misidentified. The misidentified track is most likely the pion candidate track, due to the looser pion selection criteria and the high production rates of pions. Since the classification of the candidate as Λ or $\overline{\Lambda}$ depends upon the charge of the proton candidate[3], such events would only contribute to the right-sign sample. In the determination of the efficiency, these events are not considered as being correctly identified. The magnitude of the effect is studied by looking for "double events"[4] in the data sample with identical lepton and either identical proton but different pion tracks, or vice versa. Two double events with the same lepton and the same pion tracks but different proton tracks have been found, one in the right-sign

---

[3] In principle, cases are possible where the wrongly selected pion has a momentum greater than that of the proton. In this case, the pion would be identified as proton and the proton as pion candidate, leading to an $\overline{\Lambda}$ instead of a Λ or vice versa. Such events are suppressed by the dE/dx requirement on the proton candidate, the allowed invariant mass range of the system, and by the decreasing production probability of pions with increasing momentum.

[4] See definition of double events on page 88.

sample and one in the wrong-sign sample. They are expected to originate from background sources. Furthermore, five double events with the same lepton and same proton but different pion tracks are found, four in the right-sign sample and one in the wrong-sign sample. The excess of three double events in the right-sign sample is assumed to originate from semileptonic b-baryon decays with one partly misidentified Λ. Studies of the polarised and the unpolarised Monte Carlo samples lead to an expectation of (0.8 ± 0.2) such events. The likelihood of expecting 0.8 events and finding three or more is 5%. Furthermore, Monte Carlo studies indicate that in 63% of the cases where a $\Lambda\ell$-correlation with a fake pion track has been selected, a candidate including the correct pion track is selected too, causing a double event. From the occurrence of the double events a contribution to the right-sign sample of 5 ± 2 events is estimated. In the normalisation used throughout this chapter, this corresponds to a contribution to the right-sign sample of $(1.1 \pm 0.5)\%$.

Contributions from hadronic decays of b baryons where leptons are produced via decays of secondary particles into lepton pairs are small. Such secondary processes are, for example, photon conversions or $J/\psi \to \ell^+\ell^-$ decays. These backgrounds contribute to the right-sign and the wrong-sign samples evenly and are handled correctly by the right-wrong sign subtraction method. The contribution to each sample is predicted to be small, $(1.07 \pm 0.11)\%$.

6.4 Summary

Several background processes have been investigated and are found to contribute differently to the right-sign and wrong-sign samples. The largest imbalance is caused by leptons from actual b-baryon decays combined with fragmentation Λ particles. The model uncertainty of determining a correction factor for the backgrounds caused by leptons from heavy quark decays which were combined with fragmentation Λ particles has been studied by varying the popcorn parameter in the event generator. Background contributions from exclusive decay channels have relatively small influence. Several other background sources, mainly due to the misidentification of tracks, have been

Right-Wrong-Sign Correction in %		
Background Source	Correction	Systematic Error
Frag. Λ plus ℓ from b/c-Quark Decay	-11.8	± 2.8
Exclusive Decay Channels	$+1.9$	± 1.6
Combinatorials and Fakes	$+1.1$	± 0.5
Total Change	-8.8	± 3.3

Table 6.4: Summary for Different Classes of Backgrounds
Listed are the corrections to the wrong-sign subtraction method obtained for different classes of backgrounds. The values given are normalised to the number of selected b *baryons.*

---

investigated and are also found to cause only a small imbalance between the right-sign and the wrong-sign samples. All background sources, except that due to $\overline{B}^0 \rightarrow \Lambda_c \overline{p} \pi^0$ decays which was found to be negligible, contribute to the electron and muon channels evenly. A summary of all classes of backgrounds is given in table 6.4. A total correction to the wrong-sign subtraction method of

$$\delta = \frac{n_r - n_w}{n_{\Lambda_b}} = (-8.8 \pm 3.3)\% \tag{6.6}$$

is computed and will be applied in the determination of the product branching ratio in the next chapter.

Chapter 7

Results

This analysis is based upon data which have been recorded by the OPAL experiment during the period from 1990 to 1994. After applying the multihadronic event selection,

$$N_{\mathrm{had}} = 3,610,323$$

multihadronic events remain. The flavour bias of the selection and the background in the sample are negligible for this analysis. In this sample the following number of Λ-ℓ charge correlations are selected,

	Λ-e	Λ-μ
N_r	268	466
N_w	128	199

where N_r and N_w are the numbers of Λ-ℓ charge correlations in the right and wrong-sign samples respectively. The number of b baryons, n_{Λ_b}, can be computed from the excess in the right-sign sample

$$n_{\Lambda_b} = \frac{N_r - N_w}{1 + \delta}, \tag{7.1}$$

where $\delta = (-8.8 \pm 3.3)\%$ represents a correction factor to the simple subtraction method as discussed in chapter 6. The resulting numbers of b baryon candidates are

$$\begin{aligned} n^e_{\Lambda_b} &= 154 \pm 22 \pm 5, \\ n^\mu_{\Lambda_b} &= 293 \pm 23 \pm 10, \end{aligned} \tag{7.2}$$

where the first error is statistical and the second error reflects the uncertainties due to the correction to the background subtraction method.

The product branching ratios are obtained by rewriting equation (2.40) and including the selection efficiency, $\varepsilon_{\Lambda\ell}$,

$$f(\mathrm{b} \to \Lambda_\mathrm{b}) \cdot BR(\Lambda_\mathrm{b} \to \Lambda\ell^-\bar{\nu}\mathrm{X}) = \frac{n_{\Lambda_\mathrm{b}}}{2\ \varepsilon_{\Lambda\ell}\ N_\mathrm{had}\ \Gamma_{\mathrm{b}\bar{\mathrm{b}}}/\Gamma_\mathrm{had}}. \tag{7.3}$$

The selection efficiencies (see eq. (5.9))

$$\begin{aligned} \varepsilon_{\Lambda e} &= 0.0378 \pm 0.0014 \pm 0.0028, \\ \varepsilon_{\Lambda\mu} &= 0.0602 \pm 0.0017 \pm 0.0044 \end{aligned}$$

have been determined in chapter 5. The first errors represent the errors caused by limited Monte Carlo statistics and the uncertainties in the lepton-finding algorithms, and are uncorrelated with one another. The second errors of the two samples account for the uncertainties of the Λ identification and the systematic uncertainties of the decay modelling, and are fully correlated with one another. The relative production rate of $\mathrm{b}\bar{\mathrm{b}}$ pairs in $\mathrm{Z}^0 \to$ hadron decays (see eq. (2.15)),

$$\frac{\Gamma_{\mathrm{b}\bar{\mathrm{b}}}}{\Gamma_\mathrm{had}} = 0.2171 \pm 0.0030$$

is assumed [14]. Using the above numbers, a product branching ratio of

$$\boxed{f(\mathrm{b} \to \Lambda_\mathrm{b}) \cdot BR(\Lambda_\mathrm{b} \to \Lambda e^-\bar{\nu}\mathrm{X}) = (2.59 \pm 0.37 \pm 0.23) \cdot 10^{-3}} \tag{7.4}$$

is computed for the electron sample and

$$\boxed{f(\mathrm{b} \to \Lambda_\mathrm{b}) \cdot BR(\Lambda_\mathrm{b} \to \Lambda\mu^-\bar{\nu}\mathrm{X}) = (3.10 \pm 0.30 \pm 0.27) \cdot 10^{-3}} \tag{7.5}$$

for the muon sample.

The product branching ratios obtained from the electron and muon samples are expected to be consistent with one another assuming lepton universality.

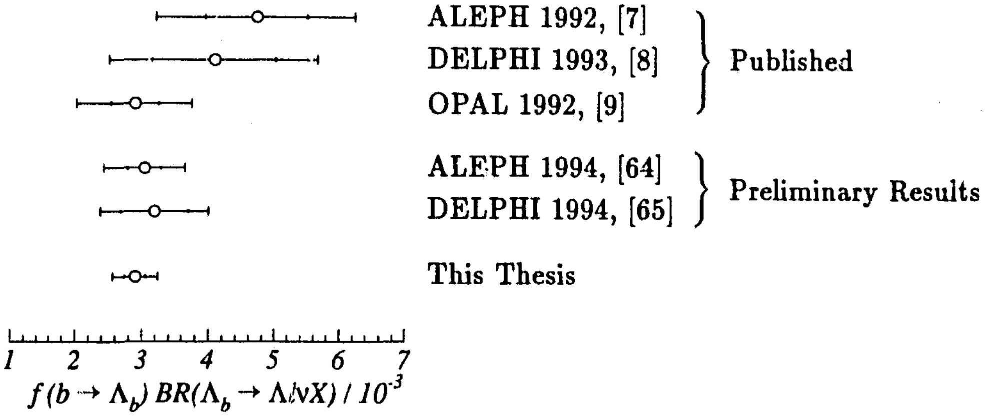

Figure 7.1: Comparison of the Result with Other Measurements
The inner error bar marks the fraction of the error due to statistics.

Most of the systematic errors, with the exception of the first error on the efficiency as given above, are identical for the two measurements. Taking the uncorrelated error of the efficiency determination and the statistical errors of the Λ-e and Λ-μ analyses into account, a χ^2 of the two measurements of 1.1 is calculated. This corresponds to a probability of 30% that the measurements are consistent. The result,

$$\boxed{r \equiv f(\mathrm{b} \rightarrow \Lambda_\mathrm{b}) \cdot BR(\Lambda_\mathrm{b} \rightarrow \Lambda \ell^- \bar{\nu} \mathrm{X}) = (2.91 \pm 0.23 \pm 0.25) \cdot 10^{-3}} \tag{7.6}$$

is obtained by averaging the two channels weighted by the statistical and the uncorrelated part of their systematic errors. The symbol ℓ in (7.6) represents either an electron or a muon.

The combined result supersedes the previous value published by the OPAL collaboration of $r^{\mathrm{pub}} = (2.9 \pm 0.5 \pm 0.7) \cdot 10^{-3}$ [9], which was derived from data recorded in the years 1990 and 1991. The result is shown in comparison to other measurements in figure 7.1.

7.1 Additional Checks

An analysis of the data taken in 1990 and 1991 using the techniques of this thesis leads to a result of $r(1990-91) = (3.4 \pm 0.6 \pm 0.3) \cdot 10^{-3}$. The difference between this and the previously published result is caused by changes in the event selection and in the estimate of the systematic errors and shifts. The largest differences are due to the correction used for the background estimate (9%) and the use of a different form factor to model the energy transfer from the Λ_b to the Λ_c in the Monte Carlo simulation which was used in determining the overall efficiency (5%).

As an alternative to the standard OPAL electron selection algorithm which covers an angular range of $|\cos\theta| < 0.715$, an artificial neural net algorithm [66] has been used. The network is of the feed-forward type and was trained on simulated events to identify electrons. The measured quantities fed into the network are similar to those used by the standard electron identification. In contrast to the standard electron identification, the neural network covers an angular range of $|\cos\theta| < 0.98$. The neural network output, which ranges between 0.0 and 1.0, was required to be greater than 0.96 in order to approximately match the efficiency and purity of the muon sample. A total of 408 right-sign and 185 wrong-sign Λ-electron correlations are found in the data sample. The efficiency of the electron identification using the neural network has been found to be overestimated in Monte Carlo simulation in comparison to the data recorded in the years 1990–1993 by $(\varepsilon_e^{\mathrm{Data}} - \varepsilon_e^{\mathrm{MC}})/\varepsilon_e^{\mathrm{MC}} = -4.7\% \pm 2.8\%$ [66]. Assuming the data collected in 1994 are of the same quality as those of 1993 and, therefore, applying the same corrections, a product branching ratio of

$$f(\mathrm{b} \to \Lambda_\mathrm{b}) \cdot BR(\Lambda_\mathrm{b} \to \Lambda \mathrm{e}^- \bar{\nu} \mathrm{X}) = (2.76 \pm 0.30 \pm 0.24) \cdot 10^{-3} \qquad (7.7)$$

is calculated. Both electron selection methods are based on similar quantities and hence their systematic uncertainties are highly correlated. Under the assumption that the systematic errors are identical and by taking the statistical correlations between both samples into account, a $\chi^2 = 0.7$ is found when the results of the measurements are compared. This corresponds to a probability of 41%, indicating reasonable agreement of the two selection methods.

If the neural network result is averaged with the result obtained with the muon channel

$$f(\mathrm{b} \rightarrow \Lambda_{\mathrm{b}}) \cdot BR(\Lambda_{\mathrm{b}} \rightarrow \Lambda \ell^{-} \overline{\nu} \mathrm{X}) = (2.95 \pm 0.21 \pm 0.25) \cdot 10^{-3} \qquad (7.8)$$

is computed, indicating no significant gain by using the neural network method in obtaining the final result. Since the determination of the neural network identification efficiency must be considered preliminary, the result obtained with the established standard electron identification has been used to obtain the final result given in equation (7.6).

7.2 Discussion

7.2.1 Determination of $f(\mathrm{b} \rightarrow \Lambda_{\mathrm{b}})$

As described in section 2.3, the branching ratio can be split into (eq. (2.32))

$$BR(\Lambda_{\mathrm{b}} \rightarrow \Lambda \ell \mathrm{X}) = BR(\Lambda_{\mathrm{b}} \rightarrow \Lambda_{\mathrm{c}} \ell \overline{\nu} \mathrm{X}) \cdot BR(\Lambda_{\mathrm{c}} \rightarrow \Lambda \mathrm{X}').$$

The second branching ratio, $BR(\Lambda_c^+ \rightarrow \Lambda \mathrm{X})$, has been measured by ARGUS and CLEO to be $(35 \pm 11)\%$ [2][1]. The contribution of semileptonic b-baryon decays into c baryons other than the Λ_c^+, which may have different branching ratios into Λ, can be neglected in comparison to the 31% error on the branching ratio $BR(\Lambda_c^+ \rightarrow \Lambda \mathrm{X})$. Using the above value, the branching ratio

$$\boxed{f(\mathrm{b} \rightarrow \Lambda_{\mathrm{b}}) \cdot BR(\Lambda_{\mathrm{b}} \rightarrow \Lambda_{\mathrm{c}} \ell^{-} \overline{\nu} \mathrm{X}) = (8.3 \pm 2.8) \cdot 10^{-3}} \qquad (7.9)$$

is computed.

The branching fraction (7.9) can be further reduced if a value for the branching ratio $BR(\Lambda_b^0 \rightarrow \Lambda_c^+ \ell^- \overline{\nu})$ is assumed. The three estimates mentioned

---

[1] The quoted ARGUS and CLEO measurements have not yet been entered into the JETSET 7.3 decay tables. The value used therein is $BR^{\mathrm{MC}}(\Lambda_c^+ \rightarrow \Lambda \mathrm{X}) = 46.5\%$. The higher value leads to an over production of Λ-ℓ correlations in the Monte Carlo simulations,

$$\frac{f^{\mathrm{MC}} \cdot BR^{\mathrm{MC}}(\Lambda_{\mathrm{b}} \rightarrow \Lambda \ell^{-} \overline{\nu} \mathrm{X})}{f^{\mathrm{data}} \cdot BR^{\mathrm{data}}(\Lambda_{\mathrm{b}} \rightarrow \Lambda \ell^{-} \overline{\nu} \mathrm{X})} = 1.55 \pm 0.18.$$

in chapter 2.3 are tried in the following calculations. First of all, the branching ratio $BR(\Lambda_b^0 \rightarrow \Lambda_c^+ \ell^- \overline{\nu}) = (2.45 \pm 0.75)\%$ (see eq. (2.38)) is used. This value has been computed from the HQET calculation by Guo and Kroll [6]. The resulting branching fraction is

$$f^{\mathrm{Guo}}(\mathrm{b} \rightarrow \Lambda_\mathrm{b}) = (34 \pm 15)\%, \tag{7.10}$$

which appears surprisingly large compared to the value of 8.5% obtained from the JETSET 7.3 simulation and considering that the JETSET 7.3 simulations overestimates baryon production (see section 2.2.2). The close to 45% error results from the 31% uncertainty of the $BR(\Lambda_c \rightarrow \Lambda X)$ and from the 31% uncertainty in the theoretical prediction of the $BR(\Lambda_b^0 \rightarrow \Lambda_c^+ \ell^- \overline{\nu})$ which originates largely from the 12% uncertainty of the CKM matrix element, V_{cb}, which enters quadratically into the calculation (2.34).

Alternatively, the branching ratio, $BR(\Lambda_b^0 \rightarrow \Lambda_c^+ \ell^- \overline{\nu}) = (5.7 \pm 1.9)\%$, is used. This value has been calculated using the formulae given by Körner and Krämer. This higher branching ratio was obtained by assuming form factors from a vector meson dominance model [5]. The resulting branching fraction is

$$f^{\mathrm{Körner}}(\mathrm{b} \rightarrow \Lambda_\mathrm{b}) = (15 \pm 7)\%. \tag{7.11}$$

An even higher branching ratio of $BR(\Lambda_b^0 \rightarrow \Lambda_c^+ \ell^- \overline{\nu}) = (11.5 \pm 1.5)\%$ had been suggested by Mannel and Schuler assuming similar semileptonic decay rates for b baryons as for b mesons [32]. The branching ratio is similar in magnitude to that used in the JETSET 7.3 decay tables, 11.4%. The branching ratio suggested by Mannel and Schuler together with equation (7.9) leads to a branching fraction of

$$f^{\mathrm{Mannel}}(\mathrm{b} \rightarrow \Lambda_\mathrm{b}) = (7.2 \pm 2.6)\%. \tag{7.12}$$

This value compares well with the value obtained from the JETSET 7.3 simulations, $f^{\mathrm{MC}}(\mathrm{b} \rightarrow \Lambda_\mathrm{b}) = 8.5\%$ (see section 2.2.2).

In conclusion, the values of $f(\mathrm{b} \rightarrow \Lambda_\mathrm{b})$ obtained depend strongly on the theoretical model chosen to estimate the $BR(\Lambda_b^0 \rightarrow \Lambda_c^+ \ell^- \overline{\nu})$.

Model	$BR(\Lambda_b \rightarrow \Lambda_c \ell \bar{\nu} X)$	$BR(\Lambda_b \rightarrow \Lambda_c X)$
	in %	in %
JETSET 7.3 default	11.4	90
Guo & Kroll	2.45 ± 0.75	42 ± 14
Körner & Krämer	5.7 ± 1.9	92 ± 36
Mannel & Schuler	11.5 ± 1.5	182 ± 47

Table 7.1: Constraints on Different Models

As mentioned in the text, events containing semileptonically decaying b *baryons with a* Λ *in their decay chain are occuring to often in JETSET 7.3 simulations. The JETSET values are given in the table for comparison. The branching ratio* $BR(\Lambda_b \rightarrow \Lambda_c \ell \bar{\nu} X)$ *has been calculated elsewhere using different theoretical approaches as described in the text. Using (7.6) and in addition the preliminary measurement of* $BR(\text{b hadron} \rightarrow \Lambda X)$ *[67], the model prediction can be transformed into values for* $BR(\Lambda_b \rightarrow \Lambda_c X)$*. This branching ratio is expected to be in the range of 80–90%. The value in the last line is about 2 standard deviations outside the physical limits indicating clear disagreement between the model and the data.*

7.2.2 Inclusion of Other Measurements

The theoretical estimates for the branching ratio given in the previous section disagree with one another. Possible constraints could be made if the preliminary measurement [67]

$$b \equiv BR(\text{b hadron} \rightarrow \Lambda X) = (5.9 \pm 0.8)\%, \tag{7.13}$$

holds. The branching ratio $BR(\Lambda_b \rightarrow \Lambda X)$ is given by

$$BR(\Lambda_b \rightarrow \Lambda X) = \frac{b - (1-f)\; BR(B \rightarrow \Lambda X)}{f}, \tag{7.14}$$

where $f \equiv f(b \rightarrow \Lambda_b)$ and B denotes a b meson. The left-hand side of the equation can be split into

$$BR(\Lambda_b \rightarrow \Lambda X) = BR(\Lambda_b \rightarrow \Lambda_c X) \cdot BR(\Lambda_c \rightarrow \Lambda X'), \tag{7.15}$$

if it is assumed that all b baryons decay via c baryons into Λ particles. This is a reasonable assumption, given the limit on its most likely alternative decay

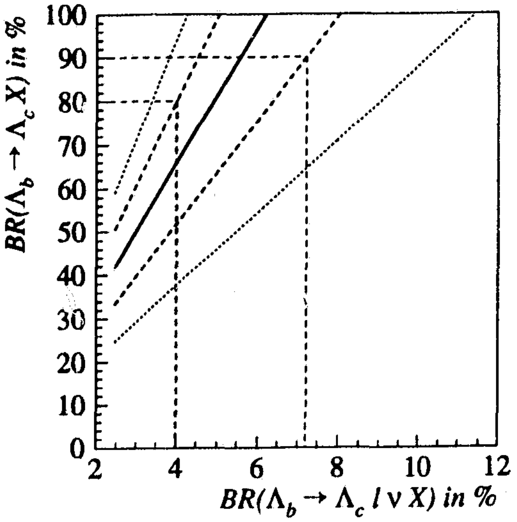

Figure 7.2: $BR(\Lambda_b \to \Lambda_c \ell \bar{\nu} X)$ *$BR(\Lambda_b \to \Lambda_c \ell^- \bar{\nu} X)$ can be constrained by $BR(\Lambda_b \to \Lambda_c X)$ (solid line) as described in the text. The dashed line marks the 1σ uncertainty of the constraint and the dotted line corresponds to a 2σ deviation. Assuming reasonable values for $BR(\Lambda_b \to \Lambda_c X)$ of 80–90%, the corresponding limits on $BR(\Lambda_b \to \Lambda_c \ell^- \bar{\nu} X)$ have been set.*

mode, $f(b \to \Lambda_b) \cdot BR(\Lambda_b \to J/\psi \Lambda) = 3.4 \cdot 10^{-4}$ [68]. The branching ratio $BR(B \to \Lambda X) = (4.0 \pm 0.5)\%$ has been measured by ARGUS and CLEO [2]. On the right-hand side one can substitute for f using equation (7.6). This leads to

$$\begin{aligned} BR(\Lambda_b \to \Lambda_c X) &= \frac{1}{r}\,(b - x) - BR(\Lambda_c \to \Lambda X) \\ &\quad - \frac{1}{r}\Big(BR(\Lambda_c \to \Lambda X) \cdot BR(B \to \Lambda X) \cdot x\Big) \end{aligned} \tag{7.16}$$

with r being the result of equation (7.6) and $x \equiv BR(\Lambda_b \to \Lambda_c \ell \bar{\nu} X)$. Using the three previously discussed theoretical estimates of x, the values given in table 7.1 are computed. For a simple spectator model, values for $BR(\Lambda_b \to \Lambda_c X)$ on the order of 80–90% would be expected. The remaining 10–20% accounts for possible decays into c mesons such as the decay $\Lambda_b \to D^0 n X$. Figure 7.2 depicts the values obtained by varying x between the predictions. Assuming $BR(\Lambda_b \to \Lambda_c X) = (85 \pm 5)\%$

$$\boxed{BR(\Lambda_b \to \Lambda_c \ell \bar{\nu} X) = (5.6 \pm 1.6)\%} \tag{7.17}$$

is obtained. This leads to an estimate of

$$\boxed{f(b \to \Lambda_b) = (14.8 \pm 4.2)\%}\,. \tag{7.18}$$

The $BR(\Lambda_b \rightarrow \Lambda_c \ell \bar{\nu} X)$ is in very good agreement, 93% probability, with the value computed from the formulae given by Körner and Krämer [5], but it is not sufficient to exclude the estimate based on the calculations of Guo and Kroll [6], with which it has a 9% probability of agreeing. Nevertheless, the simple assumption Mannel and Schuler used for their branching ratio estimate [32] can be clearly disregarded since the probability of agreement with the measurement is only 1%.

Bibliography

[1] C. Quigg, *Gauge Theories of the Strong, Weak, and Electromagnetic Interaction*, The Benjamin/Cummings Publishing Company, Inc., Menlo Park, CA, (1983);
and others.

[2] *Review of Particle Properties*, Physical Review **D 50** (1994).

[3] M. Gell-Mann, Physics Letters **8** (1964) 214;
G. Zweig, CERN Report **8182/TH. 401** (1964) (unpublished).

[4] M.B. Voloshin, M.A. Shifman, Soviet Journal of Nuclear Physics **45** (1987) 292;
N. Isgur, M. Wise, Physics Letters **B 232** (1989) 113;
E. Eichten, B. Hill, Physics Letters **B 234** (1990) 511;
H. Georgi, Physics Letters **B 240** (1990) 447.

[5] J. G. Körner and M. Krämer, Physics Letters **B 275** (1992) 495.

[6] X.H. Guo and P. Kroll, Zeitschrift für Physik **C 59** (1993) 567;
M. Neubert, Nuclear Physics **B 371** (1992) 149.

[7] ALEPH Collab., D. Decamp, *et al.*, Physics Letters **B 278** (1992) 209.

[8] DELPHI Collab., P. Abreu, *et al.*, Physics Letters **B 311** (1993) 379.

[9] OPAL Collab., P. D. Acton, *et al.*, Physics Letters **B 281** (1992) 394.

[10] A. Blondel, "Precision Electroweak Physics at LEP", CERN-PPE/94-133 (1994).

[11] S.L. Glashow, J. Iliopoulos, L. Maiani, Physical Review **D 2** (1970) 1285;
S. Weinberg, Physical Review Letters **19** (1967) 1264;
A. Salam, *Elementary Particle Theory*, Ed. N. Svartholm, (Almquist and Wiksells, Stockholm, 1969) 367.

[12] D. Griffiths, *Introduction to Elementary Particles*, John Wiley & Sons, Inc., New York, Chichester, Brisbane, Toronto, Singapore (1991), Appendix C.

[13] Edited by G. Altarelli, R. Kleiss, C. Verzegnassi, *Z Physics at LEP* vol. 1 CERN 89-08 (1989).

[14] OPAL Collab., R. Akers, *et al.*, Zeitschrift für Physik C **65** (1995) 17.

[15] D. H. Perkins, *Introduction to Hight Energy Physics*, third Edition, Addison-Wesley Publishing Company, Inc., London, Amsterdam, Don Mills, Sydney, Tokyo (1982) p. 291.

[16] B. Andersson, G. Gustafson, G. Ingelman, T. Sjöstrand, Physics Reports **97** (1983) 31.

[17] T. Sjöstrand, Computer Physics Communication **39** (1986) 347.

[18] X. Artru, Physics Reports **97** (1983) 147.

[19] T. Sjöstrand, M. Bengtsson, Computer Physics Communication **43** (1987) 367.

[20] T. Sjöstrand, M. Bengtsson, *The Lund Monte Carlo programs - JETSET version 7.2*, CERN Pool programs W5035 long writeup (1989).

[21] W. Zimmermann, Physikalische Blätter **47** (1983) 605.

[22] Edited by G. Altarelli, R. Kleiss, C. Verzegnassi, *Z Physics at LEP* vol. 3 CERN 89-08 (1989).

[23] O. Nachtmann, *Phänomene und Konzepte der Elementarteilchenphysik*, Friedrich Vieweg & Sohn; Braunschweig (1986).

[24] M. Creutz, L. Jacobs, C. Rebbi, Physics Reports **95** (1983) 201.

[25] B. Anderson, G. Gustaafson and T. Sjöstrand, Physica Scripta **32** (1985) 574.
A popcorn model has been implemented in JETSET, where the frequency for the process baryon-meson-antibaryon is regulated in JETSET by the parameter PARJ(5), such that the probability is given by PARJ(5)/(0.5 + PARJ(5)).

[26] OPAL Collab., P. Acton, *et al.*, Physics Letters **B 305** (1993) 415.

[27] OPAL Collab., R. Akers, *et al.*, Zeitschrift für Physik **C 63** (1994) 181.

[28] OPAL Collab., P. Acton, *et al.*, Physics Letters **B 291** (1992) 503.

[29] ARGUS Collab., H. Albrecht, *et al.*, Zeitschrift für Physik **C 52** (1991) 353;
CLEO Collab., D. Bortoletto, *et al.*, Physical Review **D 37** (1988) 1719.

[30] C. Peterson, D. Schlatter, I. Schmitt and P.M. Zerwas, Physical Review **D 27** (1983) 105.

[31] M. Neubert, Physics Letters **B 264** (1991) 455.

[32] T. Mannel and G. Schuler, Physics Letters **B 297** (1992) 194.

[33] OPAL Collab., R. Akers, *et al.*, Physics Letters **B 316** (1993) 435;
OPAL Physics Note, **PN146** (1994).

[34] ALEPH Collab., *Search for strange b baryon through* $\Xi^{\pm}$ *lepton correlations*, 27th International Conference on High Energy Physics, Glasgow, Scotland, 1994, ICHEP94 Ref. gls0590;
OPAL Physics Note, **PN162** (1995).

[35] OPAL Collab., P. Acton, *et al.*, et al. Zeitschrift für Physik **C 60** (1993) 217.

[36] OPAL Collab., R. Akers, *et al.*, CERN-PPE/95-12 (1995);
submitted to Zeitschrift für Physik.

[37] J. Allison, *et al.*, Nuclear Instrumentation Methods **A 317** (1992) 47.

[38] ALEPH Collab., D. Decamp, *et al.*, Nuclear Instrumentation and Methods **A 294** (1990) 121.

[39] DELPHI Collab., P. Aarnio, *et al.*, Nuclear Instrumentation and Methods **A 303** (1991) 233.

[40] L3 Collab., B. Adeva, *et al.*, Nuclear Instrumentation and Methods **A 289** (1990) 35.

[41] OPAL Collab., K. Ahmet, *et al.*, Nuclear Instrumentation and Methods **A 305** (1991) 275.

[42] A. Blondel, *Precision Tests of the Standard Electroweak Model*, High Energy Phenomenology, Proceedings of the Forty Second Scottish University Summer School in Physics, St. Andrews, (1993).

[43] P.P. Allport, *et al.*, Nuclear Instrumentation and Methods A **324** (1993) 34;
P.P. Allport, *et al.*, Nuclear Instrumentation and Methods A **346** (1994) 476.

[44] M. Hauschild, *et al.*, Nuclear Instrumentation and Methods A **314** (1992) 74;
O. Biebel, *et al.*, Nuclear Instrumentation and Methods A **323** (1992) 169.

[45] OPAL Collab., "Proposal for Upgrading the OPAL Luminosity Detector", CERN/LEPC/91-8 (1991);
OPAL Technical Note, TN178 (1993).

[46] OPAL Collab., G. Alexander, *et al.*, Zeitschrift für Physik C **52** (1991) 175.

[47] OPAL Collab., R. Akers, *et al.*, Zeitschrift für Physik C **60** (1993) 199;
J. Frederic Kral, OPAL Technical Note TN **147** (1993).

[48] OPAL Collab., P.D. Acton, *et al.*, Zeitschrift für Physik C **58** (1993) 523;
D. Charlton, OPAL Technical Note TN **239** (1994).

[49] OPAL Collab., M.Z. Akrawy, *et al.*, Zeitschrift für Physik C **49** (1991) 375.
As invariant mass-squared cut-off parameter $x_{\min} = 49\,(\mathrm{GeV}/c^2)^2$ was used.

[50] JADE Collab., W. Bartel, *et al.*, Zeitschrift für Physik C**33** (1986) 23;
JADE Collab., S. Bethke, *et al.*, Physics Letters B**213** (1988) 235.

[51] B. van Eijk, in Z Physics at LEP, eds Altarelli, Kleiss, Verzegnassi, CERN 89-08.

[52] *Review of Particle Properties*, Physical Review D **45** (1992).

[53] T. Sjöstrand, private communication;
S. Jadach and Z. Was, in *Z physics at LEP*, CERN 89-08, 1989, p. 235.

[54] J.R. Batley and S.L. Lloyd, OPAL Technical Note, TN113,
S.L. Lloyd and M.P. Singh, OPAL Technical Note, TN117.

[55] M. Morii, private communication.

[56] D. Charlton, private communication.

[57] ALEPH Collab., *Measurement of the Λ_b polarization at LEP*, 27th International Conference on High Energy Physics, Glasgow, Scotland, 1994, ICHEP94.

[58] OPAL Technical Note **TN125** (1992);
OPAL Collab., R. Akers, *et al.*, Physics Letters **B 337** (1994) 393,
and references therein.

[59] W. Kwong and J. Rosner, Physical Review **D 44** (1991) 212,
and references therein.

[60] T.Sjöstrand, Computer Physics Communication **39** (1986) 347.

[61] OPAL Collab., M.Z. Akrawy, *et al.*, Physics Letters **B 261** (1991) 334,
and references therein.

[62] CLEO Collab., D. Cinabro, *et al.*, *A study of baryon-production in B-decay: Search for semileptonic decays of B mesons to charmed baryons and the first observation of Ξ_c production in B-decay*, 27th International Conference on High Energy Physics, Glasgow, Scotland, 1994.

[63] ARGUS Collab., H. Albrecht, *et al.*, Physics Letters **B 249** (1990) 359.

[64] ALEPH Collab., *A measurement of the* b *Baryon Lifetime*, 27th International Conference on High Energy Physics, Glasgow, Scotland, 1994, ICHEP94 Ref. gls0603.

[65] DELPHI Collab., *Lifetime and Production Rate of Beauty Baryons from Z^0 Decays*, 27th International Conference on High Energy Physics, Glasgow, Scotland, 1994, ICHEP94 Ref. gls0162.

[66] OPAL Collab., R. Akers, *et al.*, Phys. Letters **B327** (1994) 411;
Hervé Lafoux, *Status of Neural Electron Identification*, OPAL Technical Note, **TN208** (1994);
Hervé Lafoux, *Studies of Systematic Effects for the Neural Electron ID*, OPAL Technical Note, **TN273** (1995).

[67] M. Pearce, OPAL Technical Note, **TN 268** (1994).

[68] OPAL Physics Note, **PN164** (1995).

Index

VITA

Surname:	Steuerer	Given Names:	Johannes Martin
Place of Birth:	Freiburg i. Br., Germany		
Date of Birth:	6. Sep. 1963		

Educational Institutions Attended:

University of Victoria	1991 – 1995
Albert-Ludwigs-Universität Freiburg	1988 – 1990
Trent University	1987 – 1988
Albert-Ludwigs-Universität Freiburg	1984 – 1987

Degrees Awarded:

Physik Diplom	Albert-Ludwigs-Universität Freiburg	1990
B.Sc. (Honours)	Trent University	1988

Honours and Awards:

University of Victoria Fellowship	1991 – 1993
Graduate Teaching Fellowship	1991, 1993, 1994, 1995

Partial Copyright Licence

Title of Dissertation:

Measurement of the Product Branching Ratio
$f(\mathrm{b} \rightarrow \Lambda_{\mathrm{b}}) \cdot BR(\Lambda_{\mathrm{b}} \rightarrow \Lambda \ell^{-} \bar{\nu} \mathrm{X})$

Author: ____________________
Johannes M. Steuerer
September 11, 1995